


2014

Fractal-based cloud shadow and irradiance model for power system analysis with high penetration of photovoltaics

Chengrui Cai
Iowa State University

Follow this and additional works at: <https://lib.dr.iastate.edu/etd>

 Part of the [Engineering Commons](#), and the [Oil, Gas, and Energy Commons](#)

Recommended Citation

Cai, Chengrui, "Fractal-based cloud shadow and irradiance model for power system analysis with high penetration of photovoltaics" (2014). *Graduate Theses and Dissertations*. 13739.
<https://lib.dr.iastate.edu/etd/13739>

This Dissertation is brought to you for free and open access by the Iowa State University Capstones, Theses and Dissertations at Iowa State University Digital Repository. It has been accepted for inclusion in Graduate Theses and Dissertations by an authorized administrator of Iowa State University Digital Repository. For more information, please contact digirep@iastate.edu.

**Fractal-based cloud shadow and irradiance model for power system analysis with
high penetration of photovoltaics**

by

Chengrui Cai

A dissertation submitted to the graduate faculty
in partial fulfillment of the requirements for the degree of
DOCTOR OF PHILOSOPHY

Major: Electrical Engineering

Program of Study Committee:
Dionysios Aliprantis, Co-Major Professor
Venkataramana Ajarapu, Co-Major Professor
James D. McCalley
Leigh Tesfatsion
Xiaoqing Wu

Iowa State University

Ames, Iowa

2014

Copyright © Chengrui Cai, 2014. All rights reserved.

TABLE OF CONTENTS

LIST OF TABLES	iv
LIST OF FIGURES	vi
ACKNOWLEDGEMENTS	xi
ABSTRACT	xii
CHAPTER 1 INTRODUCTION	1
1.1 Overview	1
1.2 Literature Review	2
1.3 Contribution	3
CHAPTER 2 MODEL DEVELOPMENT	5
2.1 Cloud Shadow Generation Using Fractals	5
2.2 Proposed Model	6
2.2.1 Solar Irradiance Characteristics	10
2.2.2 Meteorological and Geographic Parameters	11
2.2.3 Cloud Shadow Pattern Generation	14
2.2.4 Synthesis of the Irradiance Time Series	19
2.3 Sensitivity Analysis	20
2.4 Computational Requirements	22
2.5 Model Tuning	22
2.6 Model Summary	27
CHAPTER 3 MODEL APPLICATION TO A CASE STUDY OF LTC OPERATION	30

3.1	Introduction	30
3.2	Background on LTC and Problem Definition	31
3.3	Simulation Setup	33
3.3.1	Distribution System	33
3.3.2	PV System	35
3.3.3	Simulation Parameters	39
3.3.4	Scenario Parameters	40
3.3.5	Summary on Simulation Setup	45
3.4	Impact on LTC Operation in Different Season	46
3.5	Effect of Cloud Velocity and Cover	58
3.5.1	Impact of Cloud Velocity	59
3.5.2	Different Cloud Cover	62
3.6	Different PV Penetration	65
3.7	Comparison of Different Cloud and Irradiance Models	68
CHAPTER 4 CONCLUSION AND FUTURE WORK		79
4.1	Conclusions	79
4.2	Future Research Directions	81
APPENDIX A Technical Data for 65 PV Modules		84
APPENDIX B PV Experimental Station		88

LIST OF TABLES

2.1	Computing times	22
2.2	Statistical measures of experimental data	24
3.1	Simulation setup for studying LTC operation in summer and winter scenarios	49
3.2	Simulation result of total number of LTC operation for the 24-hour period in summer and winter scenarios.	59
3.3	Simulation setup for studying LTC operation under different cloud velocity	61
3.4	Simulation result of total number of LTC operations in 1-hr period of the summer day with different cloud velocity scenarios	62
3.5	Simulation setup for studying LTC operation under different cloud cover	65
3.6	Simulation result of total number of LTC operations in 1-hr period of the summer day with different cloud cover scenarios	68
3.7	Simulation setup for studying LTC operation under different PV penetration	68
3.8	Simulation result for the summer day with PV penetration scenarios (cloud cover is 50% and cloud velocity is 6 m/s).	70
3.9	Simulation result of total number of LTC operations in the study of comparing two different cloud shadow models	72
A.1	Module data part 1	85
A.2	Module data part 2	86

A.3	Module data part 3	87
B.1	Equipment list of PV experimental station (electrical parts)	89
B.2	Equipment list of PV experimental station (data acquisition parts) . .	90

LIST OF FIGURES

2.1	Illustration of the midpoint displacement algorithm.	7
2.2	(a) 513-by-513 fractal surface. Solid lines represent cutting planes of different height. (b) Cloud shadow pattern obtained with $h = 0$	8
2.3	Relationship between the cutting surface height (h) and the cloud cover (R).	10
2.4	(a) Measured global horizontal irradiance (solid) and the estimated diffuse horizontal irradiance (dotted). (b) Zenith angle. (c) Beam normal irradiance (solid) and digitization threshold (dotted). (d) Digitized shading condition.	12
2.5	Statistics of the beam normal irradiance for shaded periods shorter than 200 s, from experimental measurements.	13
2.6	Variation of: (a) cloud cover and (b) cloud velocity.	14
2.7	Geographic layout of measurement points.	15
2.8	(Top) Generated binary cloud shadow pattern for time period between 2:00 and 3:00 PM. The wind direction is SW. A is the study area. (Bottom) Final cloud shadow pattern, using a multi-layer rendering technique. The pixels of the hatched area on the right were not needed in this simulation.	16
2.9	Windows and strips for the calculation of the cutting surface.	17
2.10	Comparison of the cutting surface height before and after interpolation.	18
2.11	Magnified cloud shadow pattern.	19

2.12	(a) Cloud transparency level. (b) Beam horizontal irradiance under clear sky condition. (c) Synthesized global horizontal irradiance time series. (d) Spatially averaged irradiance time series for the cloud shadow of Fig. 2.8. (e)–(g) Spatially averaged irradiance time series for three other fractals. (h) Sample mean of spatially averaged irradiance time series for 100 Monte Carlo simulations.	21
2.13	Magnified global horizontal irradiance time series.	22
2.14	Statistics of the simulated beam normal irradiance. (a) base case; (b) $R(t_k) + 10\%$; (c) $R(t_k) - 10\%$; (d) $v_c(t_k) + 5$ m/s; (e) $v_c(t_k) - 5$ m/s.	23
2.15	Variation of statistical measures of T_{shaded} with λ . Solid line: high wind speed; dashed line: low wind speed.	25
2.16	Comparison of the cumulative distribution function of T_{shaded} from simulations (dashed line) and measurements (solid line). (Note that the shading duration can exceed 200 s in some cases, so the CDF reaches a value slightly lower than 1 in this plot.)	26
2.17	Variation of statistical measures of $G_{\text{shaded},n}$ with α . Solid line: high wind speed; dashed line: low wind speed.	27
2.18	Comparison of the cumulative distribution function of $G_{\text{shaded},n}$ from simulations (dashed line) and measurements (solid line).	28
3.1	Simplified distribution system schematic.	31
3.2	Two LTC configuration diagram, Y connection (left) and Delta connection (right).	32
3.3	Location of distribution transformers (red triangle) and houses (black dots) in the distribution feeder.	34
3.4	Measuring the location of each house in GoogleEarth	35
3.5	Roof pitch and slope angle.	36
3.6	Measuring the available roof area for PV system.	37
3.7	The module shipments in MW of top 10 PV supplier in 2012 worldwide.	38

3.8	Estimated probability density function of PV module efficiency.	38
3.9	Two measurement grids for generating the irradiance time series for each PV system. Left: using 1372 houses. Right: using 175 distribution transformers.	41
3.10	Comparing the substation total real power using different measurement grid. Dashed line: using 1372 houses. Solid line: using 175 distribution transformers.	41
3.11	Illustration of 1st and 2nd hosting capacity (HC), where the x -axis is the installed capacity of PV systems under a distribution transformer and the y -axis is the maximum loading experienced by the transformer.	43
3.12	Load and temperature for the first week of January and July in 2011.	47
3.13	The real and reactive power load at the substation for a summer (solid) and winter day (dashed).	48
3.14	The reshaped net load profile in the summer day.	50
3.15	The reshaped net load profile in the winter day.	51
3.16	Measurements at the substation for the summer day without any PV integration.	52
3.17	Measurements at the substation for the summer day with 100% PV penetration.	53
3.18	LTC operations within a zoomed 15-min period for the summer day with 100% PV penetration, 50% cloud cover and 5 m/s cloud velocity.	55
3.19	Measurements at the substation for the winter day without any PV integration.	56
3.20	Measurements at the substation for the winter day with 100% PV penetration.	57
3.21	Three-phase total number of LTC tap changes for cases with 100% PV penetration.	58

3.22	Measurements at the substation between 11 AM and 12 PM with summer load.	60
3.23	Total PV generation of one simulation case with different cloud velocity.	61
3.24	Measurements at the substation between 11 AM and 12 PM with summer load and low cloud velocity of 3 m/s.	63
3.25	Measurements at the substation between 11 AM and 12 PM with summer load and high cloud velocity of 15 m/s.	64
3.26	Total PV generation of one simulation case with different cloud cover.	66
3.27	The average value of three-phase total number of LTC tap changes in the 1-hr period simulation in a summer day with different cloud cover scenarios.	67
3.28	Total PV generation for 50% cloud cover and 6 m/s cloud velocity under 25%, 50%, 75% and 100% PV penetration scenarios.	69
3.29	The cumulative distribution function (CDF) of the cumulus cloud with area a within range of 0.1 to 2.34 square nautical miles.	71
3.30	Procedure to place cloud shadow objects in generating the shadow pattern.	73
3.31	The procedure of generating the cloud pattern band using Jewell's method. Black parts are cloud shadows. In this example, the cloud cover is set to be 30% and the cloud velocity is 10 m/s. The simulation time is 2 hours.	74
3.32	Generated cloud shadow pattern using the fractal and Jewell's model for different cloud cover. Cloud velocity is 6 m/s and the simulation duration is 1 hour. The length of the cloud pattern is 25 km and the width is 3.6 km.	75
3.33	PV generation for the study area under different cloud pattern synthesized by different model.	76

3.34	Compare the voltage profile of each phase under 25% cloud cover scenario using fractal based model (left) and Jewell's model (right). . . .	77
3.35	Compare the voltage profile of each phase under 50% cloud cover scenario using fractal based model (left) and Jewell's model (right). . . .	78
B.1	Schematic of PV generation system.	91
B.2	Schematic of data acquisition system.	92

ACKNOWLEDGEMENTS

I would like to take this opportunity to express my sincere gratitude to my major professor Dr. Dionysios C. Aliprantis for his patience, guidance and support throughout my PhD research work. His way of critical thinking in research inspires me to overcome many research challenges, and his words of encouragement often lights my hope to complete my PhD at Iowa State University.

I am also thankful to my committee members, Dr. Venkataramana Ajjarapu, Dr. James D. McCalley, Dr. Leigh Tesfatsion and Dr. Xiaoqing Wu for their great efforts and insightful suggestions to improve this work.

I dedicate this dissertation to my parents, Lin Cai and Ju Jiang, and my wife Dongqi for their unconditional love and support in every way possible throughout the process of this dissertation and beyond.

ABSTRACT

Distributed photovoltaic (PV) power generation systems are being rapidly deployed worldwide, causing technical problems such as reverse power flows, voltage rise and abnormal operation of voltage control devices in distribution feeders, and real and reactive power transients that affect the operation of the bulk transmission system. To fully understand and address these problems, extensive computer simulation studies are required. As a prerequisite, modeling of PV generation with satisfactory spatial and temporal resolution plays a key role. To this end, this dissertation sets forth a fractal-based cloud shadow and irradiance model that can be used to recreate the power generation of rooftop PV systems embedded in a distribution feeder, or that of a utility-scale PV power plant, during days with low-altitude cumulus clouds. Because of its clearly defined edge and the deep shadow it creates, the cumulus cloud is considered as the cloud type that contributes the most to fluctuations of power output from distributed PV systems, which is a primary concern of system engineers. Realistically shaped cumulus cloud shadows are modeled as fractals. Technical details of the model development, validation and tuning are presented. A case study that focuses on impacts to Load Tap Changer actions demonstrates the potential of the developed model in power system analysis with high penetration of photovoltaics.

CHAPTER 1 INTRODUCTION

1.1 Overview

Grid-tied photovoltaic (PV) power generation systems are being rapidly deployed. The cumulative worldwide installed PV generation capacity reached 136.7 GW at the end of year 2013 [1], with a considerable amount installed at the distribution level. However, distribution feeders are typically designed for delivering electric energy to end-use customers, rather than for collecting it from distributed energy resources. Hence, a variety of technical issues related to PV system integration arises, e.g., reverse power flows, voltage fluctuations and abnormal operation of voltage control devices in distribution feeders, and real and reactive power transients that affect the operation of the bulk transmission system.

To fully understand and address these problems, extensive computer simulation studies are required. This is feasible today using specialized distribution feeder analysis software, such as CYMDIST [2], ETAP [3], GridLAB-D [4], or OpenDSS [5]. These programs can represent distribution networks with high accuracy, which is critical for—among other things—shedding light on the impacts of distributed generation resources. Proper modeling of distributed PV generation is required, where one should account carefully for its variability at appropriate temporal and spatial resolution, under all possible environmental conditions. The majority of prior PV integration studies are based on single-point irradiance data obtained from various sources (e.g., [6]). However, during cloudy days, using the same solar irradiance time series for calculating the power output of hundreds or thousands of PV panels scattered over an area can lead to significant error [7–10]. Therefore, results could be overly conservative, and the costs to mitigate any foreseeable issues might be over-estimated. Since the primary driver of PV power output is the solar irradiance (in W/m^2), high-fidelity cloud shadow models, which

are capable of producing realistic irradiance time series to further model the PV generation, are becoming increasingly important and timely for electric power system engineers, especially under the premise that the exponential growth in PV capacity will continue to take place.

1.2 Literature Review

Ideally, one would use experimental data from areal measurements of solar irradiance, but this requires the installation of a costly sensor network, and such data are not commonly available. An alternative is to make use of cloud images [11], but there is limited availability at the necessary degree of temporal and spatial resolution. Practically the only remaining alternative is to devise numerical models that generate random cloud shadow patterns on the ground. This was the approach taken by Jewell et al., who generated cloud patterns using information on the size distribution of clouds [12–17]. Garrett and Jeter have employed a similar method to synthesize cloud patterns based on statistical information [18, 19]. These methods generate a rigid cloud pattern that moves over a given area with constant speed, and simple geometries are assumed for the cloud pattern, such as rectangular or circular shapes. These models cannot reproduce the irregular shape of cloud shadows, which could be important for studies of dynamic interactions between individual PV inverters and Volt/VAR control systems.

Two notable recent modeling approaches are those developed by Morf and Beaucage. Morf has proposed a series of models based on Markov chains to generate the solar irradiance for each point on a grid over an area [20–22]. These models reproduce statistical properties of cloud cover (i.e., percentage of sky area covered by clouds), but neglect the creation of realistic cloud shadow shapes, which could be important when modeling real distribution feeders with geographical coordinates of installed PV panels. Overall, Morf’s approach places less emphasis on meteorological parameters such as cloud type, cloud velocity or wind speed, and direction of cloud movement. Beaucage et al. have combined a mesoscale Numerical Weather Prediction (NWP) model with a stochastic cloud generation model to simulate the development of cloud patterns [23]. This model is powerful but comes at high computational cost. Moreover, the

initialization of atmospheric physics parameters of the NWP model is rather complicated and requires a certain level of meteorology expertise.

Here, a representation of the cloud perimeter using fractals, as originally proposed by Lovejoy [24,25], and further studied by Cahalan and Joseph [26] and others [27–29], is adopted. Fractal-based modeling can reproduce the naturally irregular shapes of the cumulus cloud shadow pattern, thereby yielding more realistic results than models based on simple geometrical shapes. In [30], Beyer et al. adopted the midpoint displacement algorithm [31] to generate a cloud shadow pattern, which was used to simulate the irradiance and validated by a statistical analysis.

1.3 Contribution

This dissertation sets forth a model of the solar irradiance over a given area during times when cumulus clouds are prevailing. The cloud shadow is modeled as a fractal. The model is probabilistic, and intended for use in Monte Carlo simulations. It yields a reasonable representation of temporal variability (on a second-by-second basis) and spatial variability (down to a resolution of a few meters) without requiring extraordinary computational resources, since it does not rely on a physics-based cloud model. This is key in conducting any type of study that requires detailed knowledge of the power flow variation in a distribution feeder over an extended time period of interest, e.g., over the course of several hours (the assumption of a series of quasi steady-state conditions is typical for the analysis of distribution feeders) [32–35].

The proposed model could be applied for the study of dynamic interactions of PV inverters with each other, or between the inverters and an integrated Volt/VAr control system coordinating the actions of tap changing transformers, voltage regulators, and switched capacitor banks [36–39]. Such analyses can facilitate the design of advanced control schemes for mitigating voltage rise [40, 41], minimizing distribution feeder losses [42], and reducing voltage fluctuations [43]. Moreover, they can be useful for estimating PV penetration limits [44, 45]. Finally, the proposed model could be applied, in lieu of real data, for calculating the aggregate power output of large-scale centralized or distributed PV systems, which is necessary for trans-

mission grid integration studies (investigating ramping issues, voltage stability, etc.) [46–48].

Compared to previous fractal-based cloud shadow models, this model has several novel features:

1. Realistic irradiance waveforms are generated, whereas in prior work, the synthesized irradiance typically varies between two fixed values for the clear and shaded time periods.
2. The synthesis of a cloud shadow pattern of arbitrary time duration is possible, thus allowing longer-term simulation studies.
3. The model is not restricted to constant meteorological conditions, but can represent variable cloud velocity, cloud cover and cloud movement direction.
4. The algorithm for generating the cloud shadow and irradiance time series is simple and can be easily implemented on a computer.
5. Parameters can be tuned based on commonly available meteorological data.
6. The output of the model can be easily integrated with popular distribution system simulation software.

CHAPTER 2 MODEL DEVELOPMENT

2.1 Cloud Shadow Generation Using Fractals

There exist ten principal types of clouds, viz., cirrus, cirrocumulus, cirrostratus, altocumulus, altostratus, nimbostratus, stratocumulus, stratus, cumulus, and cumulonimbus, which are categorized according to height as high, middle, and low clouds [49]. To the authors' knowledge, a universal algorithm that can generate all principal cloud types at high temporal and spatial resolution does not exist, due to the complexity of atmospheric physics. The proposed model represents the cloud type that contributes the most to fluctuations of power output from distributed PV systems, which is a primary concern of system engineers. This is generally considered to be the low-altitude cumulus cloud because of its clearly defined edge and the deep shadow it creates [7, 9, 10, 14, 19, 30, 50, 51].

The shapes of cumulus cloud shadow contours on the ground can be modeled as fractals, which can be synthesized using the midpoint displacement algorithm [30, 31]. The required parameters are the fractal dimension D , the number of pixels along the edge of a square ground area $(N + 1)$, and the actual pixel dimension s (in m; for example, $s = 7$ means that one pixel represents an area of 49 m^2 , with the pixel at its center). The ground area containing the cloud shadow is $((N + 1)s)^2$.

The fractal dimension D is a key property, for which different values have been proposed based on observations of cloud images [26, 28, 30]. It has been found that two different dimension values (D_1 and D_2) are adequate. For example, [30] proposes values of $D_1 \in [1.82, 1.94]$ and $D_2 \in [1.24, 1.43]$. To account for this in the midpoint displacement algorithm, D changes from D_1 to D_2 at a certain stage, as suggested by [30]. In our simulations, the values $D_1 = 1.9$ and $D_2 = 1.33$ are used. Of course, these parameters can be modified by the analyst, if different

types of low altitude cumulus clouds need to be generated.

A simple example showing the generation of a fractal surface with 25 pixels is illustrated in Fig. 2.1. The midpoint displacement algorithm is recursive, and takes $M = \log_2(N)$ stages to complete. In each stage, center midpoint values are calculated based on the four corner points of each square, and then values on the midpoints of the edges are calculated. The output of the algorithm is a three-dimensional fractal surface.

An example of a square fractal surface with $N + 1 = 513$ pixels on each side is shown in Fig. 2.2(a). Note that the fractal surface should not be confused with the actual cloud shape. Rather, it is an intermediate mathematical artifact that allows cloud shadows to be generated by intersecting the fractal surface with a horizontal plane of height h . The pixels where the fractal surface is below h are shaded (black area in Fig. 2.2(b)). The cloud cover R is defined as the percentage of the ground area covered by cloud shadow. Cloud shadow patterns with increasing cloud cover can be generated by raising the cutting plane from the bottom to the top of the fractal surface. The R - h map corresponding to this fractal surface is shown in Fig. 2.3.

Algorithm 1 describes the process to construct an elongated fractal surface consisting of F square frames. The main idea is to execute the “canonical” midpoint displacement algorithm for F times, where F is determined by the simulation duration and cloud velocity, as explained in Section 2.2.3. To ensure continuity between frames, all points on the left edge of a new frame are assigned the same fractal value as the corresponding points on the right edge of the previous frame. Some details worthwhile to note are: (i) The fractal dimension change from D_1 to D_2 occurs when the stage is $M' = 4$, with $s = 7$ m and $N = 512$, as suggested by [30]. (ii) The parameter σ is arbitrarily assigned and can be any positive number. Here, we are using $\sigma = 10$. (iii) For the sake of brevity, the algorithm only describes in detail how to obtain the midpoint of the upper edge; the other three edges are found in a similar manner.

2.2 Proposed Model

This section describes subsequent steps that are taken once a fractal surface has been obtained using the midpoint displacement algorithm. Solar irradiance data have been col-

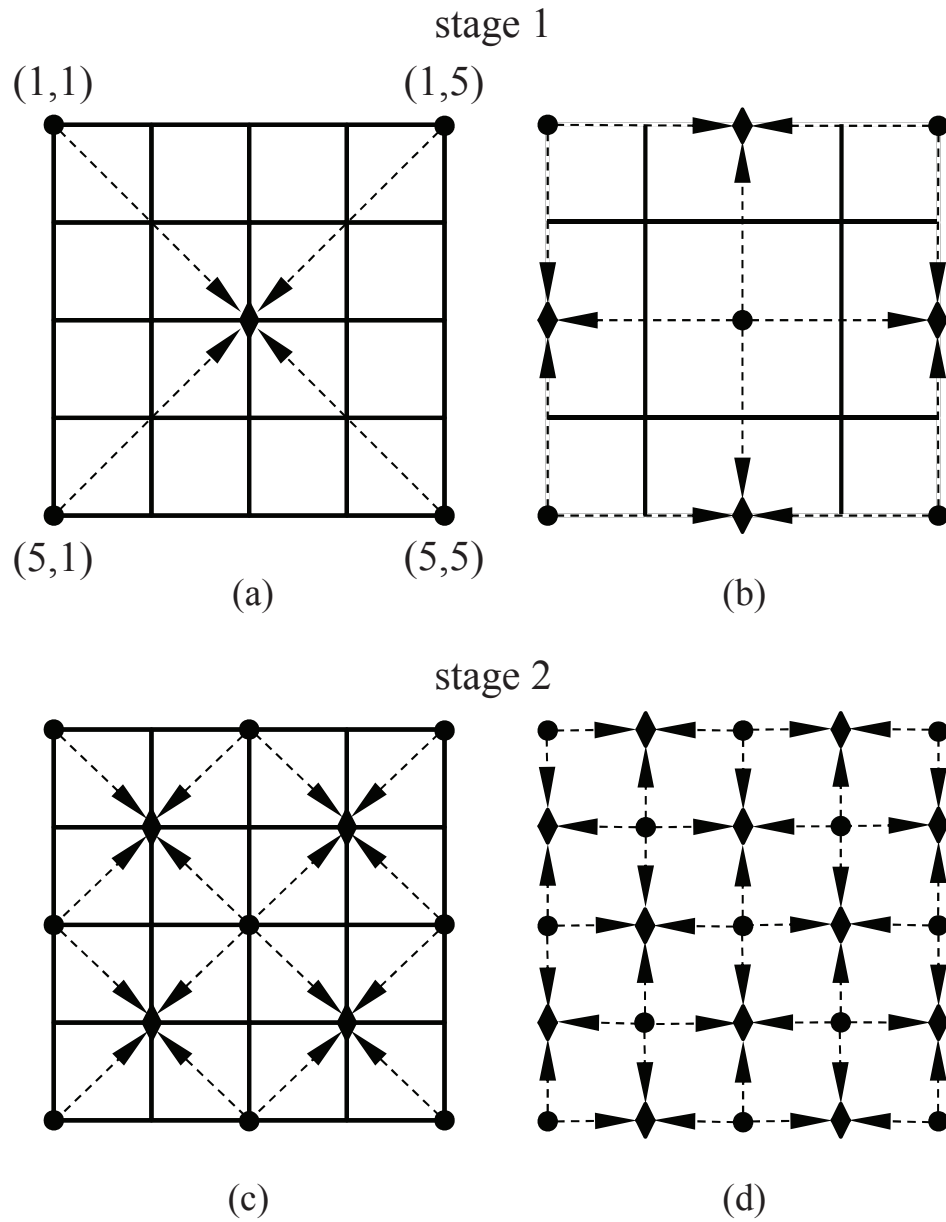
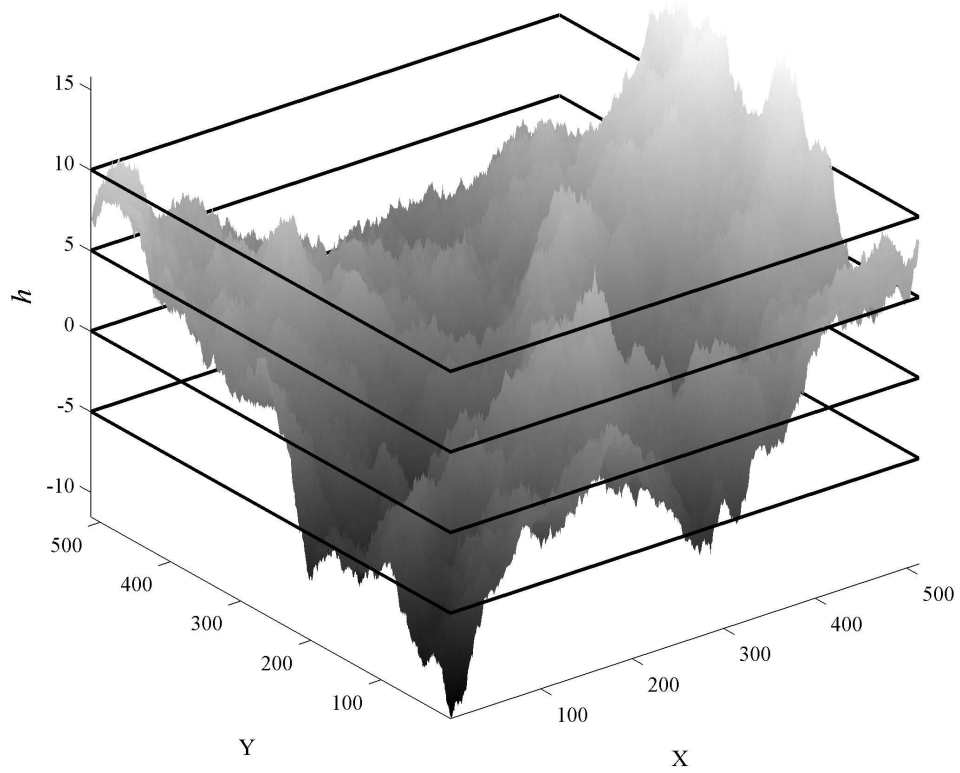
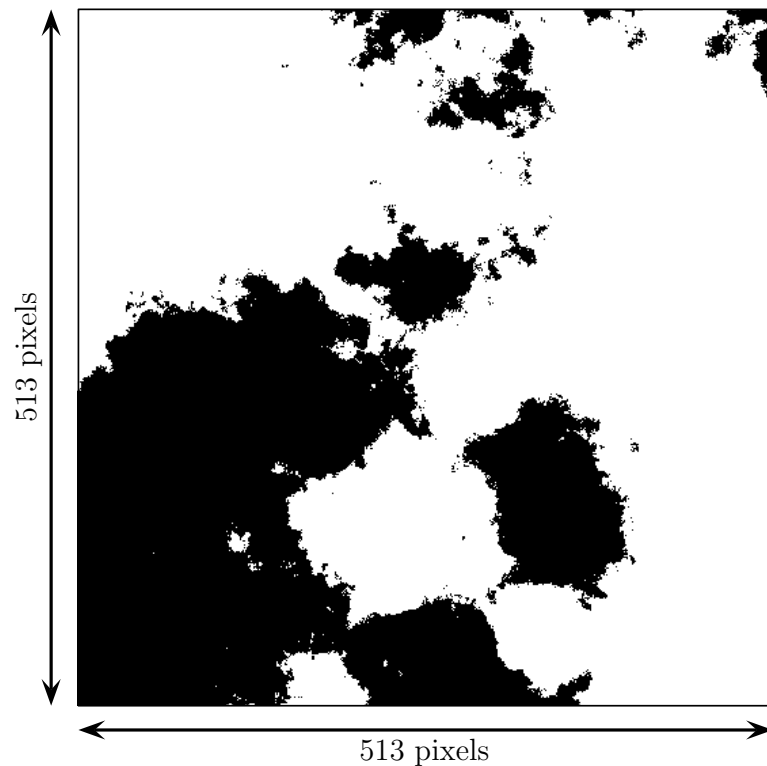


Figure 2.1: Illustration of the midpoint displacement algorithm.



(a)



(b)

Figure 2.2: (a) 513-by-513 fractal surface. Solid lines represent cutting planes of different height. (b) Cloud shadow pattern obtained with $h = 0$.

Algorithm 1 Modified midpoint displacement algorithm

$P \leftarrow$ empty $(N + 1) \times (N + 1)F$ matrix
for $i = 1$ **to** F **do**
 $D \leftarrow D_1$; $X \leftarrow$ empty $(N + 1) \times (N + 1)$ matrix
 if i equals 1 **then**
 $X(1, 1) \leftarrow \mathcal{N}(0, \sigma^2)$; $X(1, N + 1) \leftarrow \mathcal{N}(0, \sigma^2)$
 $X(N + 1, 1) \leftarrow \mathcal{N}(0, \sigma^2)$; $X(N + 1, N + 1) \leftarrow \mathcal{N}(0, \sigma^2)$
 else
 $X(N + 1, N + 1) \leftarrow \mathcal{N}(0, \sigma^2)$; $X(1, N + 1) \leftarrow \mathcal{N}(0, \sigma^2)$
 Make the first column of X in stage i equal to
 the last column of X in stage $i - 1$ (stored in P)
 end if
 $\delta \leftarrow 0.5^{0.5(2-D)}\sigma$
 for $ii = 1$ **to** M **do**
 if $ii \geq M'$ **then**
 $D \leftarrow D_2$
 end if
 $x_c \leftarrow$ empty vector with length of 4^{ii-1}
 $y_c \leftarrow$ empty vector with length of 4^{ii-1}
 $d \leftarrow 2^{M-ii}$; $j \leftarrow 1$
 for $jj = 1$ **to** 2^{ii-1} **do**
 $y \leftarrow 2^{M-ii} + 2^{M-ii+1}(jj - 1) + 1$
 for $k = 1$ **to** 2^{ii-1} , step 1 **do**
 $x \leftarrow 2^{M-ii} + 2^{M-ii+1}(k - 1) + 1$
 $X(x, y) \leftarrow [X(x + d, y + d) + X(x + d, y - d) + X(x - d, y + d) + X(x - d, y - d)]/4$
 $+ \mathcal{N}(0, \delta^2)$
 $x_c(j) \leftarrow x$; $y_c(j) \leftarrow y$; $j \leftarrow j + 1$
 end for
 end for
 $\delta \leftarrow 0.5^{0.5(2-D)}\delta$
 for $kk = 1$ **to** length of x_c **do**
 $x \leftarrow x_c(kk)$; $y \leftarrow y_c(kk)$
 if $x - d$ equals 1 and $X(x - d, y)$ is empty **then**
 $X(x - d, y) \leftarrow [X(x, y) + X(x - d, y - d) + X(x - d, y + d)]/3 + \mathcal{N}(0, \delta^2)$
 else
 $X(x - d, y) \leftarrow [X(x, y) + X(x - d, y - d) + X(x - d, y + d) + X(x - 2d, y)]/4 + \mathcal{N}(0, \delta^2)$
 end if
 The midpoints on the other 3 edges are calculated in a similar manner.
 end for
 end for
 Assign X to the $(i - 1)(N + 1) + 1, \dots, i(N + 1)$ columns of P
end for

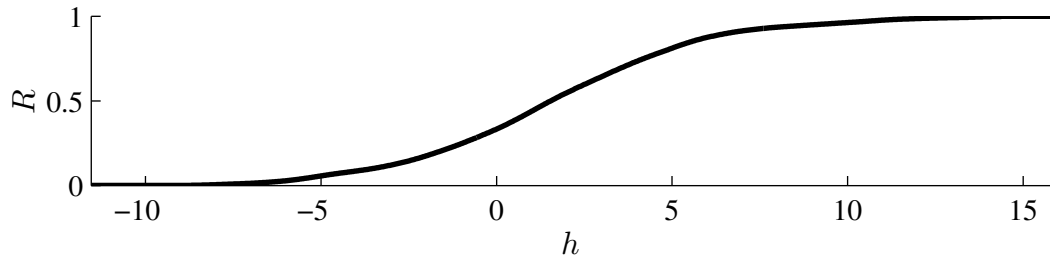


Figure 2.3: Relationship between the cutting surface height (h) and the cloud cover (R).

lected with an experimental station at Iowa State University (ISU) located at $42^{\circ}1'42.74''$ N, $93^{\circ}39'3.88''$ W. The experimental station consists of two PV panels with total rating of 270 Wp and maximum power-point tracking capability. Various sensors are monitoring the system's performance, including a LI-COR LI-200 pyranometer that measures the global horizontal irradiance.

2.2.1 Solar Irradiance Characteristics

The global irradiance consists of a beam (also called direct) and a diffuse component [52]. The beam component is directly and considerably affected by cloud shading, by a factor that depends on the thickness and type of cloud. The diffuse component is determined by numerous atmospheric factors, such as the cloud cover and the cloud type. The proposed solar irradiance model treats these two components separately. The beam component is determined by multiplying the maximum (clear sky) beam normal irradiance value with a factor related to the severity of shading at each location, yielding relatively fast transients. Our model is able to reproduce this type of behavior. Experimental and simulated time-domain waveforms and statistics are compared in a subsequent section. On the other hand, the diffuse component is assumed to maintain a user-defined constant value or a slowly-varying time profile, which is assumed to be the same for the entire area.

Our experimental setup has gathered many months' worth of global horizontal irradiance data, logged at 1-s intervals. An example is shown as the solid line in Fig. 2.4(a). Time segments from days with cumulus clouds are selected with the help of a sky camera installed on the ISU campus [53]. When the shading is caused by an opaque cloud, the beam component

drops considerably to a minimum. This usually happens repeatedly over the course of a few minutes, allowing the estimation of the diffuse horizontal irradiance level, plotted as the dotted line in Fig. 2.4(a). Hence, the beam horizontal irradiance is obtained by subtracting the diffuse component from the global irradiance. The beam normal irradiance is further obtained by dividing the beam horizontal irradiance by the cosine of the zenith angle (Fig. 2.4(b)) [52].

The beam normal irradiance (solid line in Fig. 2.4(c)) is further digitized, in order to extract the duration and magnitude of each shaded period. A shaded period is thought to occur whenever the beam normal irradiance level drops below $L \cdot G_{\text{clear,avg}}$, where L is a constant and $G_{\text{clear,avg}}$ is the averaged beam normal irradiance level for all clear periods within the entire data segment. In this analysis, $L = 0.85$, and the threshold is plotted as the dotted line in Fig. 2.4(c). This process yields the digital shading sequence shown in Fig. 2.4(d).

Two quantities are used to capture the statistical properties of the shading sequence on the beam normal irradiance, namely, the duration of a shaded period T_{shaded} and the normalized magnitude of the shaded period $G_{\text{shaded,n}}$. The latter is defined by $G_{\text{shaded,n}} = G_{\text{shaded}}/G_{\text{clear,avg}}$, where G_{shaded} is the averaged beam normal irradiance level for a particular shaded period. From the data, it can be observed that the majority of the shorter shaded periods have duration less than 200 s. Longer shaded periods ($T_{\text{shaded}} > 200$ s) are due to large opaque and/or slowly moving cumulus clouds. The variation of $G_{\text{shaded,n}}$ is within 5% to 90% for short shaded periods, and within 10% to 25% for longer shaded periods. Therefore, shaded periods with durations less than 200 s are more interesting from a modeling standpoint. Their statistics are plotted in Fig. 2.5.

2.2.2 Meteorological and Geographic Parameters

To generate the cloud shadow pattern for a given time span, the model requires two meteorological parameters as functions of time, namely, the cloud cover $R(t)$ and the cloud velocity $v_c(t)$. We lack the necessary instrumentation to measure these meteorological parameters. Hence, for illustration purposes, we utilize data from the National Renewable Energy Laboratory's (NREL) Baseline Measurement System (BMS) [54]. We also assume that cloud veloc-

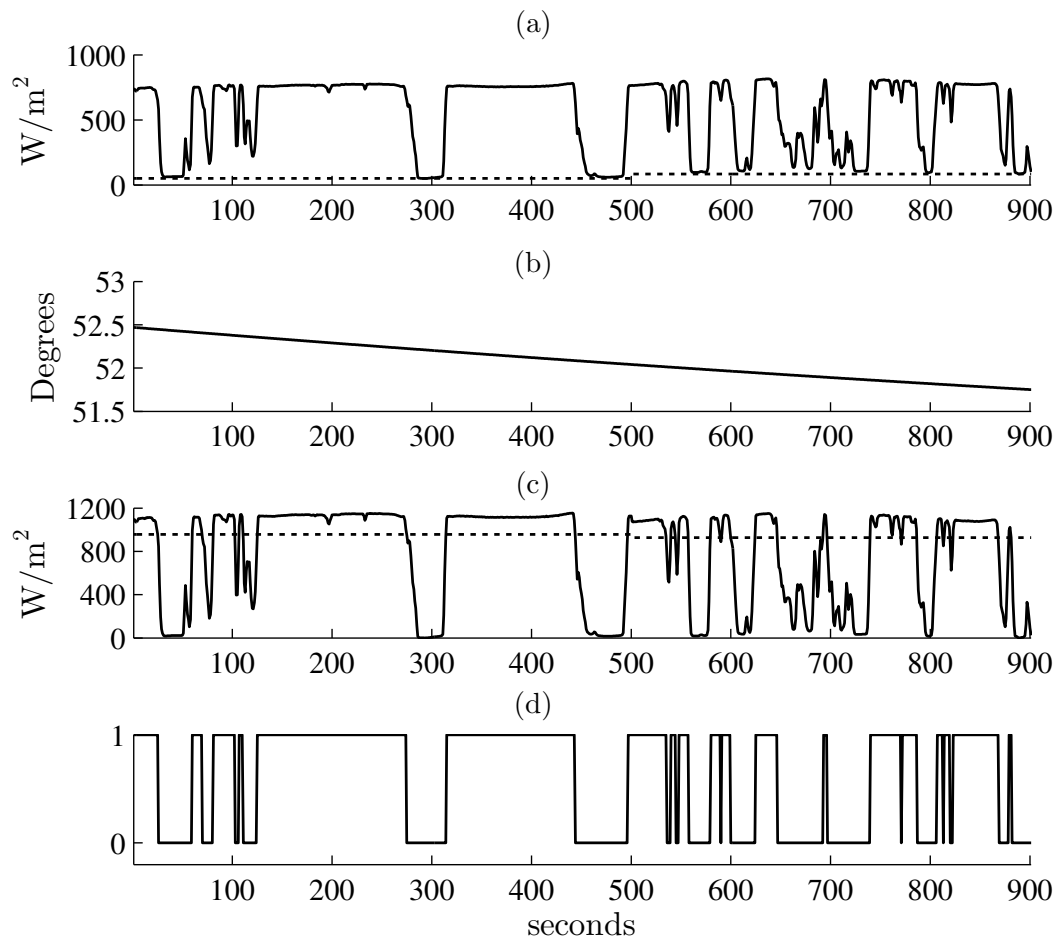


Figure 2.4: (a) Measured global horizontal irradiance (solid) and the estimated diffuse horizontal irradiance (dotted). (b) Zenith angle. (c) Beam normal irradiance (solid) and digitization threshold (dotted). (d) Digitized shading condition.

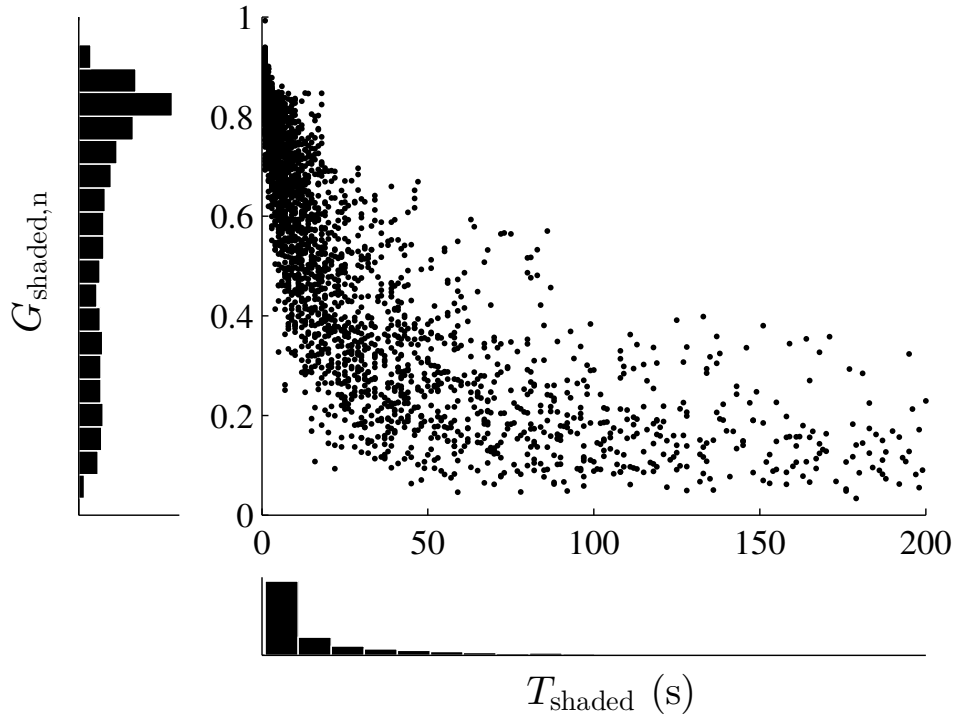


Figure 2.5: Statistics of the beam normal irradiance for shaded periods shorter than 200 s, from experimental measurements.

ity (v_c) is equal to the wind speed at cloud height (v_w). The time resolution of the NREL data is at a 1-min. interval, so it is interpolated into 1-s data to be consistent with the simulation step in the case study. The wind speed data $v_{w,\text{meas}}(t)$ is measured at a height of $H_{\text{meas}} = 42$ ft, and has been modified to reflect the wind speed at a height of $H = 1500$ m (a common height of cumulus clouds [49]) based on the power law equation $v_w(t; H) = v_{w,\text{meas}}(t)(H/H_{\text{meas}})^\lambda$ [55], with $\lambda = 0.155$. It should be noted that these simplifying assumptions are not limitations of the proposed model itself, but rather of the available data for parameterizing the model. The specific waveforms used to generate the cloud shapes in this study are plotted in Fig. 2.6. The wind direction is assumed to remain constant.

The model also requires knowledge of the system's geographic layout. Here, we perform a case study involving a residential community with rooftop PV panels [56]. The exact location of each house is not available, but the coordinates of all service transformers are included in the feeder data, indicated by circles in Fig. 2.7. In the simulation, the irradiance at each

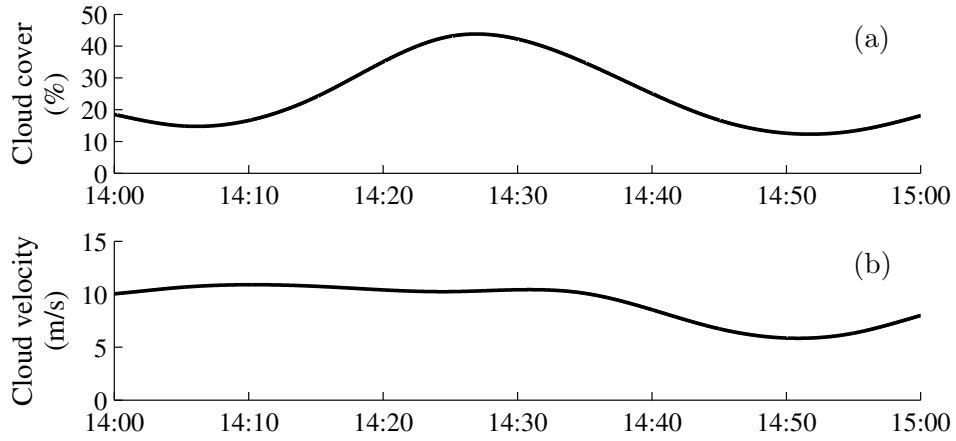


Figure 2.6: Variation of: (a) cloud cover and (b) cloud velocity.

transformer also represents the irradiance received by the PV panels at its immediate vicinity. The shading condition of each point is obtained by virtually moving the generated cloud shadow over the area under study. To account for the wind direction, the PV system layout is rotated accordingly, as shown in Fig. 2.8, which depicts the cloud shadow pattern between 2:00 and 3:00 PM.

2.2.3 Cloud Shadow Pattern Generation

The canonical midpoint displacement algorithm has been modified to generate the cloud shadow pattern for a rectangular (i.e., not necessarily square) area, as described by Algorithm 1. Consecutive square frames are generated and are stitched together at their boundaries. To ensure continuity between frames, all points on the left edge of a new frame are assigned the same fractal value as the corresponding points on the right edge of the previous frame. The modified algorithm needs to know the number F of square frames to generate, which depends on the time span of the simulation and the cloud velocity. Let t_s and t_e denote the start and end times of the study, and let Δt be a simulation time step, so that $t_s = k_s \Delta t$ and $t_e = k_e \Delta t$ for appropriate integers k_s and k_e . The cloud shadow is moved to the left at times $t_k = k \Delta t$ by an amount equal to $\Delta x(t_k) = v_c(t_k) \Delta t$, where $k_s \leq k < k_e$. Then F can be determined by

$$F = \text{ceiling} \left(\frac{\sum_{k=k_s}^{k_e-1} v_c(t_k) \Delta t}{(N+1)s} \right) + 1. \quad (2.1)$$

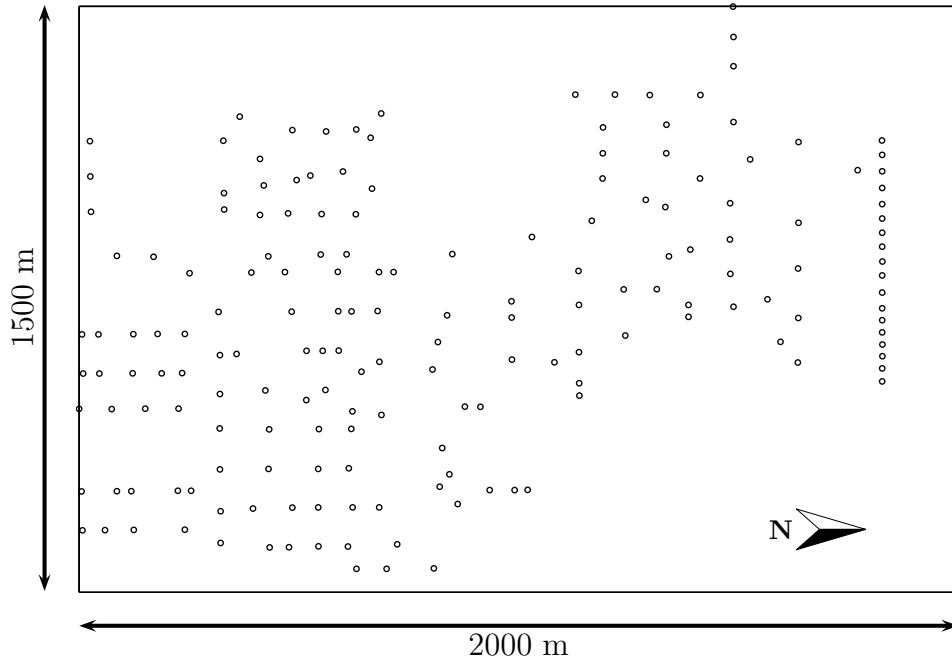


Figure 2.7: Geographic layout of measurement points.

In our case study, $\Delta t = 1$ s, and $F = 11$ frames were necessary.

In the canonical midpoint displacement method described in Section 2.1, a square $(N + 1) \times (N + 1)$ fractal surface S_{frac} is generated first; then S_{frac} is intersected with a horizontal cutting plane S_{cut} of height h . The contour of the intersection generates a static cloud shadow pattern for this square area associated with a given cloud cover R . On the other hand, the proposed model generates a rectangular, $(N + 1) \times ((N + 1)F)$ cloud shadow pattern for a variable cloud cover $R(t)$. This is achieved by intersecting S_{frac} with a non-horizontal S_{cut} surface, which is stored as a matrix with $N + 1$ identical rows but different elements in each of its $(N + 1)F$ columns.

Fig. 2.9 graphically demonstrates the technique used to obtain the cutting surface. The light dashed lines represent the frames of the generated fractal surface S_{frac} . A new square $(N + 1) \times (N + 1)$ “horizon-defining” window is created every 1 minute, according to the cloud velocity, so that the center of area \mathbf{A} is always at a window’s center. In general, these windows will not coincide with the F frames generated by the midpoint displacement algorithm, even though they have the same dimension as each frame (only the first window coincides with the

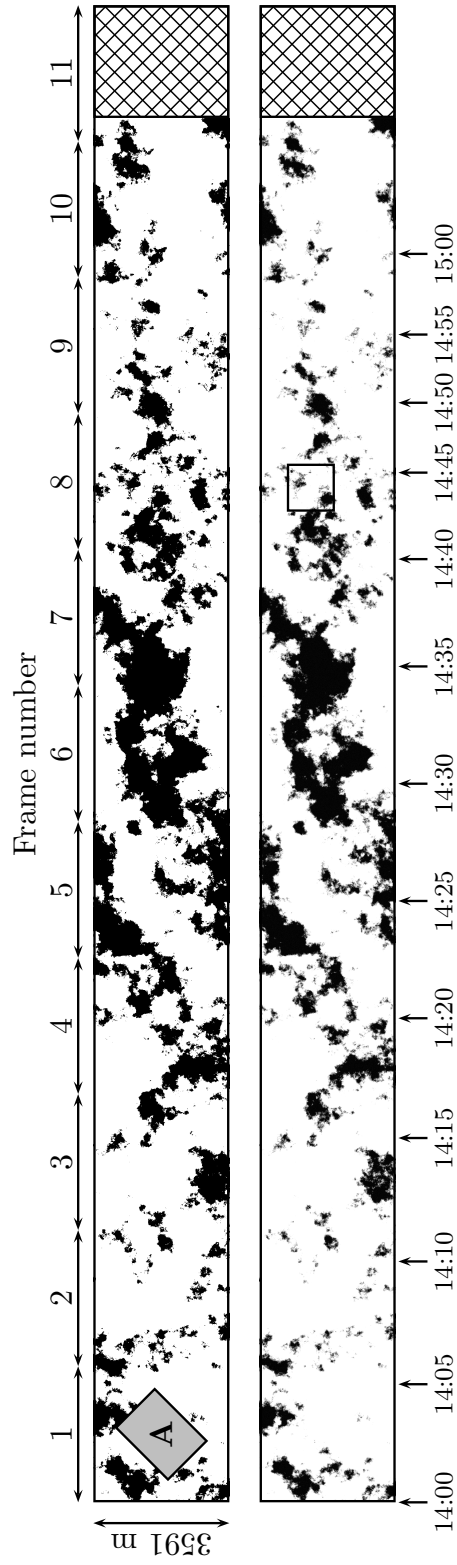


Figure 2.8: (Top) Generated binary cloud shadow pattern for time period between 2:00 and 3:00 PM. The wind direction is SW. **A** is the study area. (Bottom) Final cloud shadow pattern, using a multi-layer rendering technique. The pixels of the hatched area on the right were not needed in this simulation.

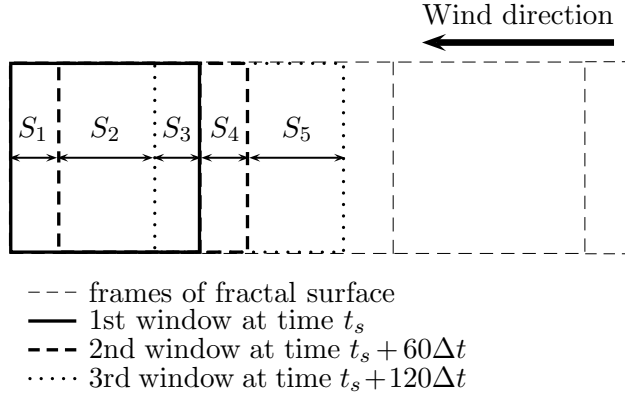


Figure 2.9: Windows and strips for the calculation of the cutting surface.

first frame). The problem is to determine the appropriate h value for each column in the cutting matrix, so that the number of clouded pixels within the window is equal to $R(t_w) \cdot (N + 1)^2$, at times $t_w = t_s + 60w\Delta t$, $w = 0, 1, 2, \dots$

Each consecutive window leads to the formation of a strip, as shown in Fig. 2.9. We define n_i as the number of clouded pixels in strip S_i . In this illustration, the first window consists of three strips, S_1 , S_2 , and S_3 . The h value for all pixels in the first window (i.e., the first frame) can be determined as discussed in Section 2.1, given $R(t_s)$. The h value for pixels belonging to the second window, which consists of S_2 , S_3 , and S_4 , is calculated next. Since the clouded pixels in strips S_2 and S_3 have been already determined, we only need to determine the h value for pixels in S_4 , such that $n_2 + n_3 + n_4 = R(t_s + 60\Delta t) \cdot (N + 1)^2$. To find n_4 , the fractal surface corresponding to S_4 is intersected by a horizontal surface of increasing height, until n_4 satisfies this equation. Similarly, for the third window, which consists of S_3 , S_4 , and S_5 , we find the h value that yields the required n_5 . This process is repeated until the simulation end time.¹ In order to eliminate discontinuities between strips, an interpolation is further performed. Instead of using the same h value for entire strips (i.e., ranges of columns in the S_{cut} matrix), the values of h thus obtained are only assigned to the middle column of each strip, and the values for the remaining columns are obtained by linear interpolation, as illustrated in Fig. 2.10. This process yields the binary cloud shadow pattern of Fig. 2.8 (top), where the black pixels represent the shadow.

¹The rounding operations needed to obtain integer numbers of pixels and strip-defining column ranges are not explicitly shown for expositional clarity.

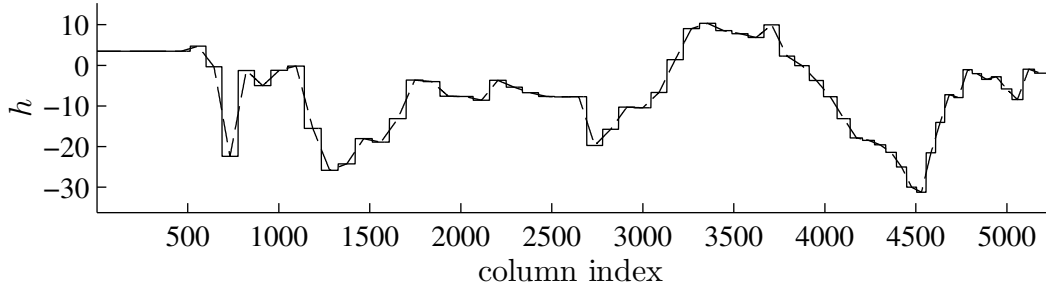


Figure 2.10: Comparison of the cutting surface height before and after interpolation.

The final step is to represent the thickness of clouds. This effect has been often neglected in previous studies, thus resulting in simulated solar irradiance that drops or rises vertically, contradicting with experimental observations. To this end, a computationally efficient multi-layer rendering technique is devised. The objective is to obtain statistics of beam irradiance that are qualitatively similar to the experimental results (see Fig. 2.5). These statistics reveal that faster variations usually correspond to less severe shading (probably due to shading by the peripheral parts of the clouds or by smaller clouds). On the other hand, moderate to complete shading conditions correspond to slower variations (probably caused from the inner, thicker parts of larger clouds).

The surface S_{cut} that has been determined by the previously illustrated technique defines the external boundary of the cloud shadow. Afterwards, new cutting surfaces are formed by repeatedly lowering the height of S_{cut} by a factor $l = (h_{\text{max}} - h_{\text{min}})/\alpha$, where h_{max} and h_{min} represent the highest and lowest elevation of the fractal surface S_{frac} . If K layers are to be used, $K - 1$ extra cutting surfaces below the original one are formed. The cloud shadow pixels belonging to the k -th layer are assigned a random number using a uniform distribution $\mathcal{U}(a, b)$, where $a = (k - 1)/K$, $b = k/K$, and $k = 1, 2, \dots, K$. These values are representative of the cloud's thickness, and are stored in an $(N + 1) \times ((N + 1)F)$ shading matrix S_{cloud} . In this illustrative example, $\alpha = 400$ and $K = 21$. The obtained cloud shadow pattern is shown in Fig. 2.8 (bottom), and a magnified portion of this (indicated by a small box around 14:45) is displayed in Fig. 2.11. The figures are in gray scale; darker pixels correspond to increased shading.

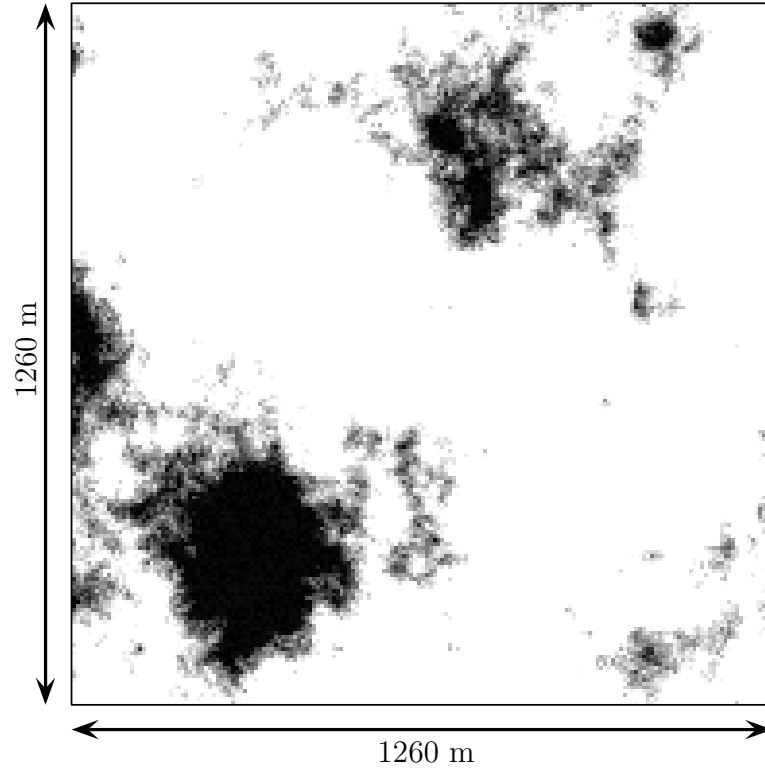


Figure 2.11: Magnified cloud shadow pattern.

2.2.4 Synthesis of the Irradiance Time Series

Moving the cloud shadow pattern over the study area (under the assumption that the study area has been rotated so that the cloud moves over it from “right” to “left”) is equivalent to sampling pixel values from the cloud shading sequence stored in S_{cloud} . For a given measurement point p on the ground, the shading level $s_p(t_k)$ is obtained by sampling values from the appropriate row and column of S_{cloud} , which are determined by the geographic location of the point (affecting the row and column offset) and the cloud velocity. Thanks to the rotation of the study area, the row index for a given point will be constant. The factor $[1 - s_p(t_k)]$ represents a cloud transparency level (see Fig. 2.12(a)).

The global horizontal irradiance for point p at time t_k is

$$G_{gh,p}(t_k) = [1 - s_p(t_k)] \cdot G_{cbh}(t_k) + G_{dh}, \quad (2.2)$$

where G_{cbh} (see Fig. 2.12(b)) is the maximum beam irradiance that can be received by a horizontal surface under fully clear condition, calculated using classical formulas [52]; and G_{dh}

is the diffuse horizontal irradiance. In this case study, G_{dh} has a constant value (179 W/m^2) over the entire simulation period, but it could have been defined as time-varying. Fig. 2.12(c) shows the final synthesized solar irradiance time series for an arbitrarily selected measurement point, and Fig. 2.13 shows a magnified 15 minute-long portion of the waveform to illustrate the similarity with experimental measurements (cf. Fig. 2.4(a)). All other measurement points exhibit similar patterns. The spatially averaged solar irradiance over all measurement points within the study area is depicted in Fig. 2.12(d). As expected, the variability of the irradiance decreases considerably, compared with the variability of single-point measurements. Note that Fig. 2.12(d) shows the irradiance variation corresponding to a single realization of a fractal cloud shadow, i.e., the one shown in Fig. 2.8. To estimate the sample mean of spatially averaged irradiance, 100 Monte Carlo simulations have been conducted, where each simulation uses a different fractal. It is interesting to observe that the spatially averaged irradiance of individual simulations (Figs. 2.12(d)–(g)) can be substantially different from the sample mean (Fig. 2.12(h)), which resembles more closely the smooth cloud cover variation of Fig. 2.6(a). The small decrease from 14:00 to 15:00 in Fig. 2.12(h) is due to the movement of the sun over that one hour. Statistics for the simulated irradiance for all measurement points are shown in Fig. 2.14(a). A visual comparison of this plot with Fig. 2.5 shows that the proposed model is able to qualitatively reproduce the statistical properties of the measured data.

2.3 Sensitivity Analysis

The sensitivity of the model's output with respect to changes in meteorological parameters is examined via four additional case studies. These are based on the original case, whose cloud cover and cloud velocity waveforms are modified by $\pm 10\%$ and $\pm 5 \text{ m/s}$, respectively. The statistics are plotted in Fig. 2.14, from which the following may be observed: (i) The cloud cover has a significant impact on the number of shaded periods with relatively longer durations ($> 100 \text{ s}$) and low irradiance. (ii) Changes in cloud velocity tend to stretch the statistics along the horizontal axis, thus directly affecting the duration of shaded periods.

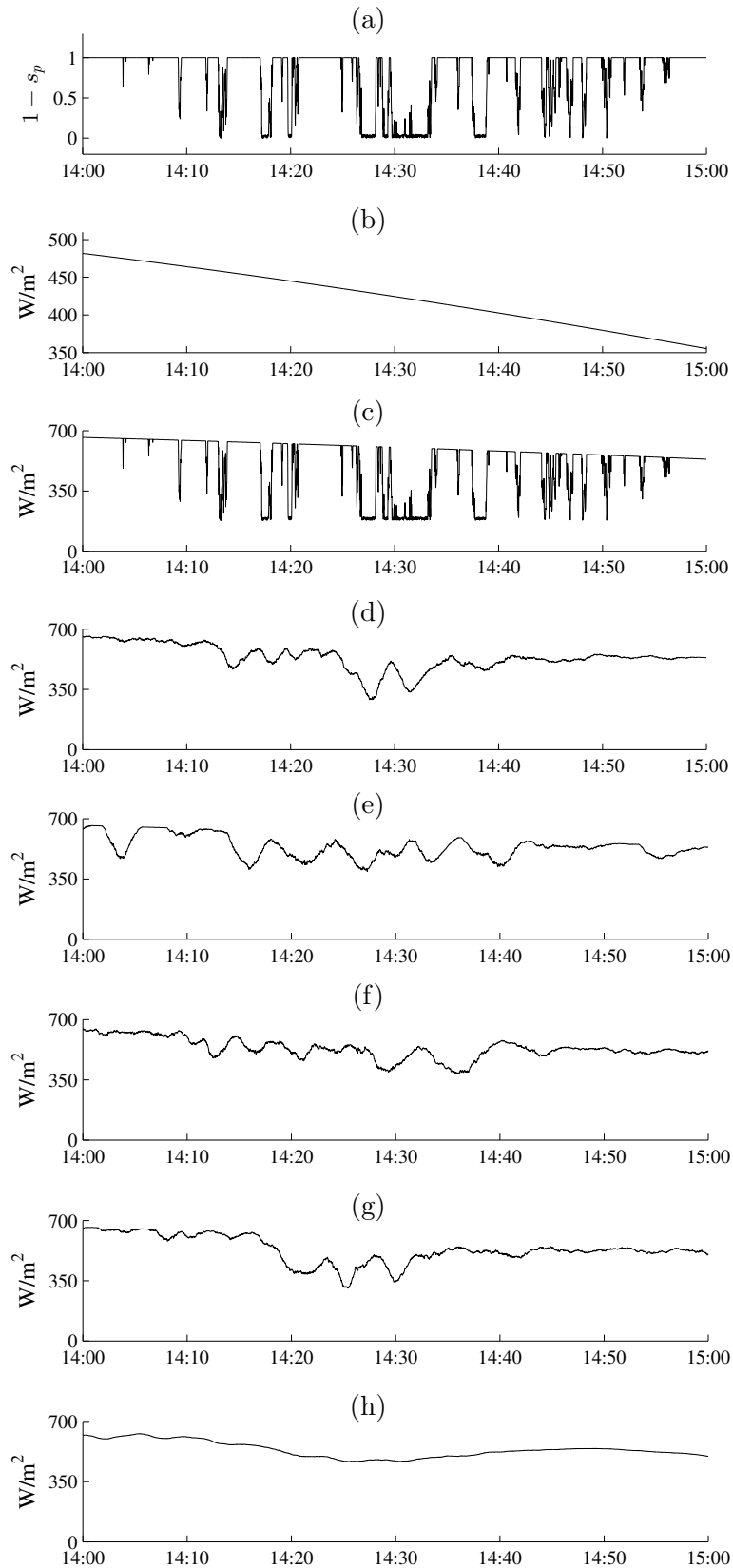


Figure 2.12: (a) Cloud transparency level. (b) Beam horizontal irradiance under clear sky condition. (c) Synthesized global horizontal irradiance time series. (d) Spatially averaged irradiance time series for the cloud shadow of Fig. 2.8. (e)–(g) Spatially averaged irradiance time series for three other fractals. (h) Sample mean of spatially averaged irradiance time series for 100 Monte Carlo simulations.

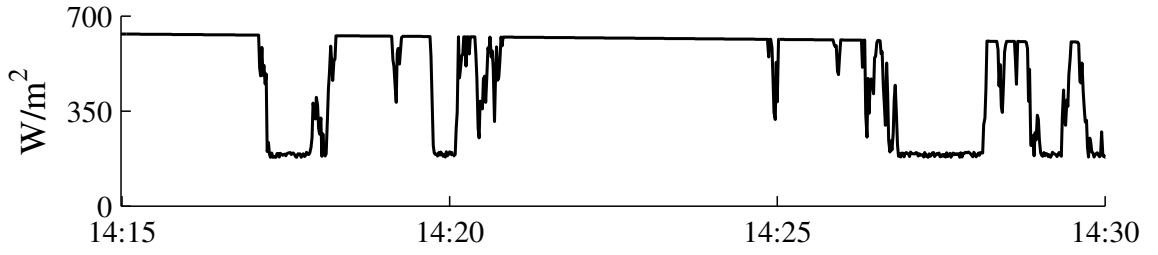


Figure 2.13: Magnified global horizontal irradiance time series.

Table 2.1: Computing times

Case	F	T_{frac} (s)	T_{cut} (s)	T_{render} (s)
(a)–(c)	11	5.50	0.87	1.02
(d)	16	7.98	1.09	1.71
(e)	6	2.86	0.58	0.63

2.4 Computational Requirements

The computing time required for completing the aforementioned five sensitivity case studies is presented in Table 2.1. The studies were run on a PC with an Intel i7 2.2-GHz CPU. The table lists the average times required for completing the three main steps of the proposed algorithm, T_{frac} , T_{cut} , and T_{render} , for generating the fractal surface, generating the cutting surface, and applying the multi-layer rendering technique, respectively. The proposed model is computationally efficient, and suitable for use in Monte Carlo simulations of distribution feeders.

2.5 Model Tuning

A practical method for tuning the parameters of the proposed model can be based on data that are commonly available from public weather stations, namely, hourly cloud cover, ground-level wind speed, and cloud height data. We use the weather station in Ames Municipal Airport, Iowa, USA [57]. The cloud velocity is estimated using the power law equation $v_c(t; H) = v_{w, \text{meas}}(t)(H/H_{\text{meas}})^\lambda$, using the ground-level wind speed and cloud height data. The exponent λ is the first tuned parameter. The second tuning parameter is α , which is

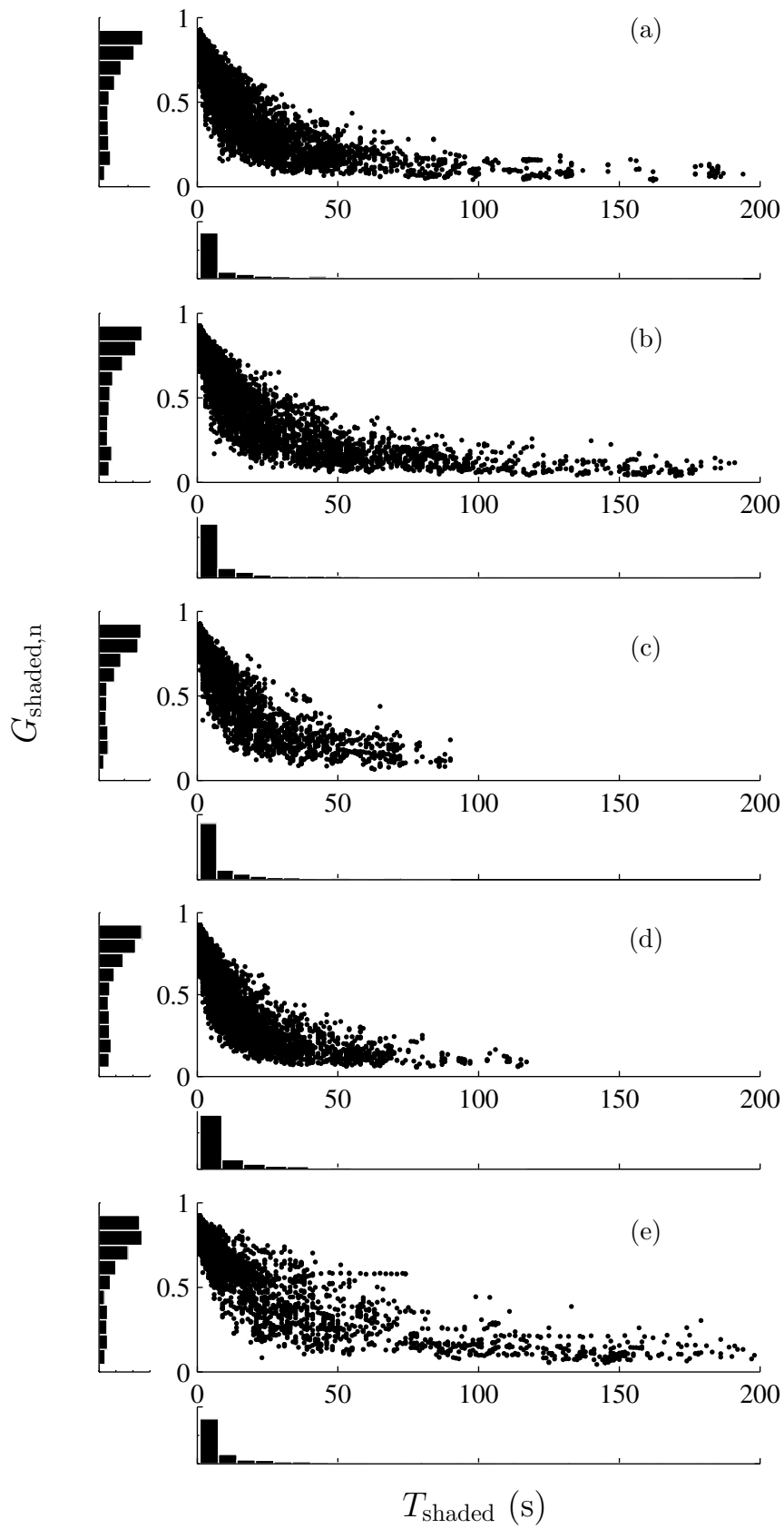


Figure 2.14: Statistics of the simulated beam normal irradiance. (a) base case; (b) $R(t_k) + 10\%$; (c) $R(t_k) - 10\%$; (d) $v_c(t_k) + 5 \text{ m/s}$; (e) $v_c(t_k) - 5 \text{ m/s}$.

Table 2.2: Statistical measures of experimental data

	T_{shaded}		$G_{\text{shaded},n}$	
	High	Low	High	Low
μ	32.65	40.88	0.5088	0.5573
σ^2	4272	7444	0.0653	0.0615
γ	4.61	4.39	-0.266	-0.5538

used in the multi-layer rendering technique. The tuning aims to provide a reasonably good match between the measured and simulated statistics of duration and normalized magnitude of shaded periods, T_{shaded} and $G_{\text{shaded},n}$, respectively.

For analysis, the irradiance data measured by our experimental station is divided into a high wind speed and a low wind speed group, based on average ground-level wind speed, using a threshold of 8 m/s. Table 2.2 shows the mean (μ), variance (σ^2), and skewness (γ) of the two groups of data. It can be observed that both the mean and variance of T_{shaded} decrease with higher cloud velocity, as expected.

First, the parameter α is fixed to a value of 400, and only λ is adjusted. All other parameters are kept constant, using previously defined values. Then, Monte Carlo simulations are conducted using the data retrieved from the weather station for the same time periods as the measured data. Fig. 2.15 shows the effect of λ on the statistics of T_{shaded} . It can be observed that as the cloud velocity increases (i.e., for higher λ), the model tends to produce shaded periods with shorter duration. The tuning process shows that $\lambda = 0.155$ is a reasonably good value, leading to $\mu_H = 32.86$, $\sigma_H^2 = 3371$, $\gamma_H = 3.29$, and $\mu_L = 44.35$, $\sigma_L^2 = 9332$, $\gamma_L = 4.79$. Fig. 2.16 further compares the cumulative distribution function of T_{shaded} from simulations (with $\lambda = 0.155$) and measurement.

Next, the tuning of α takes place. Simulations are run with $\lambda = 0.155$ and other parameters kept fixed. Fig. 2.17 shows how the statistics of $G_{\text{shaded},n}$ are affected by α . Selecting $\alpha = 275$ leads to $\mu_H = 0.5008$, $\sigma_H^2 = 0.0713$, $\gamma_H = -0.3423$, and $\mu_L = 0.5488$, $\sigma_L^2 = 0.0705$, $\gamma_L = -0.642$. Fig. 2.16 shows a comparison of the cumulative distribution of $G_{\text{shaded},n}$ from simulations (with

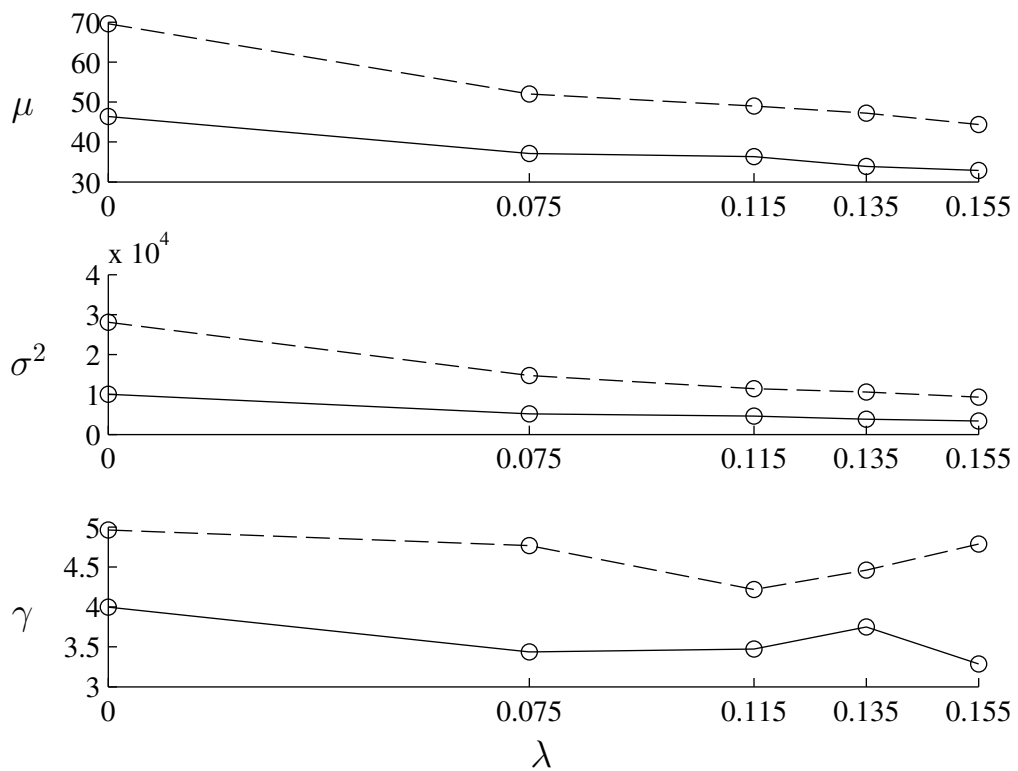


Figure 2.15: Variation of statistical measures of T_{shaded} with λ . Solid line: high wind speed; dashed line: low wind speed.

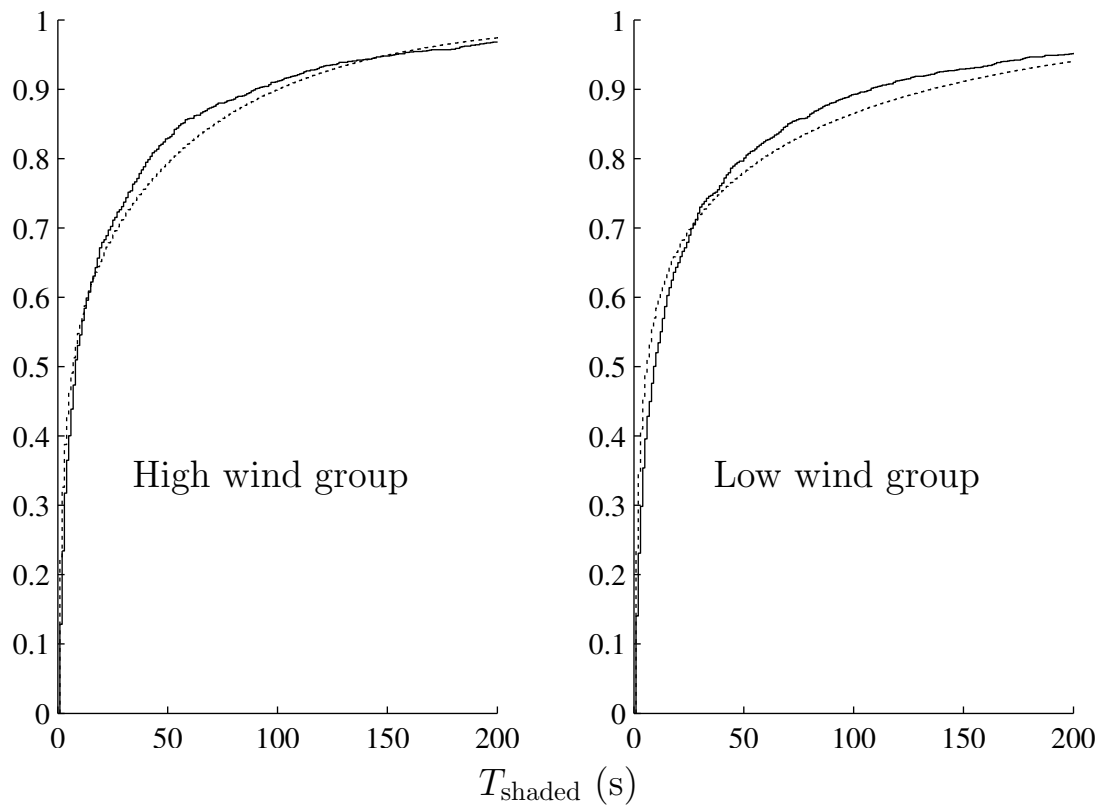


Figure 2.16: Comparison of the cumulative distribution function of T_{shaded} from simulations (dashed line) and measurements (solid line). (Note that the shading duration can exceed 200 s in some cases, so the CDF reaches a value slightly lower than 1 in this plot.)

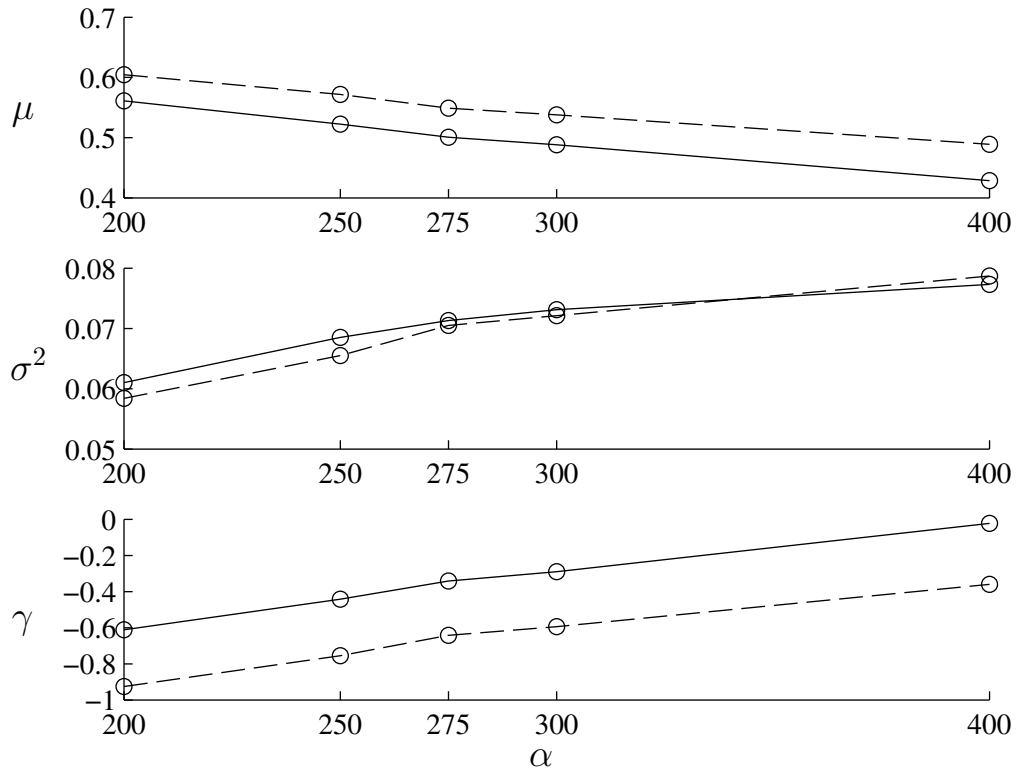


Figure 2.17: Variation of statistical measures of $G_{\text{shaded},n}$ with α . Solid line: high wind speed; dashed line: low wind speed.

$\alpha = 275$) and measurement.

After tuning α , the statistics of T_{shaded} will be slightly affected, so it might be necessary to iterate until a more satisfactory combination of λ and α is found. The other parameters used in the fractal generation (i.e., D_1 , D_2 , s , and N) can also be adjusted based on captured cloud images, using the image processing method described in [30].

2.6 Model Summary

In summary, the proposed model proceeds as follows:

1. Determine the geographic parameters of the area containing the PV, including the site's altitude, latitude and longitude, and coordinates of measurement points.
2. Specify the time period of the study, i.e., t_s , t_e , Δt , as well as year, month, and day.

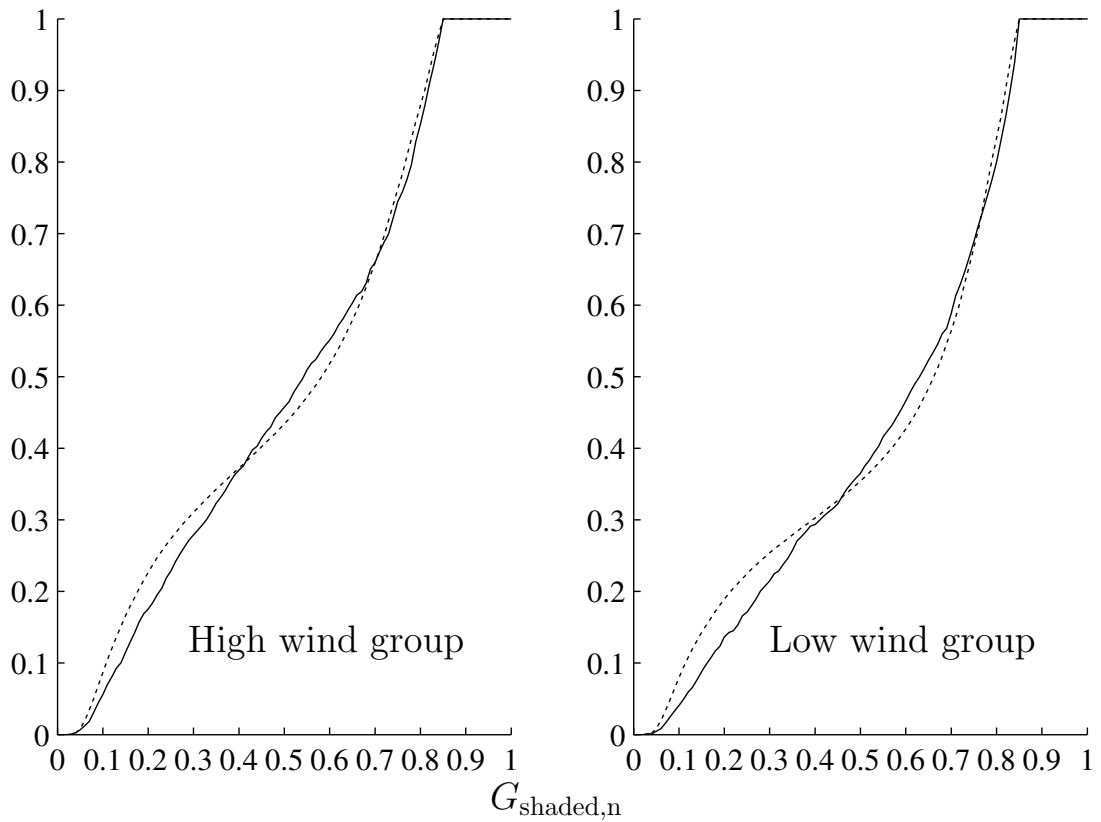


Figure 2.18: Comparison of the cumulative distribution function of $G_{\text{shaded},n}$ from simulations (dashed line) and measurements (solid line).

3. Calculate the clear beam horizontal irradiance $G_{cbh}(t)$ and specify the diffuse horizontal irradiance G_{dh} .
4. Specify the variation of cloud cover $R(t)$ and cloud velocity $v_c(t)$, and a constant direction of cloud movement.² (If not known, cloud velocity time series can be generated using ground-level wind speed measurements and a power law equation with an exponent λ .)
5. Rotate the study area according to the cloud movement direction.
6. Specify the parameters of the fractal cloud shadow model, i.e., D_1 , D_2 , s , N , σ , K , and α .
7. Calculate the number of frames F using (2.1).
8. Use the modified midpoint displacement algorithm to generate the fractal surface S_{frac} .
9. Calculate the cutting surface S_{cut} according to the first half of Section 2.2.3.
10. Apply the multi-layer rendering technique described in the second half of Section 2.2.3 to obtain the shading matrix S_{cloud} .
11. Move the synthesized cloud shadow pattern over the area under study, and obtain the shading sequences for all measurement points $s_p(t_k)$.
12. Convert the shading sequence to an irradiance time series using (2.2).
13. Convert irradiance to electric power output based on specifications of PV systems, e.g., orientation of PV panels, tilt angle, efficiency, sun tracking method, etc [58].
14. Go to step 8) and repeat for the required number of Monte Carlo simulations.

²With a simple modification to the model, allowing for continuous rotation of the area under study, the cloud movement direction would not need to be constant. It is kept constant here for the sake of simplicity.

CHAPTER 3 MODEL APPLICATION TO A CASE STUDY OF LTC OPERATION

3.1 Introduction

Due to the variability of PV generation during cloudy days, the traditional static single-snapshot power flow analysis used in studies of distribution system operation, e.g., focusing on voltage drop along the feeder, is becoming insufficient to reveal how the high penetration of PV could affect the system operation over time. The impact on voltage regulation device switching is of particular interest.

Two key parts are involved in the modeling of distributed PV generation, i.e., the irradiance input and solar-to-power energy conversion process (the electric model of PV modules). The latter has been studied extensively, whereas, the former has not been adequately addressed.

This chapter, through studying the impact of high penetration of PV on LTC (Load Tap Changer) operation, demonstrates a possible scenario where the model presented in the previous chapter can be applicable.

The chapter is organized as follows. A short background on the LTC equipment and a brief introduction to the problem are first given. Then a series of experiments are set up to investigate:

- how the PV generation will affect the LTC operation under different load profile in different seasons, i.e., summer and winter.
- what is the effect of passing by cloud velocity on the LTC operation.
- what is the effect of cloud cover on the LTC operation.

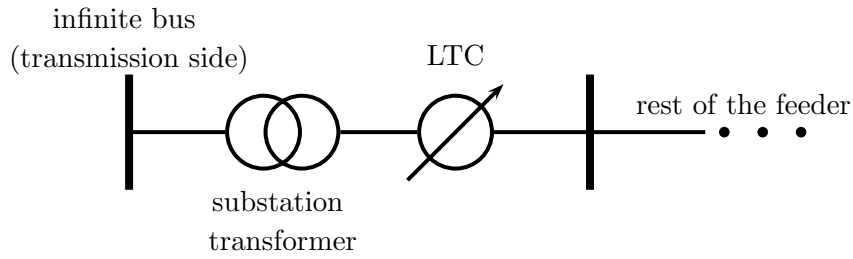


Figure 3.1: Simplified distribution system schematic.

- how the LTC operation pattern is changed by different PV penetration level, i.e., amount of installed capacity of distributed PV systems.

Finally, the proposed fractal-based model is compared with Jewell's model.

3.2 Background on LTC and Problem Definition

The Load Tap Changer (LTC), also called On Circuit Tap Changer or On Load Tap Changer, is essentially a part of the power transformer to regulate the voltage at the substation by adjusting winding turns ratio, as shown in Figure 3.1. In traditional distribution systems without distributed energy sources, with the changing of load level, the current drawn from the transmission side through the substation constantly varies, which leads to the change of secondary voltage at the output terminal of LTC. As a result, a given substation transformer turns ratio cannot guarantee the voltage of the feeder is always maintained within the acceptable range. By mechanically moving the tap inside the LTC to different locations, the turns ratio of the power transformer can be adjusted so that the output voltage can be accordingly set to the desired value range.

Two typical LTC diagrams from [59] are shown in Figure 3.2. The small arrow indicates the tap position on each phase. Based on [59], the common LTC configuration in North America is:

- There are 33 tap positions on each phase. 16 positions for raising up the output voltage and 16 positions for lowering down the output voltage. The one center tap position represents the desired place of the voltage center. A common practice is to label the tap

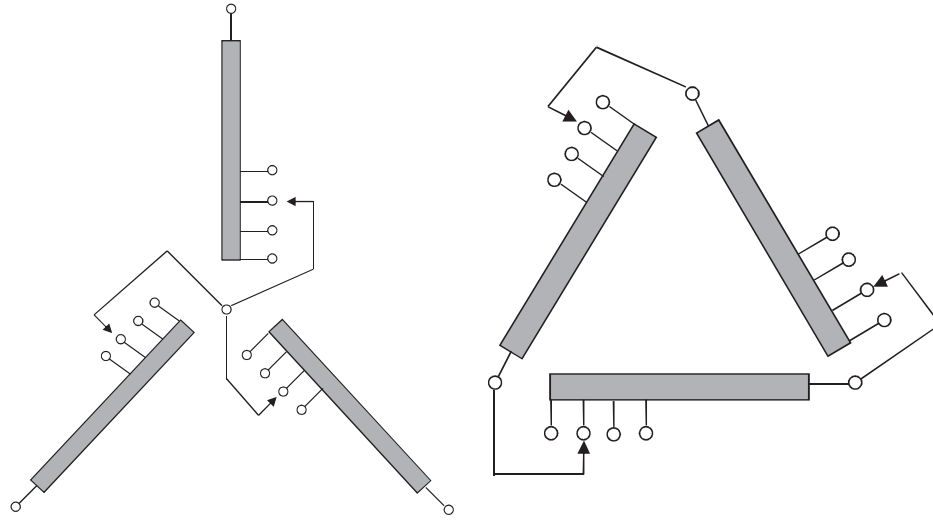


Figure 3.2: Two LTC configuration diagram, Y connection (left) and Delta connection (right).

positions from -16 to +16, where “ - ” is for lowering taps, “ + ” is for raising taps and 0 is for the center tap.

- The voltage control range for each phase is approximately $\pm 10\%$ of the desired voltage center. For example, if the voltage center is set to be 7915 V, then the desired output voltage at the +16 tap position will be $7915 * 1.1 = 8706$ V and the voltage at -16 tap position will be $7915 * 0.9 = 7123$ V.
- Given the voltage center and the voltage control range, the voltage change per tap position can be calculated as $7915 * 0.1/16 \approx 51$ V.

Power transformers with LTC have been used widely in distribution systems for years with well established maintenance procedure and operation experience. However, with the introduction of high penetration of distributed PV generation, the load seen by the substation is experiencing dramatic changes. First, the daily load pattern is reshaped by the PV generation, with some cases that during the generation peak hours, the net real power load measured at the substation can even go to negative, which means the distribution system is feeding power back to the transmission side. Second, due to the intermittency and variability of the PV

generation, the feeder will experience more fluctuations in voltages. These changes will also affect how the LTC operates. The LTC is one of the most expensive and important devices in the distribution system. If not properly inspected and maintained, its life time will be considerably shortened. For those distribution systems with PV penetration still at relatively low level, the LTC operation might not be seriously affected. However, with the premise of increasing penetration of PV as well as other distributed generations, it is important to look ahead on how the high penetration of PV generation could affect the LTC operation under different cloud scenarios and then develop corresponding mitigation methods.

3.3 Simulation Setup

Since the LTC operation is a dynamic behaviour at the time scale of a few seconds, the simulation will need to perform the continuous power flow calculation at small time step. To perform the power flow calculation, three aspects are needed, i.e., distribution network topology, generation and load profile at each node. To this end, this section provides the details on how the simulation environment is set up to study the impact of high penetration of PV on the LTC operation. First, the distribution system used in this study is introduced, followed by the modeling of distributed rooftop PV systems on houses. At last, the simulation parameters and scenario parameters are listed and explained.

3.3.1 Distribution System

The distribution system used in this study is a 13.2 kV feeder with 12 MVA rating capacity [56], where detailed technical data and topology can be found. The distribution feeder serves a residential area in Iowa with some light commercial load. The location of each house and distribution transformer is plotted in Figure 3.3. Each red triangle is a single phase center tapped distribution transformer, connected to houses (black dots) around it by lines. The distribution system is modeled in GridLAB-D, including 1372 house objects and 175 distribution transformer objects. The coordinates of all distribution transformers are provided by the utility and the location of all houses are manually measured in GoogleEarth, as shown in

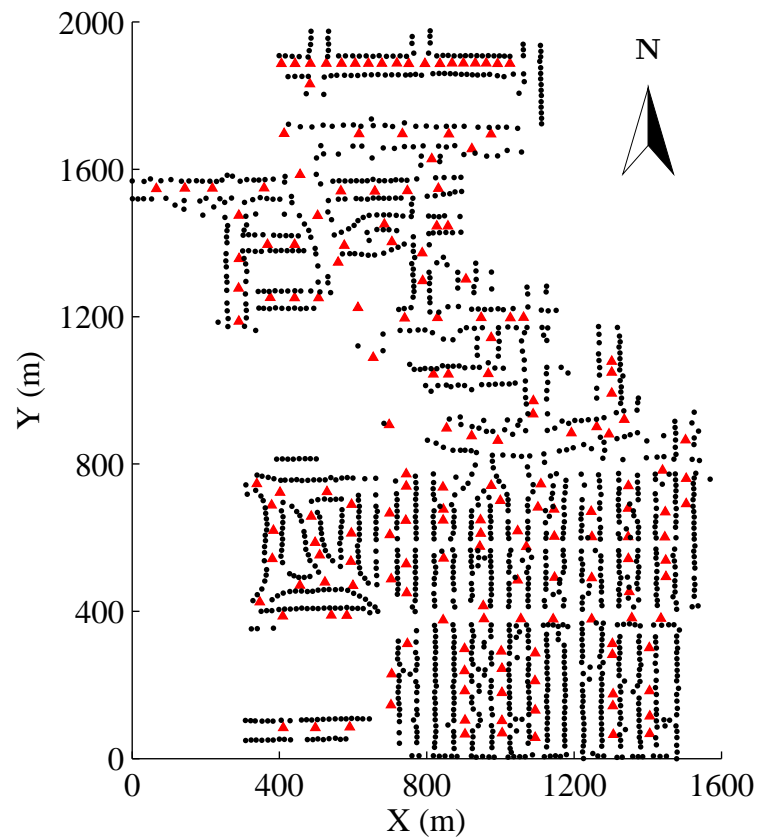


Figure 3.3: Location of distribution transformers (red triangle) and houses (black dots) in the distribution feeder.

Figure 3.4.

The load in the feeder comes from the HVAC (Heating, Ventilation and Air Conditioning) and other appliances in residential and commercial buildings. GridLAB-D is used to model and simulate the electricity usage of each building, whose parameters are provided by [56]. The ETP (Equivalent Thermal Parameter) model developed by PNNL is utilized by GridLAB-D to simulate the thermal balance of each building and thus generate the HVAC load. The electricity usage profile of other appliances are also provided by PNNL based on an end-use load survey.

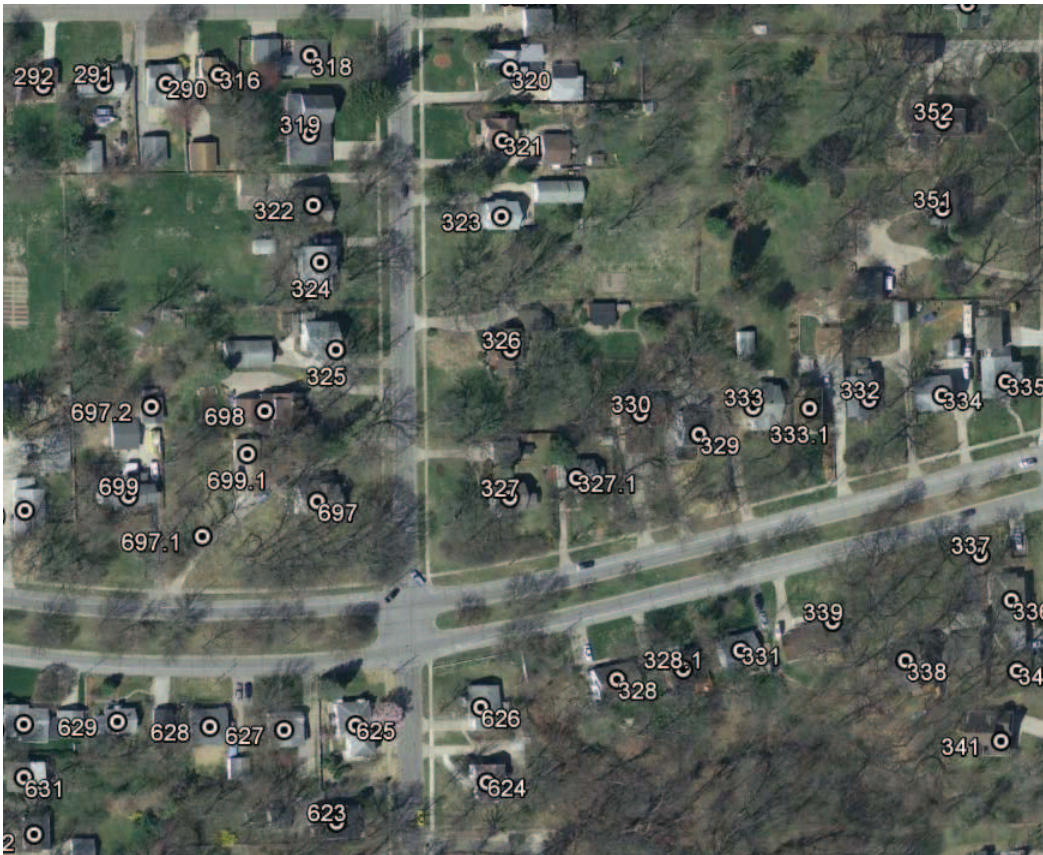


Figure 3.4: Measuring the location of each house in GoogleEarth

3.3.2 PV System

In this study, all PV systems are modeled as rooftop PV and it is assumed that every house has the PV system installed but with different parameters. Each house has 8 parameters for modeling the PV generation.

The first parameter is the geographic location of each house in terms of longitude and latitude. GoogleEarth is used for identifying the position of each house, as shown in Figure 3.4. The longitude and latitude for houses and distribution transformers are then converted to meters on a $x - y$ plane. The minimum value of x and y among all coordinates is selected as the origin for the new coordinate system, as shown in Figure 3.3.

The second parameter is the facing of the roof area for PV installation. It is assumed that the PV facing direction is either due south or due west, for the reason that facing south can maximize the PV generation and facing west can make the PV generation peak better align

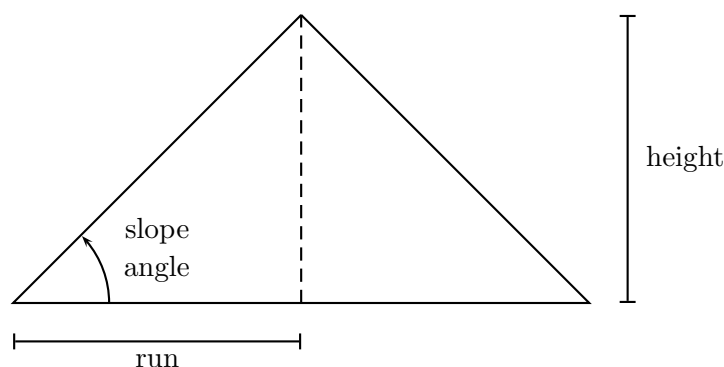


Figure 3.5: Roof pitch and slope angle.

with the evening load peak. The ratio between south facing and west facing PV systems is 3:1.

The third parameter is the roof pitch or the angle of the roof. The roof pitch is defined as the ratio between the vertical height and the horizontal run of the roof, which is also the tangent value of the slope angle, as shown in Figure 3.5. Typically, the run is expressed as the number of 12, and the height ranges from 0 to 12 with increment of 1. Here, height above 12 is not considered, since the very steep roof for residential house is not very commonly seen. A similar choice is also made in [60]. The roof pitch shown in the figure is 12:12, which corresponds to 45° .

The fourth parameter is the available roof area for installing the PV system. The south or west facing part of the roof are measured using GoogleEarth, as shown in Figure 3.6. Note that the area measured from the satellite picture in GoogleEarth is the horizontal projection of the roof, which means that it needs to be converted back to the actual roof area by dividing the cosine value of the roof slope angle. The PVWatts Calculator [61] from National Renewable Energy Laboratory (NREL) adopts a similar approach.

The fifth and sixth parameter are the tilt angle and the azimuth angle of the PV system. Since it is common to install the PV panels along the roof surface, the tilt angle and azimuth angle will be the same as the roof slope angle and the facing. The only exception is for the house with a flat roof. i.e., roof slope angle of zero degree. For this case, the common practice is to have the PV system face due south and have a tilt angle equal to the latitude of the location.



Figure 3.6: Measuring the available roof area for PV system.

The seventh parameter is the module efficiency of the PV system on each house. The technical data of 65 modules, covering the most popular brands in the market [62] as shown in Figure 3.7, are compiled to provide a ground for modeling the module efficiency. Though First Solar has the 2nd rank, its PV modules are not considered due to the fact that its thin film PV product is mainly for utility-scale commercial and industrial applications, instead of residential installations. The full list of data can be found in Appendix A. Based on the data, the probability distribution function (PDF) of the module efficiency is estimated, as shown in Figure 3.8. As can be observed, the estimated distribution is close to a Gaussian distribution with mean value of 15%. This average module efficiency is considered reasonable, given the value of 13.5% used by [58] back to 2007. The efficiency of PV system for each house is then randomly sampled from this estimated PDF.

The eighth parameter is the maximum possible nameplate capacity of the PV system installed on the rooftop of each house. It is assumed that all available south facing or west

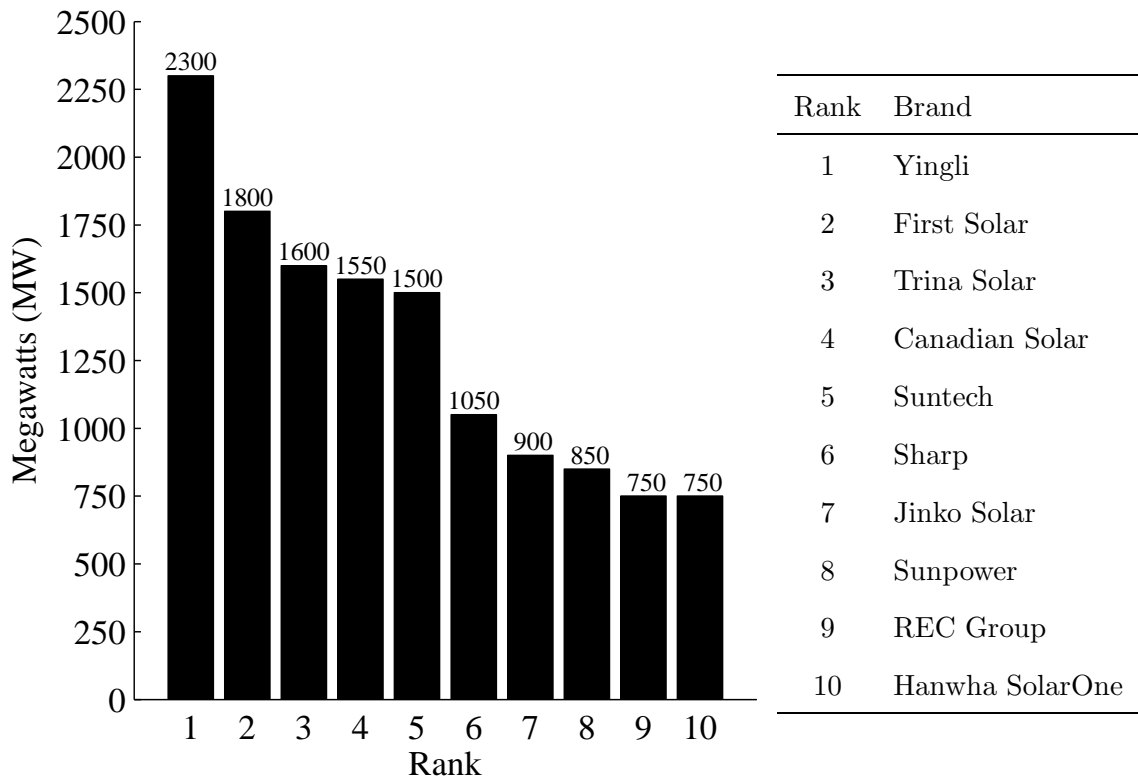


Figure 3.7: The module shipments in MW of top 10 PV supplier in 2012 worldwide.

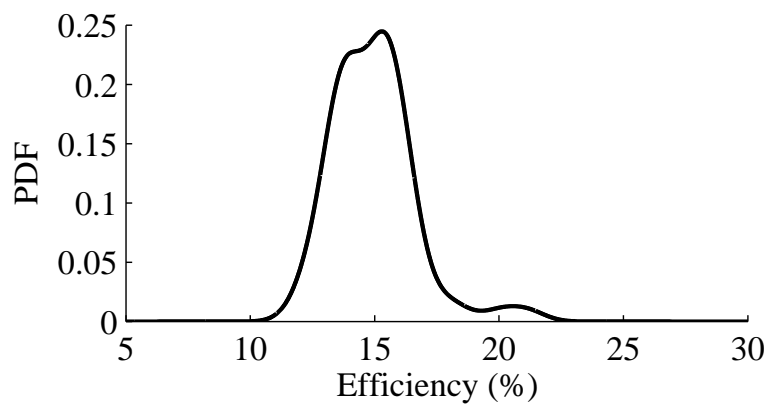


Figure 3.8: Estimated probability density function of PV module efficiency.

facing roof area is mounted with PV panels. Given the available roof area R in m^2 and the PV module efficiency of η , the nameplate capacity (W) of the PV system taking all available roof area can be calculated as $R \times \eta \times 1000 \text{ W/m}^2$.

3.3.3 Simulation Parameters

In this study, simulation parameters configure the simulation process and are divided into four groups. The first group is for defining the simulation timestamp, i.e., simulation start/end time (T_s/T_e) and simulation step. Unless otherwise specified, in this study all simulations run with 1-sec time step in order to capture all possible events (sub-second events are not considered here). The second group is for generating the cloud shadow pattern using the fractal-based model as discussed in Section 2.6. The default values are $s = 7$, $N = 512$, $K = 21$, $D1 = 1.9$, $D2 = 1.33$ and $\alpha = 400$.

The third group is for configuring the measurement grid for synthesizing the irradiance time series from the cloud shadow pattern. Given the coordinates of all houses in the distribution feeder, the ideal irradiance measurement method is to place an irradiance sensor on top of each house and sample the irradiance shading sequence from the cloud shadow pattern for its own. In order to speed up the simulation, a less dense measurement grid is used, which is to place the irradiance sensor at the location of each distribution transformer and then share the sampled shading sequence with houses in the vicinity of the distribution transformer. Figure 3.9 shows the two measurement method, where the left one is to use the location of all houses and the right one is to use the location of all distribution transformers. To check how much error will be made by using the transformer measurement grid, a 10-minute simulation with 1-sec step is performed with the same cloud shadow pattern and all other parameters. Figure 3.10 compares the total real power at the substation using different measurement method to model the total PV power. As can be observed, the error is very small, and it is thus acceptable to use the less condense measurement grid to synthesize the power output time series for all PV systems. Unless otherwise specified, the transformer measurement grid is used for all simulations.

The fourth group is for configuring the LTC device, including:

- Voltage center (V_0): the desired voltage point for tap 0 position. The default value in this study is 7915 V.
- Number of raise and lower taps: the default value is 16 for each direction.
- Voltage regulation range (R_r): the default value is $\pm 10\%$ of V_0 .
- Voltage tap change (V_{tap}): the voltage change per tap position. As discussed previously, this value is derived from V_0 and the voltage regulation range. With default setting, this value is 51 V.
- Voltage bandwidth (V_b): the tolerance of voltage variation for each tap position. The default value is 60 V, which means the LTC will be alarmed when the voltage is out of ± 30 V of the desired voltage point at this tap.
- Wait time (T_w): after the LTC gets alarmed of the voltage violation, it will change the tap position only if the voltage keeps out of the range for a consecutive T_w seconds.
- Voltage sensing mode: specify the source of voltage monitored by the LTC, which can be the LTC output terminal voltage (local sensing mode) or the voltage at any node in the distribution network (remote sensing mode). The default setting is to use the local sensing mode.

3.3.4 Scenario Parameters

The scenario parameters define different scenarios, in which the LTC operation is studied. There are four scenario parameters, i.e., cloud velocity, cloud cover, cloud movement direction and PV penetration. As discussed in Section 2.6, the cloud velocity affects how much cloud pattern will be generated and the cloud cover determines how much sky will be filled by clouds. The coordinates of measurement points should be rotated properly based on the the cloud movement direction.

PV penetration will decide the nameplate installed PV capacity in the simulation. The concept of hosting capacity (HC) is used for mathematically defining the PV penetration in

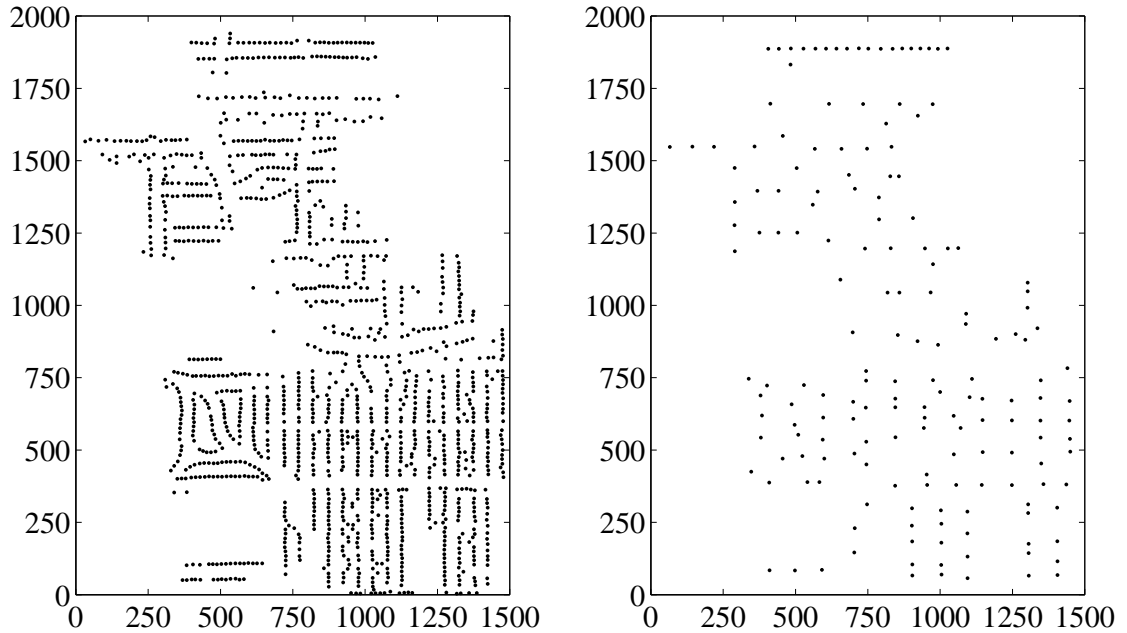


Figure 3.9: Two measurement grids for generating the irradiance time series for each PV system. Left: using 1372 houses. Right: using 175 distribution transformers.

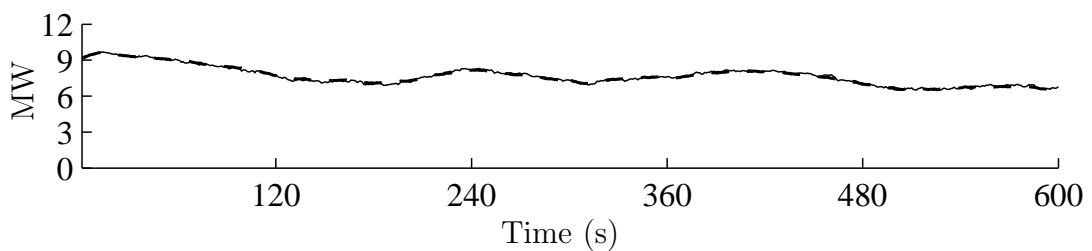


Figure 3.10: Comparing the substation total real power using different measurement grid. Dashed line: using 1372 houses. Solid line: using 175 distribution transformers.

this study. As proposed by [63,64], hosting capacity is a method for quantifying the amount of distributed generation allowed to be installed within a distribution system without violating the system operational constraints, e.g., voltage magnitude, power factor, loading of transformers and lines, losses, etc. In this study, the concept from [65] is borrowed, where the hosting capacity approach was studied and developed in details.

Hosting capacity, with respect to a certain metric such as the maximum transformer loading or the maximum drop of voltage magnitude at the end of the feeder, is defined as the maximum amount of distributed generation, here PV, can be deployed in a certain distribution system, beyond which the distribution system performance, measured by the metric, becomes unacceptable. Occasionally, it can be observed that, with the initial introduction of a small amount of distributed PV generation, some system performance metrics are first improved, and start to drop with an increased amount of installation. Hence, two hosting capacities are further defined. The first hosting capacity (HC1) is the installed capacity of distributed PV, beyond which the system performance is worse than the original system without any PV. The second hosting capacity (HC2) is the installed capacity, above which the system starts to experience unacceptable conditions.

This concept is illustrated by Fig. 3.11. In the the original system, represented by the point A, the maximum observed loading level of the transformer is 60% of its rating capacity. With the introduction of PV systems connected to it, the peak loading level first reduces but rises back to the 60% condition again, which is caused by the large amount of reverse power flow injected by PV systems during light demand hours. The first hosting capacity is therefore obtained, since with more PV the maximum loading of the transformer will exceed 60% which is the original level. With further increase of installed PV capacity, the maximum loading condition of the transformer keeps going up, until the point C, where the second hosting capacity is reached. Beyond this second hosting capacity, the transformer will experience overloading conditions, e.g., more than 100% of its rating capacity, and this is conservatively considered as unacceptable.

In this study, the second hosting capacity is used to determine the maximum allowance

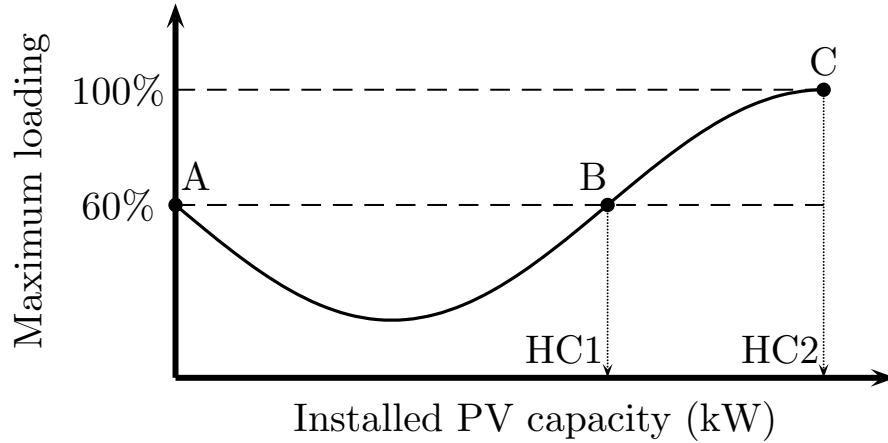


Figure 3.11: Illustration of 1st and 2nd hosting capacity (HC), where the x -axis is the installed capacity of PV systems under a distribution transformer and the y -axis is the maximum loading experienced by the transformer.

of PV capacity under each distribution transformer. Next, the method to calculate the (second) hosting capacity is discussed, with a reference to [65]. First, the simple case with only consideration of real power is explained and then the full case with considering both real and reactive power is outlined.

For the real power only case, let the real power seen by the transformer at time t , $P(t)$, be given by (3.1), where $P_L(t)$ is the total real power consumption under the transformer, and $P_G(t)$ is the total real power injection of PV systems under the transformer. Thus, $P(t)$ is positive when load is greater than PV injection, and negative for the reverse power flow.

$$P(t) = P_L(t) - P_G(t) \quad (3.1)$$

Let $P_{r,t}$ denote the real power rating of the transformer for both direction of power flow, then it is required that $-P_{r,t} \leq P_L(t) - P_G(t) \leq P_{r,t}$, with a conservation assumption that the transformer should not be overloaded at any time. From this constraint, we can obtain $P_G(t) \leq P_L(t) + P_{r,t}$. Thus, the hosting capacity of PV under the transformer $P_{G,HC}$ will be $P_{L,\min} + P_{r,t}$. For example, $P_L(t) \in [1, 5]$ kW and $P_{r,t} = 10$ kW, then there should be no more than 11 kW of PV injection to ensure the transformer will not be overloaded at any time.

When considering both the real and reactive power, let the magnitude of apparent power flowing through the transformer at time t be given by (3.2), with the assumption of unity

power factor of PV systems.

$$|S(t)| = \sqrt{[P_L(t) - P_G(t)]^2 + Q_L(t)^2} \quad (3.2)$$

The maximum reverse power flow happens with the maximum PV generation and minimum load consumption. Let $|S_{r,t}|$ denote the magnitude of the rated apparent power of the transformer. In order to ensure the transformer is not overloaded by the maximum reverse power flow, we need (3.3).

$$\sqrt{[P_{L,\min} - P_{G,HC}]^2 + Q_{L,\min}^2} \leq |S_{r,t}| \quad (3.3)$$

From (3.3), the hosting capacity of PV is obtained by (3.4), which is identical to equation 4.11 in Bollen's book.

$$P_{G,HC} = P_{L,\min} + \sqrt{S_{r,t}^2 - Q_{L,\min}^2} \quad (3.4)$$

For example, let's assume a transformer has a rating of 100 kVA. The peak load is observed as 80 kVA with a power factor of 0.9 lagging, i.e. 72 kW and 34.87 kVAr. The minimum load is observed as 20 kVA also with the 0.9 lagging power factor, i.e., 18 kW and 8.72 kVAr. Then the hosting capacity of PV can be calculated as

$$P_{G,HC} = 18 + \sqrt{100^2 - 8.72^2} = 117.62 \text{ kW}$$

Given the rating of the transformer and the information of minimum real and reactive power consumption of the aggregated load connected, the maximum amount of PV systems allowed to install can be calculated. The rating data is widely available for transformers, however the minimum load information for each transformer might not be readily available given the fact that traditionally utilities are more concerned about the maximum loading condition when sizing their transformers. So here the same assumption in [66] is made that the minimum load is 25% of the maximum load which is assumed to be the rating of the transformer. Here, it is also assumed a 0.95 lagging power factor for the minimum load condition, as suggested by [67].

For the distribution system used in this LTC study, the total rating of all distribution transformers is 8.15 MVA and the total hosting capacity calculated is 10.06 MW, as expected higher than the total rating of all transformers. With the PV hosting capacity calculated for each distribution transformer, the maximum possible PV capacity for each house needs to be adjusted. First, sum up the total maximum PV capacity of houses under a distribution transformer. Second, if this total capacity is greater than the PV hosting capacity of the distribution transformer, then a proper scale down coefficient is applied to the maximum possible PV capacity of each house such that the adjusted total value equal to the PV hosting capacity. If this total capacity is smaller than the PV hosting capacity of the distribution transformer, then no further adjustment is needed since there won't be any more available roof area for additional PV panels. After doing this adjustment for all PV systems, the total installed PV capacity is at last defined as the 100% penetration case. For less penetration cases, one just needs to further scale down the PV system size of each house from the 100% penetration case.

3.3.5 Summary on Simulation Setup

To setup the simulation using the fractal-based cloud shadow and irradiance model, there are four key steps as listed below.

1. Prepare the parameters and inputs for generating the cloud shadow pattern.
2. Specify the measurement grid which synthesizes the irradiance time series for each PV system.
3. Model each PV system, including its nameplate capacity and orientation.
4. Determine the load profile at each distribution transformer.

Two things are worthy noting. First, in all following simulations, all scenario parameters are explicitly defined. Simulation parameters not listed will use the default values specified in Section 3.3.3. Second, due to the stochastic natural of PV generation, simulation will run for

several realizations with same simulation parameters under a certain scenario defined by the scenario parameters.

3.4 Impact on LTC Operation in Different Season

It is a common practice for distribution system operators and planners to look at the system performance in different seasons. The load shape and magnitude exhibit a large difference between summer and winter. Figure 3.12 shows the real power measured at the substation and the temperature for the first week of January and July in 2011. By comparing Figure 3.12(a) and Figure 3.12(b), two observations can be made. First, the daily load follows a similar pattern in the same season, without too much difference between days. Second, the daily load in summer has its peak hour in the afternoon, largely due to the heavy use of air conditioners, while the daily load in winter has two peak hours, one in the morning and the other one in the afternoon. The temperature plotted in Figure 3.12(c) and Figure 3.12(d) further shows that the summer load is highly correlated with the temperature, while the temperature does not have phenomenal impact on the winter electric load.

To study how the high penetration of PV generation could affect the LTC operation in different seasons, one day in summer (July) and one day in winter (January) are selected for simulation. First, GridLAB-D is used to generate the load profile, as shown in Figure 3.13. It can be observed that, although having two peak load during the day, the winter load has a smaller variation magnitude, ranging from 1 MW to 4 MW. However, for the summer load, it reaches the bottom at 1.5 MW and soars to the peak at 11 MW, which results in a 9.5 MW of difference.

The simulation setup is shown in Table 3.1. The simulation parameters and scenario parameters are same for both the summer and winter scenario and a detailed description of these can be found in Section 3.3. Since this experiment is with the purpose of comparing the effect of high penetration of PV on the LTC operation in different seasons, instead of investigating the LTC operation under a particular weather condition, it is thus assumed that for the whole day, the cloud cover is 50% and the cloud velocity is 5 m/s passing the study

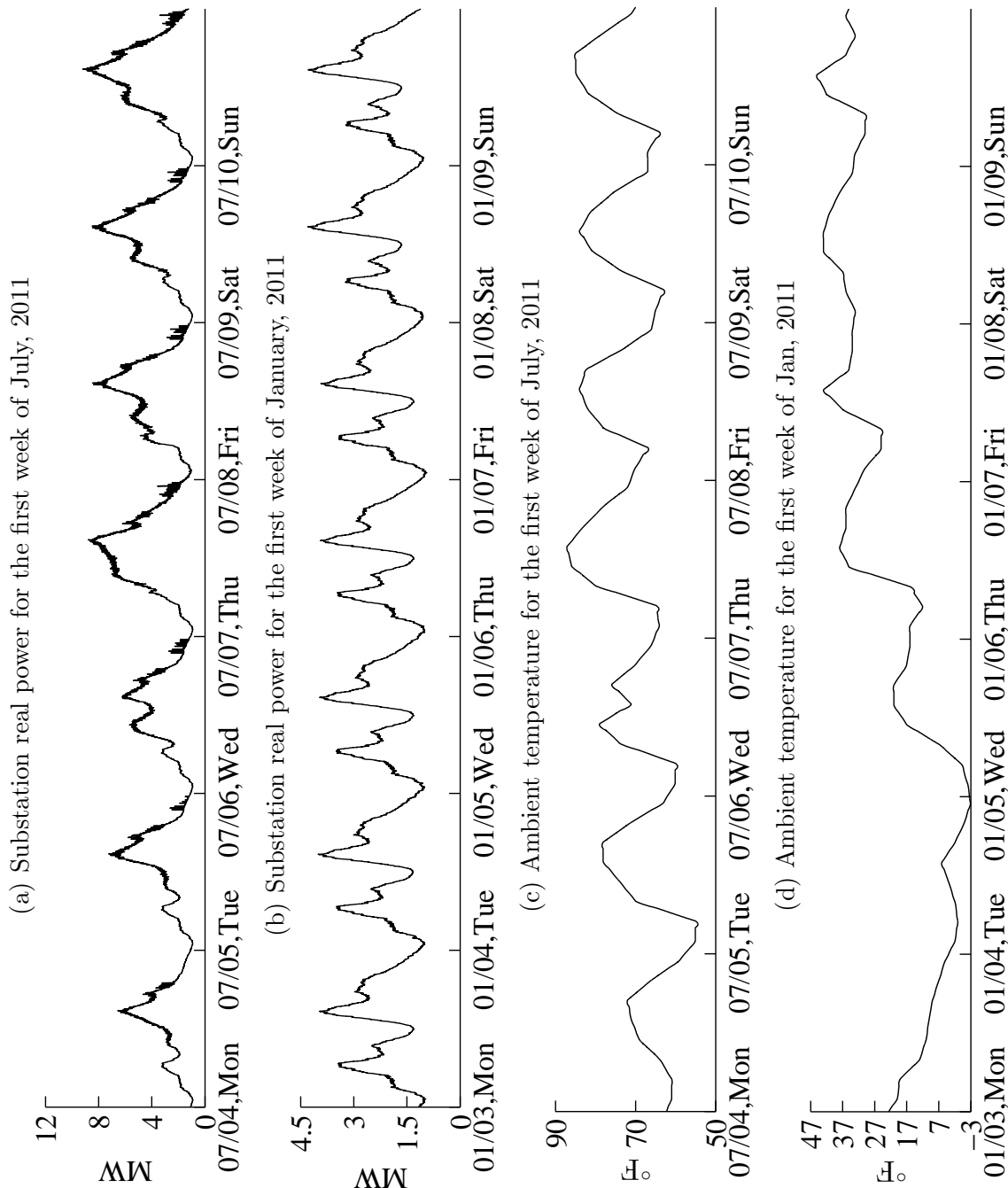


Figure 3.12: Load and temperature for the first week of January and July in 2011.

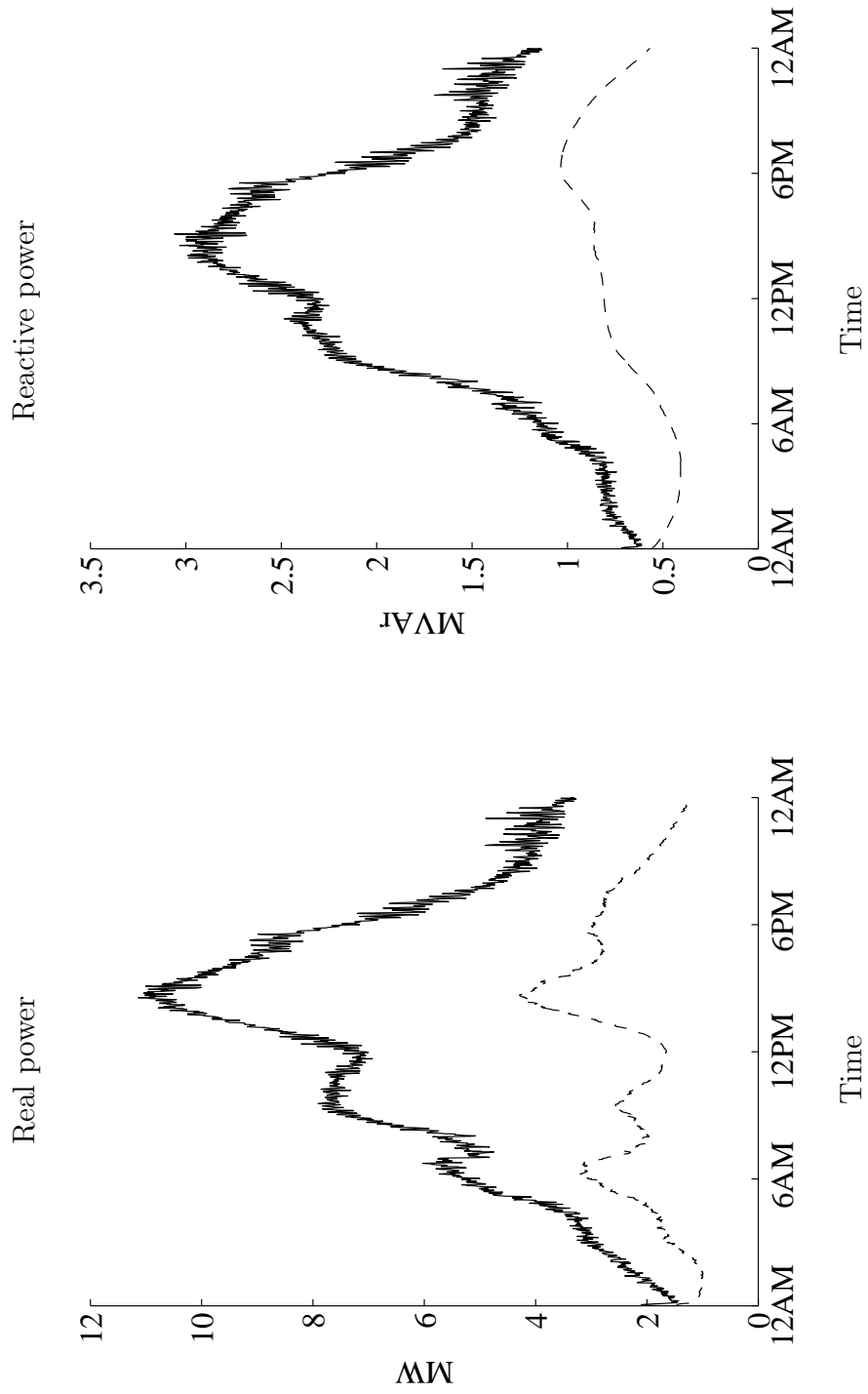


Figure 3.13: The real and reactive power load at the substation for a summer (solid) and winter day (dashed).

Table 3.1: Simulation setup for studying LTC operation in summer and winter scenarios

Simulation parameters		Scenario parameters	
T_s	00:00	cloud cover	50%
T_e	24:00	cloud velocity	5 m/s
iteration	5	cloud movement direction	0°
		PV penetration	100%

area from east to west. Note that, the fractal based cloud shadow model is capable to simulate different weather condition, either fixed or time variant, given the input of cloud cover, cloud velocity and movement direction. Five cases are simulated for the summer and winter day respectively. Due to stochastic characteristics of the fractal cloud shadow model, though with the same weather condition inputs, each case will simulate the whole day with different cloud pattern which will in turn result in a different PV generation time series.

Figure 3.14 shows how the PV generation reshapes the net load of the distribution system. Figure 3.14(c) is obtained by subtracting the PV generation shown in Figure 3.14(b) from the total real load shown in Figure 3.14(a). The red horizontal line in Figure 3.14(c) indicates the zero level on the vertical axis. It can be observed that during the noon hour, the feeder experiences the negative load, which means the distribution system is feeding power back to the transmission system. The PV generation and net system load in the winter scenario is shown in Figure 3.15, where it can be observed that due to the lower level of demand, the feeder has a severer negative load condition during an extended noon hours.

Figure 3.16 shows the measurements at the substation for the summer day without integrating any PV systems. Figure 3.17 shows one simulation realization of the distribution system performance in the summer day with 100% PV penetration. Compared to the voltage profile in the reference case without PV shown in Figure 3.16, the voltage profile in this realization becomes much more fluctuating due to the passing by clouds which cause the ramping up and down of a large amount of PV generation. The number of LTC tap changes increases dramatically, as seen in the phase tap position time series.

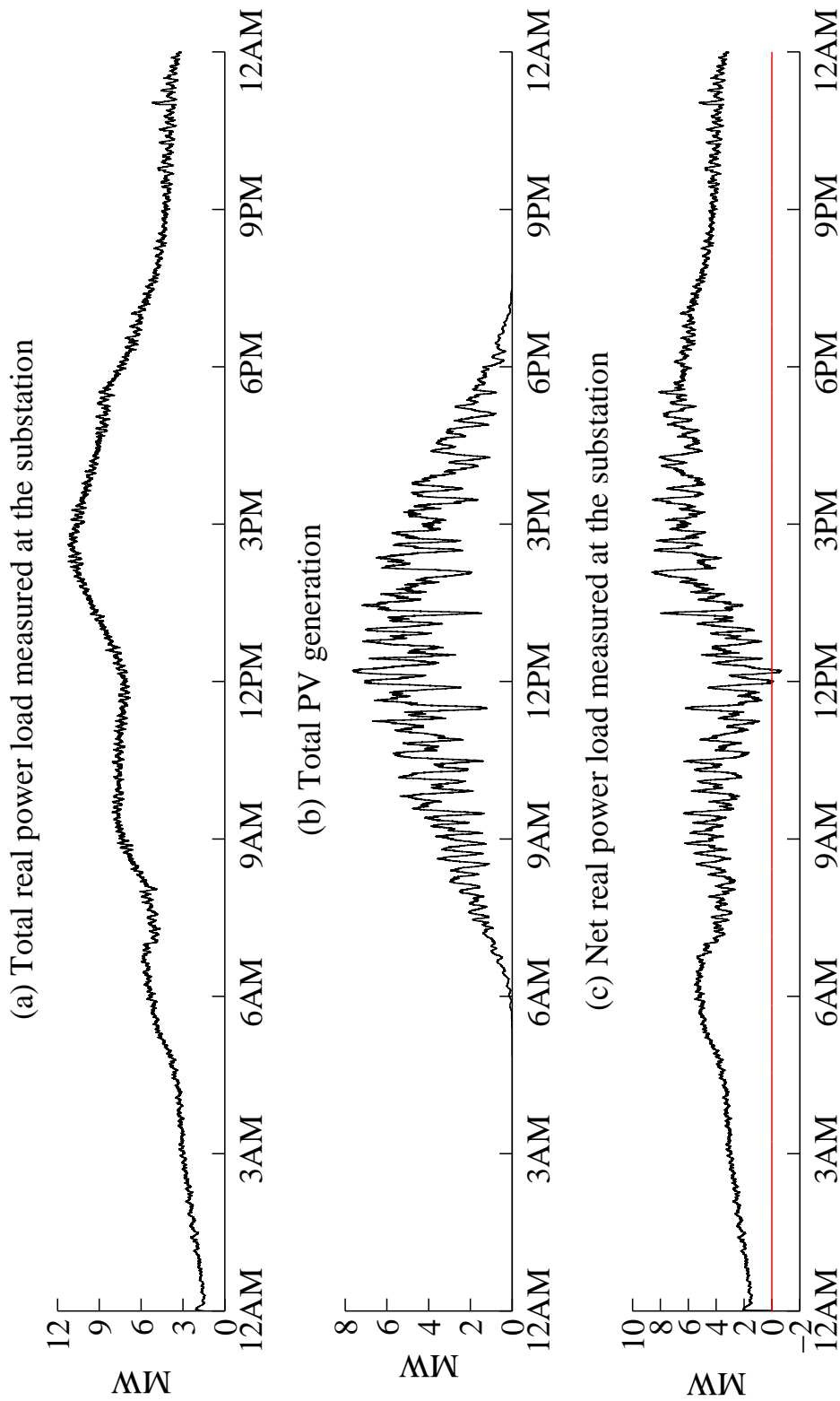


Figure 3.14: The reshaped net load profile in the summer day.

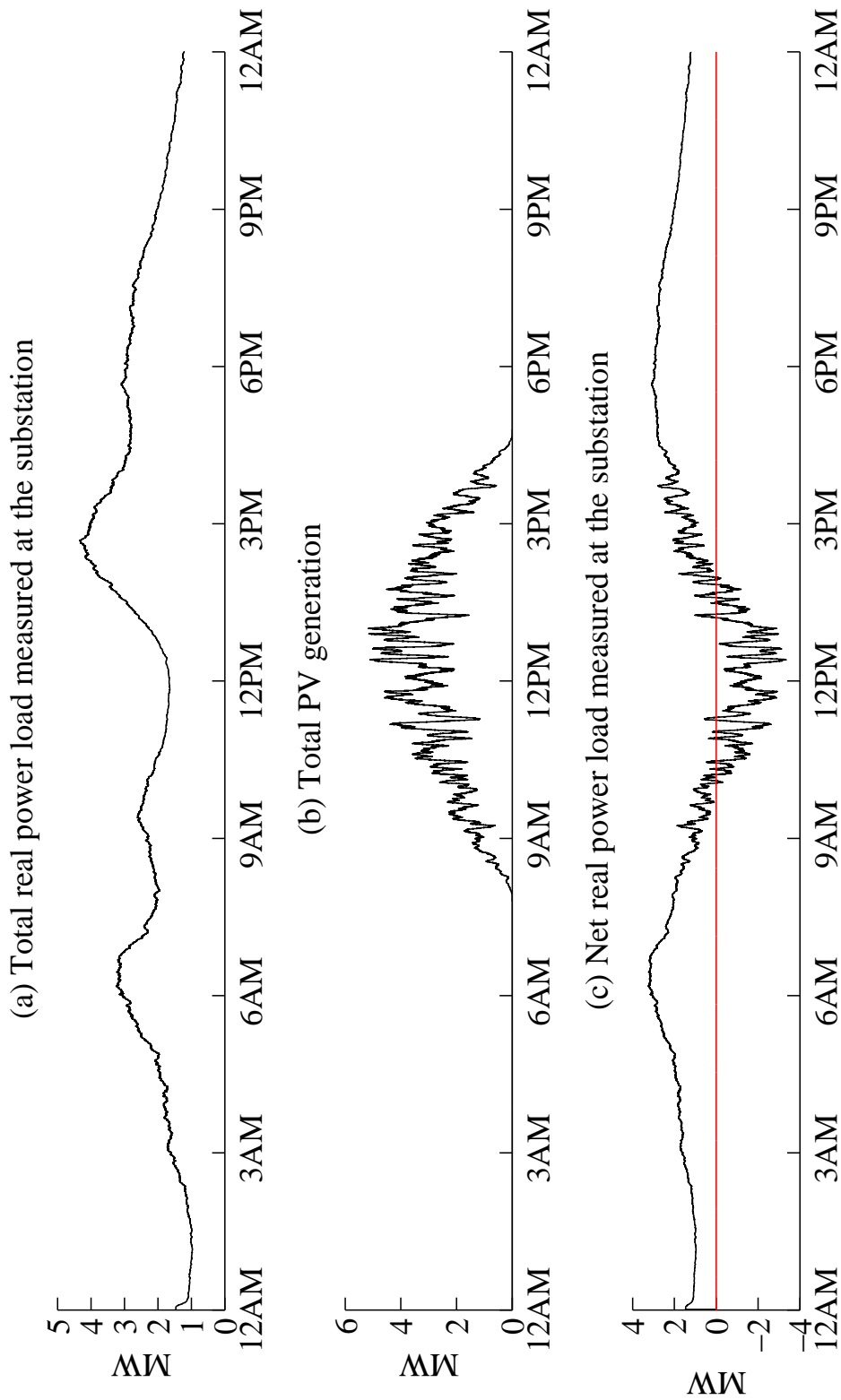


Figure 3.15: The reshaped net load profile in the winter day.

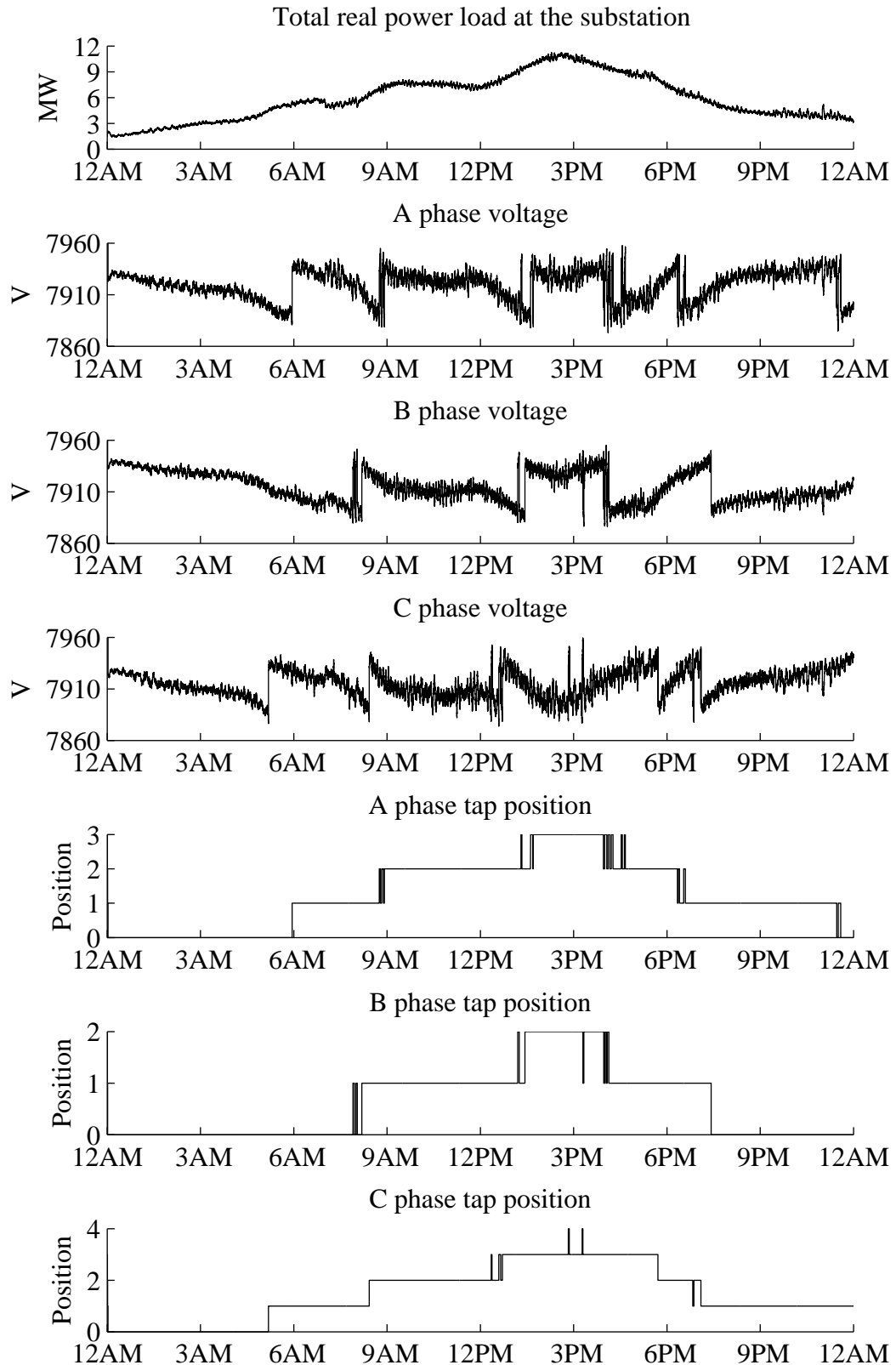


Figure 3.16: Measurements at the substation for the summer day without any PV integration.

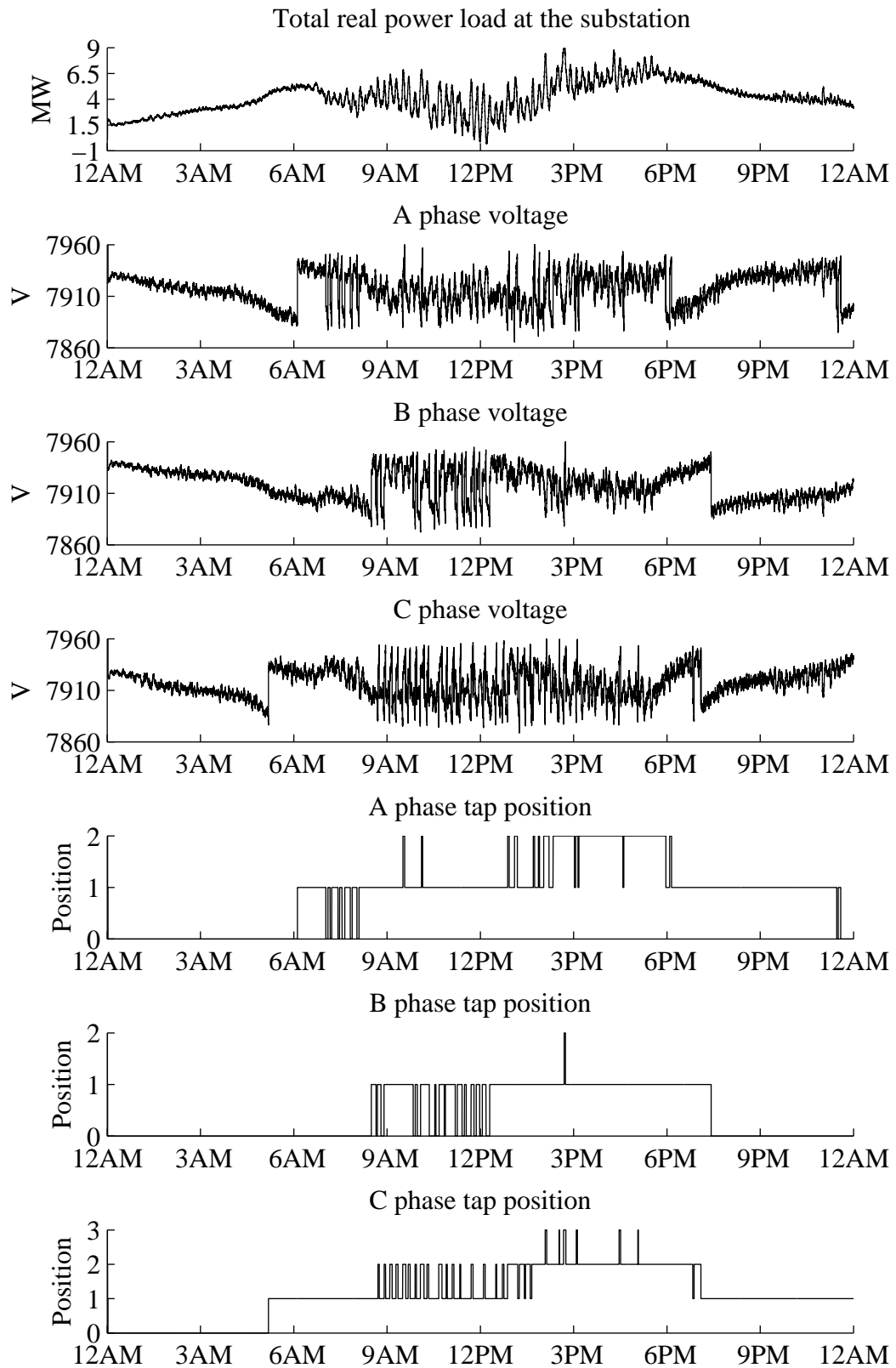


Figure 3.17: Measurements at the substation for the summer day with 100% PV penetration.

A magnified 15-min period of the phase B voltage in Figure 3.17 is further plotted in Figure 3.18 to show how the LTC operates with large fluctuations on PV generation. The time window between 11:20 AM and 11:35 AM is selected, for the reason that during this time period, the system load is relatively flat which can better reflect how the variation of PV generation affects the LTC operation. The solid line is the phase B voltage with the left axis and the dotted line is the phase B net real power with the right axis. Two horizontal dashed lines at 7945 V and 7885 V are the upper and lower limit for the ± 30 V voltage bandwidth of the voltage center at 7915 V. From $t = 210$, the net load on phase B starts to drop due to the increase of PV generation. Meanwhile, the voltage on phase B also gradually climbs toward the upper limit. At $t = 259$, the voltage exceeds the upper limit at 7945 V and alarms the LTC on the voltage violation. With $T_w = 30$ s, the LTC waits for 30 seconds and because the voltage is still out of the range, lowering one tap position change is triggered at $t = 289$ with voltage at 7948 V. The voltage immediately drops 51 V with the tap change to 7897 V at $t = 290$. From $t = 510$, the net load again rebounds with the decrease of PV generation. Accordingly, the voltage keeps decreasing and goes below the lower voltage limit at $t = 529$, which again alarms the LTC on the voltage violation. At $t = 559$, the voltage is still under the lower limit, one up tap change is made by the LTC after waiting for 30 s since the voltage violation alarm at $t = 529$, resulting a voltage jump of 51 V at $t = 560$.

Figure 3.19 shows the measurements at the substation for the winter day without integrating any PV systems. Due to a smaller magnitude of real power variation, the voltage profile on each phase is flat with very limited number of LTC operations (no tap change on A and C phase, 2 tap changes on B phase). However, with integrating a high penetration of PV, as shown in Figure 3.20, the net real power load becomes very fluctuating during the day hours. With this alternating net real power load, it is for sure that the voltage on each phase will experience much more fluctuations, as can be seen in Figure 3.20. As expected, the number of LTC tap changes increases considerably.

Figure 3.21 shows the three-phase total number of LTC tap changes for each realization under the summer and winter load scenario. The result are numerically summarized in Ta-

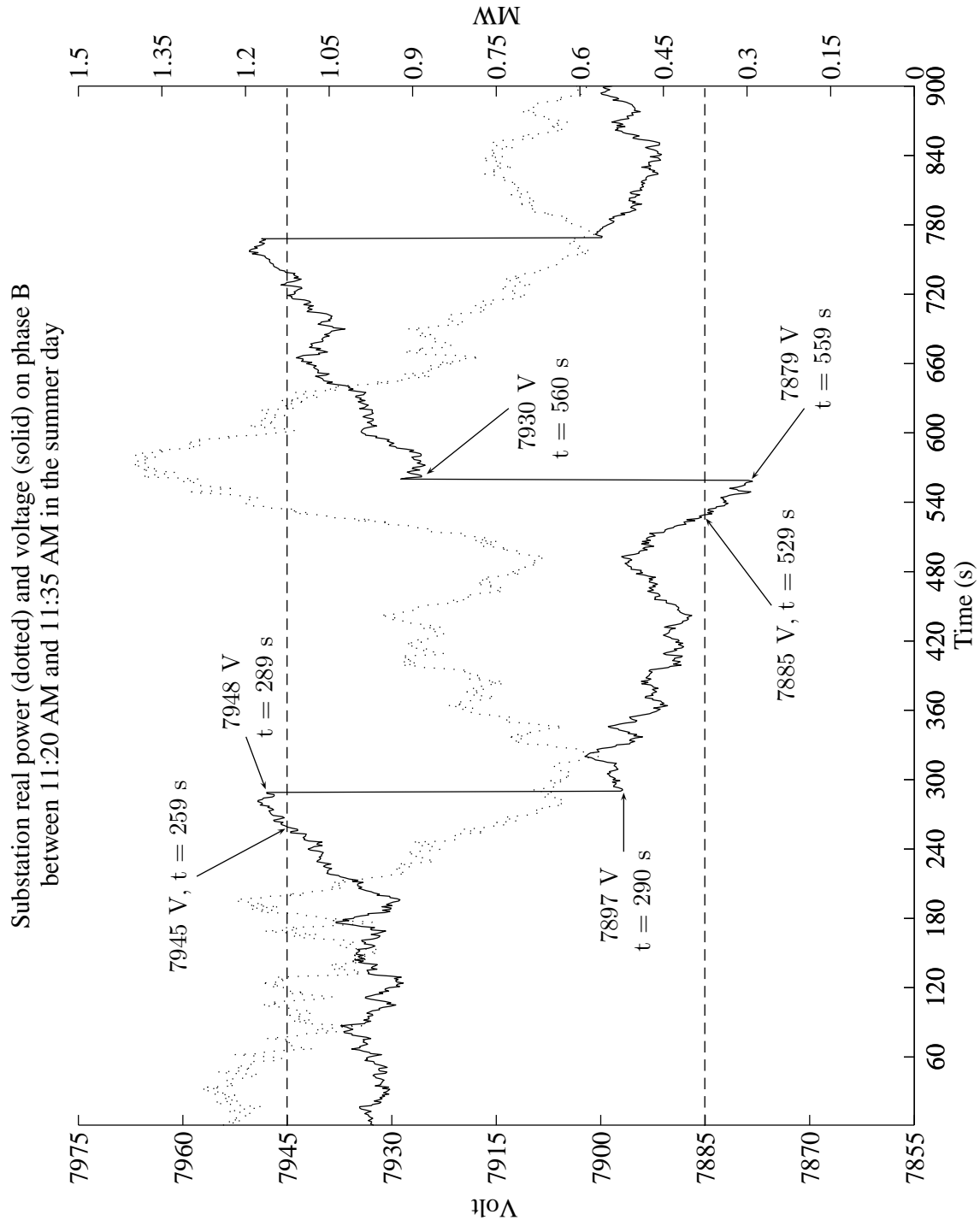


Figure 3.18: LTC operations within a zoomed 15-min period for the summer day with 100% PV penetration, 50% cloud cover and 5 m/s cloud velocity.

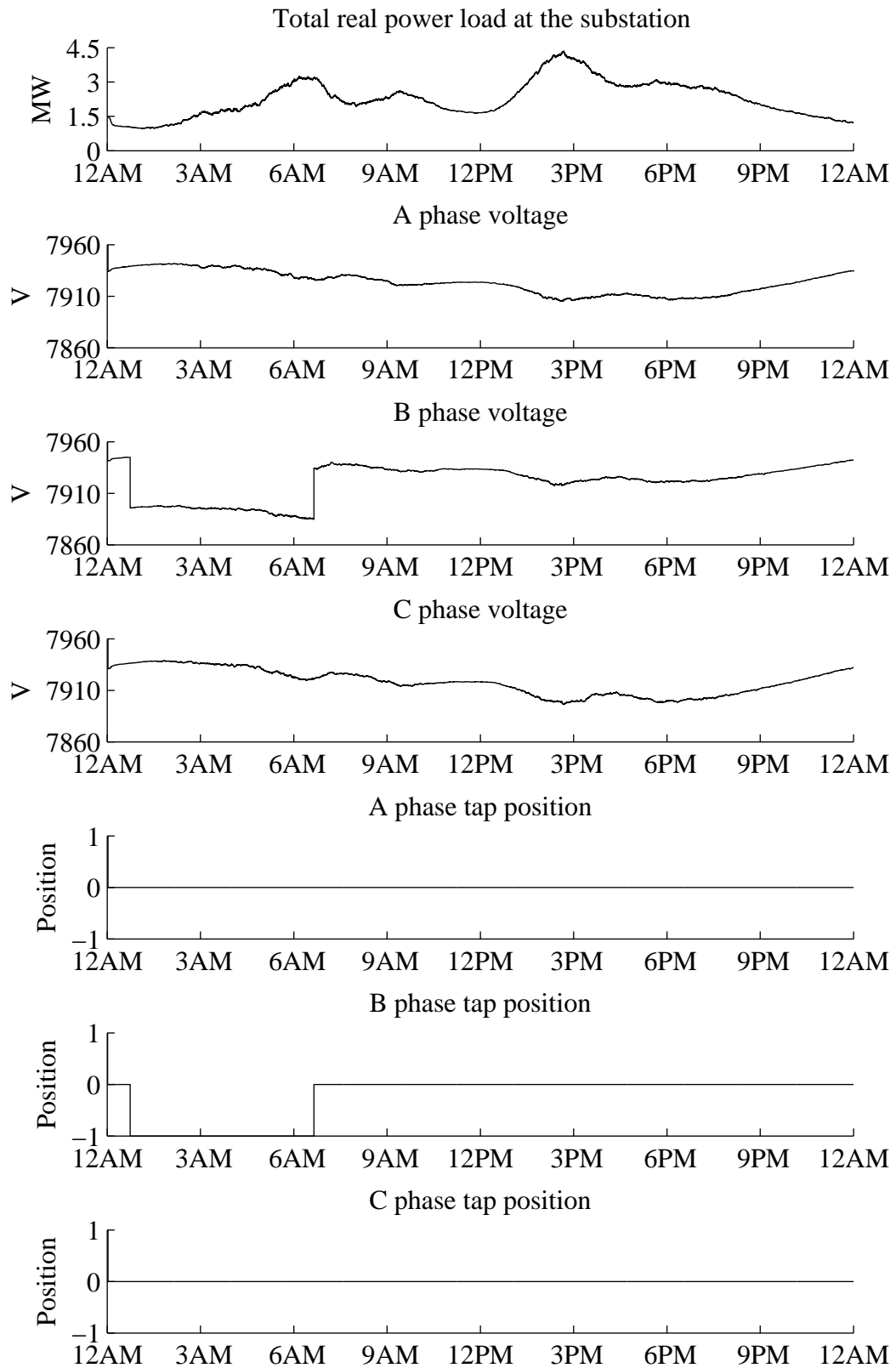


Figure 3.19: Measurements at the substation for the winter day without any PV integration.

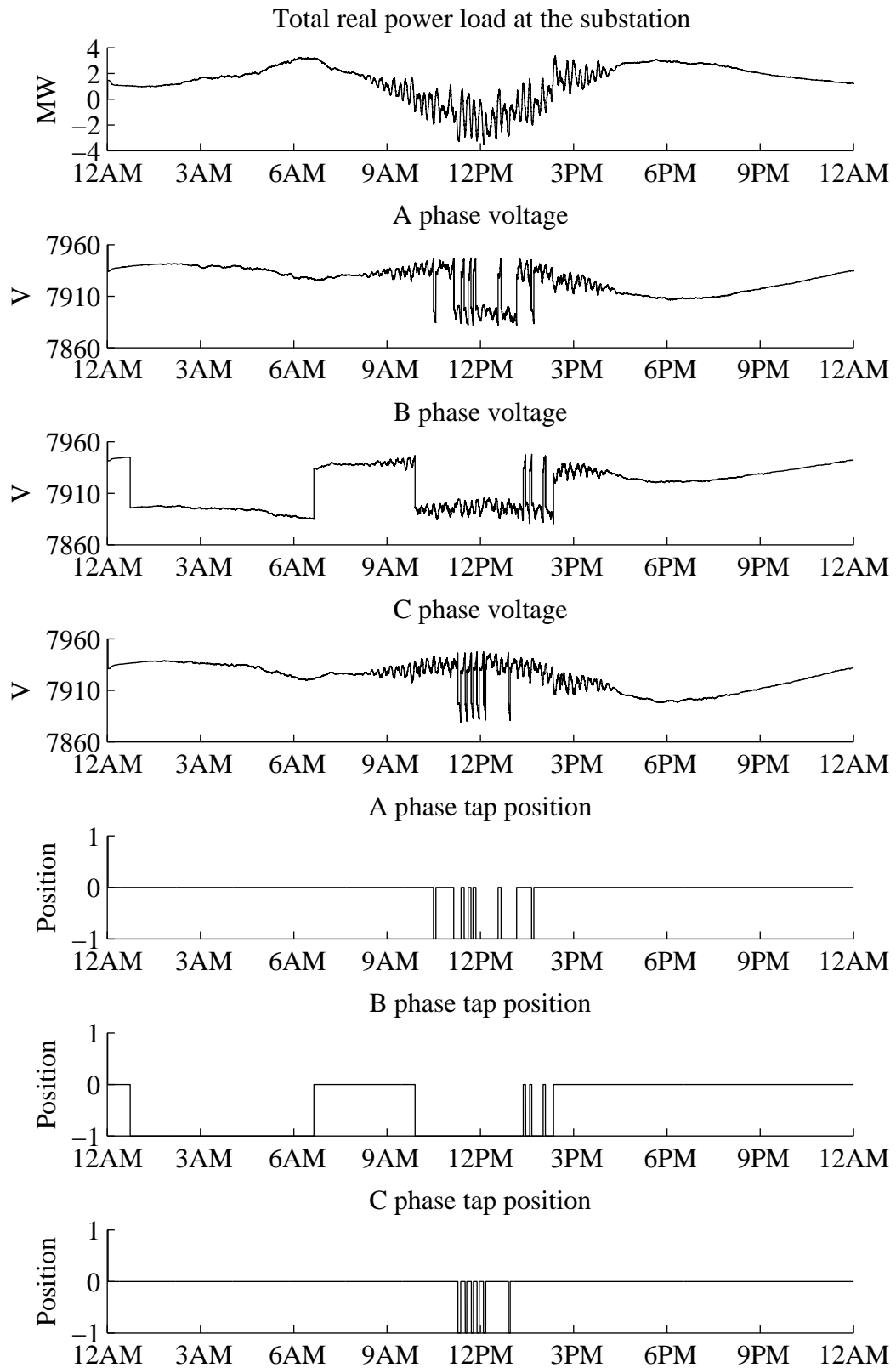


Figure 3.20: Measurements at the substation for the winter day with 100% PV penetration.

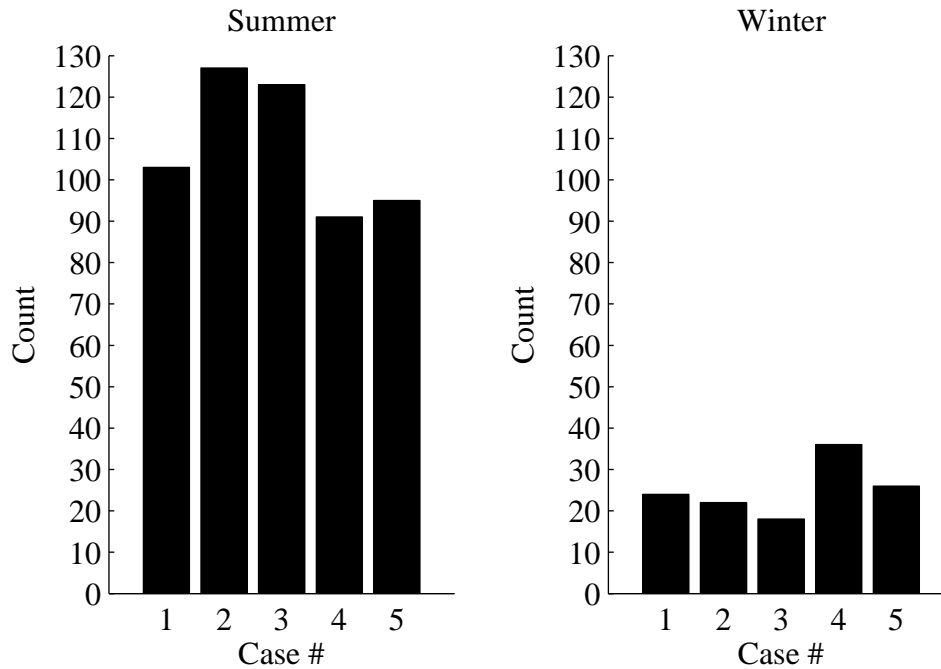


Figure 3.21: Three-phase total number of LTC tap changes for cases with 100% PV penetration.

ble 3.2. For the summer load scenario, the average number of LTC tap changes is 109, which is almost double the number in the summer reference case with no PV integrated. For the winter load scenario, the integration of high penetration of PV generation greatly changes how the LTC operates in a winter day. In the reference winter case without PV, there is only 2 tap changes on B phase. However, the average number of LTC tap changes for cases with PV is 25, 12 times of the winter reference case count. This dramatic difference might raise the attention of the distribution system operators on how to properly set the parameters of their LTC equipment and reschedule the maintenance on it.

3.5 Effect of Cloud Velocity and Cover

The weather condition, especially the cloud velocity and cloud cover, will have a major impact on the PV generation. Since the distributed PV generation will reshape the net load of the distribution system, the LTC operation will also be different under different cloud

Table 3.2: Simulation result of total number of LTC operation for the 24-hour period in summer and winter scenarios.

	Case 1	Case 2	Case 3	Case 4	Case 5	Average	No PV case
Summer	103	127	123	91	95	109	61
Winter	24	22	18	36	26	25	2

condition. However, due to the fact that there were no suitable cloud and irradiance model available, the issue of weather's impact on LTC operation hasn't received enough qualitative or quantitative studies. Now, with the proposed fractal-based cloud and irradiance model, this issue can be better studied in a simulation manner with the control of different cloud condition. The rest of this section first studies the impact of cloud velocity on the LTC operation and then investigates the effect of cloud cover on the LTC operation.

The one-hour window (11 AM to 12 PM) in the summer day scenario is chosen for the load profile, based on which the LTC operation is simulated with different cloud velocity and cover. The reason for this selection is because this time window has a relatively constant load profile, which provides a perfect environment to study how the fluctuation of PV generation will affect the LTC operation. Figure 3.22 shows the measurements at the substation for the reference case without PV. There are no LTC operation on each phase in this simulation hour due to the relatively flat load profile.

3.5.1 Impact of Cloud Velocity

The setup of the simulation is listed in Table 3.3. Five cloud velocity scenarios are selected and studied based on the data in [46]. One realization of PV generation for each cloud velocity scenario is shown in Figure 3.23. As can be observed, with increased cloud velocity, the total PV generation tends to have more frequent fluctuations. Ten simulations are performed for each cloud velocity scenario to investigate how this increasing of PV generation fluctuation will affect the LTC operation.

Figure 3.24 and Figure 3.25 individually plots the voltage profile and LTC operation on

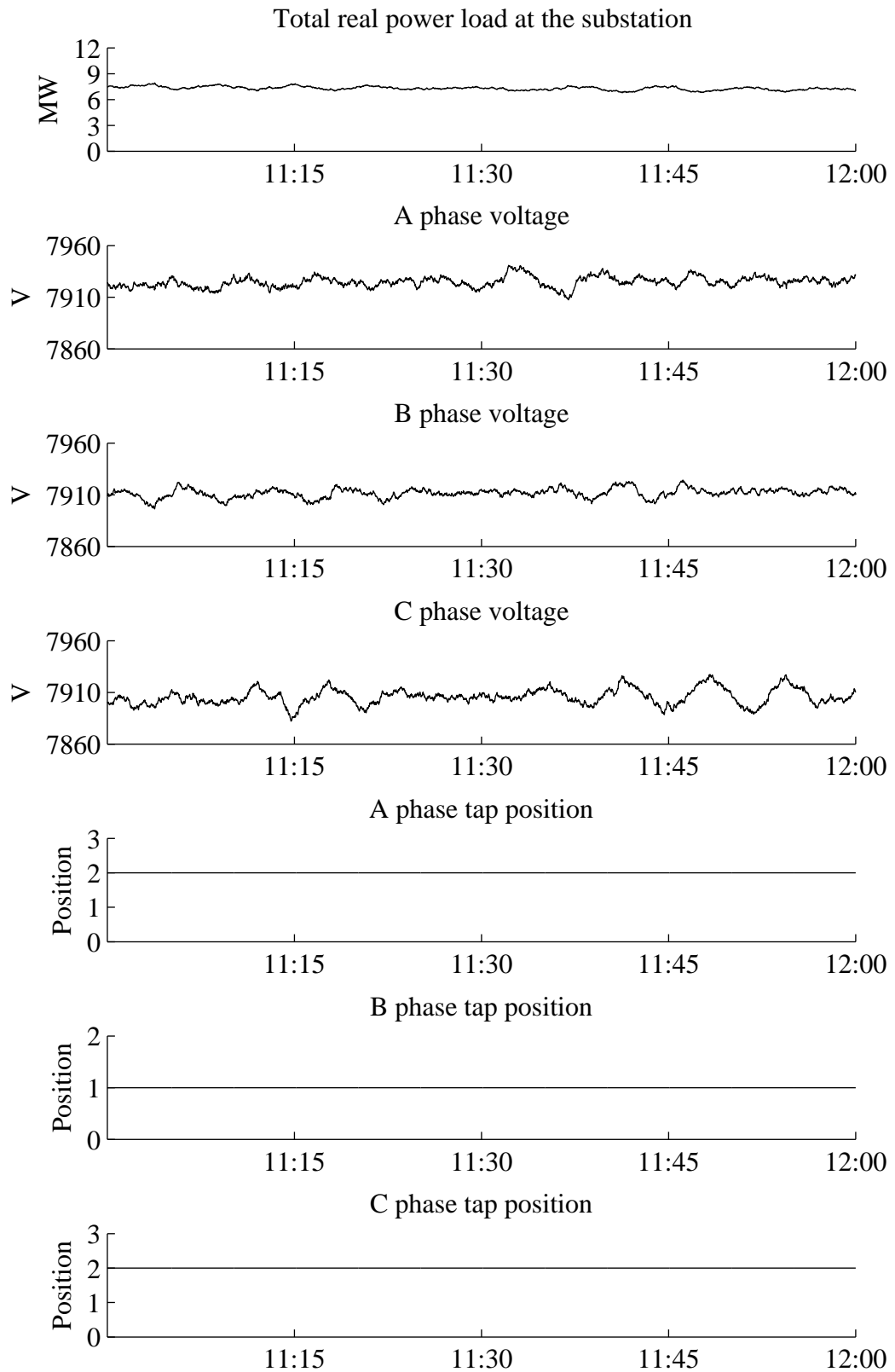


Figure 3.22: Measurements at the substation between 11 AM and 12 PM with summer load.

Table 3.3: Simulation setup for studying LTC operation under different cloud velocity

Simulation parameters		Scenario parameters	
T_s	11:00	cloud cover	50%
T_e	12:00	cloud velocity	3,6,9,12,15 m/s
iteration	10	cloud movement direction	0°
		PV penetration	100%

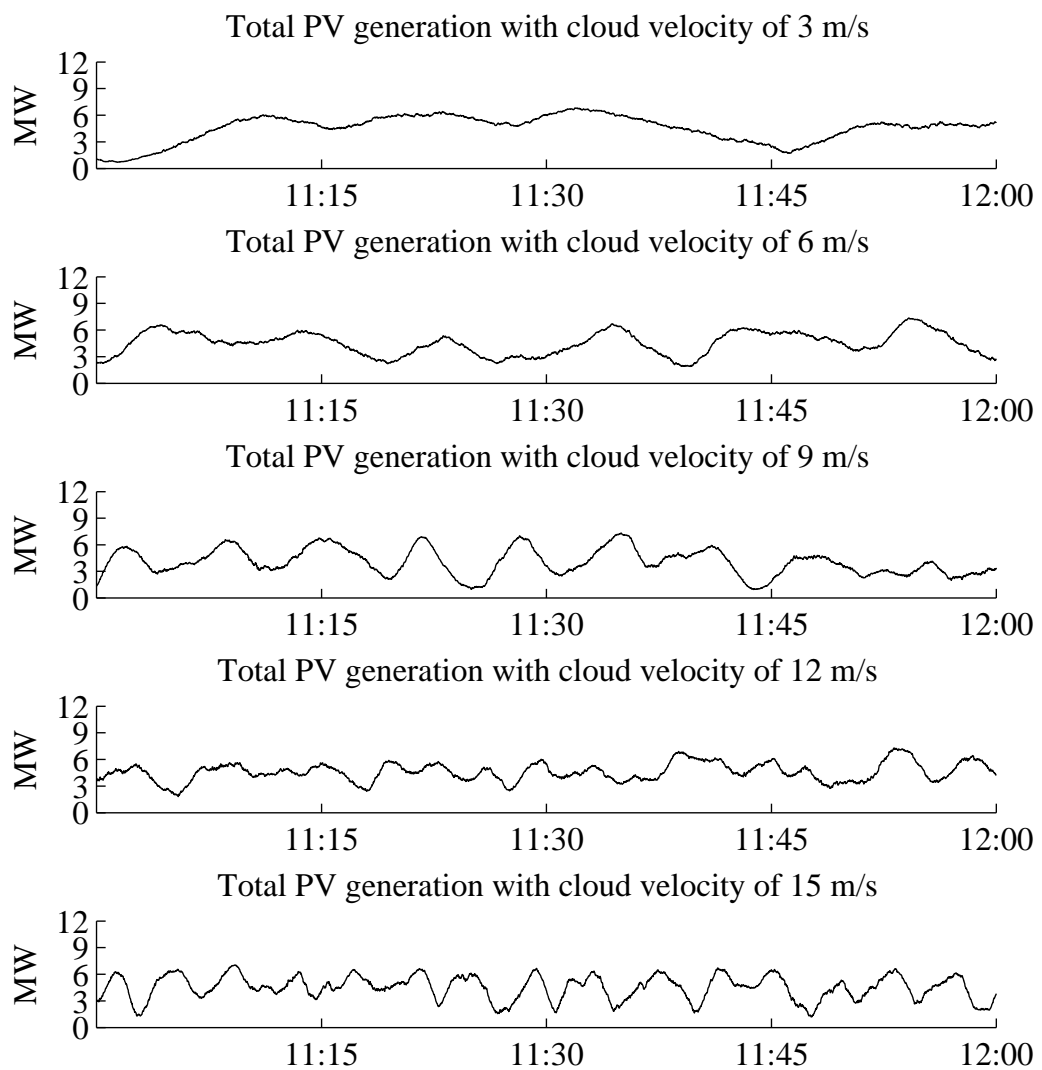


Figure 3.23: Total PV generation of one simulation case with different cloud velocity.

Table 3.4: Simulation result of total number of LTC operations in 1-hr period of the summer day with different cloud velocity scenarios

	3 m/s	6 m/s	9 m/s	12 m/s	15 m/s
Case 1	11	14	29	11	30
Case 2	8	13	14	14	15
Case 3	13	18	16	20	22
Case 4	11	28	22	39	12
Case 5	10	10	17	20	16
Case 6	9	17	12	21	23
Case 7	11	20	10	19	30
Case 8	15	11	11	16	20
Case 9	15	7	17	28	30
Case 10	17	10	11	11	22
Average	12	14.8	15.9	19.9	22

each phase for the lowest and highest cloud velocity scenario (3 m/s and 15 m/s). It can be seen that, even with little cloud movement, the LTC will operate whenever the feeder area is covered by the cloud shadow, and with fast cloud movement, the number of LTC operation considerably increases.

The result of total number of LTC operations under different cloud velocity scenarios are detailed in Table 3.4, where it can be seen that with the increase of cloud velocity, the LTC tends to operate more frequently.

3.5.2 Different Cloud Cover

The setup of the simulation is listed in Table 3.5. Nine cloud cover scenarios are studied, covering the range from 10% to 90%. Scenarios below 10% and above 90% are not studied, for there will be no severe PV generation fluctuation under a clear or overcast sky. Ten simulations are performed for each cloud cover scenario to study how the LTC operation will be affected under different cloud cover condition. One realization of the total PV generation for each

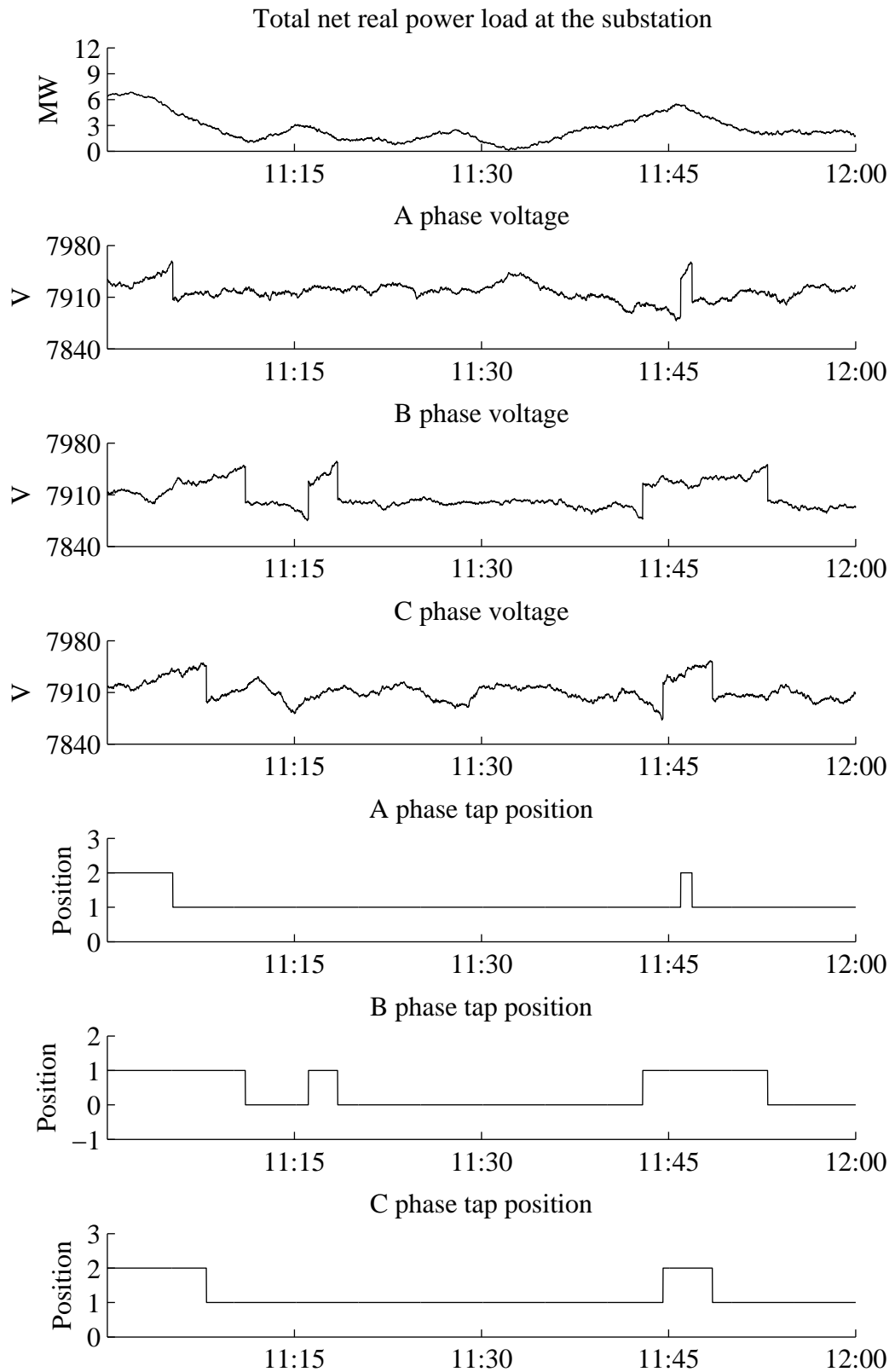


Figure 3.24: Measurements at the substation between 11 AM and 12 PM with summer load and low cloud velocity of 3 m/s.

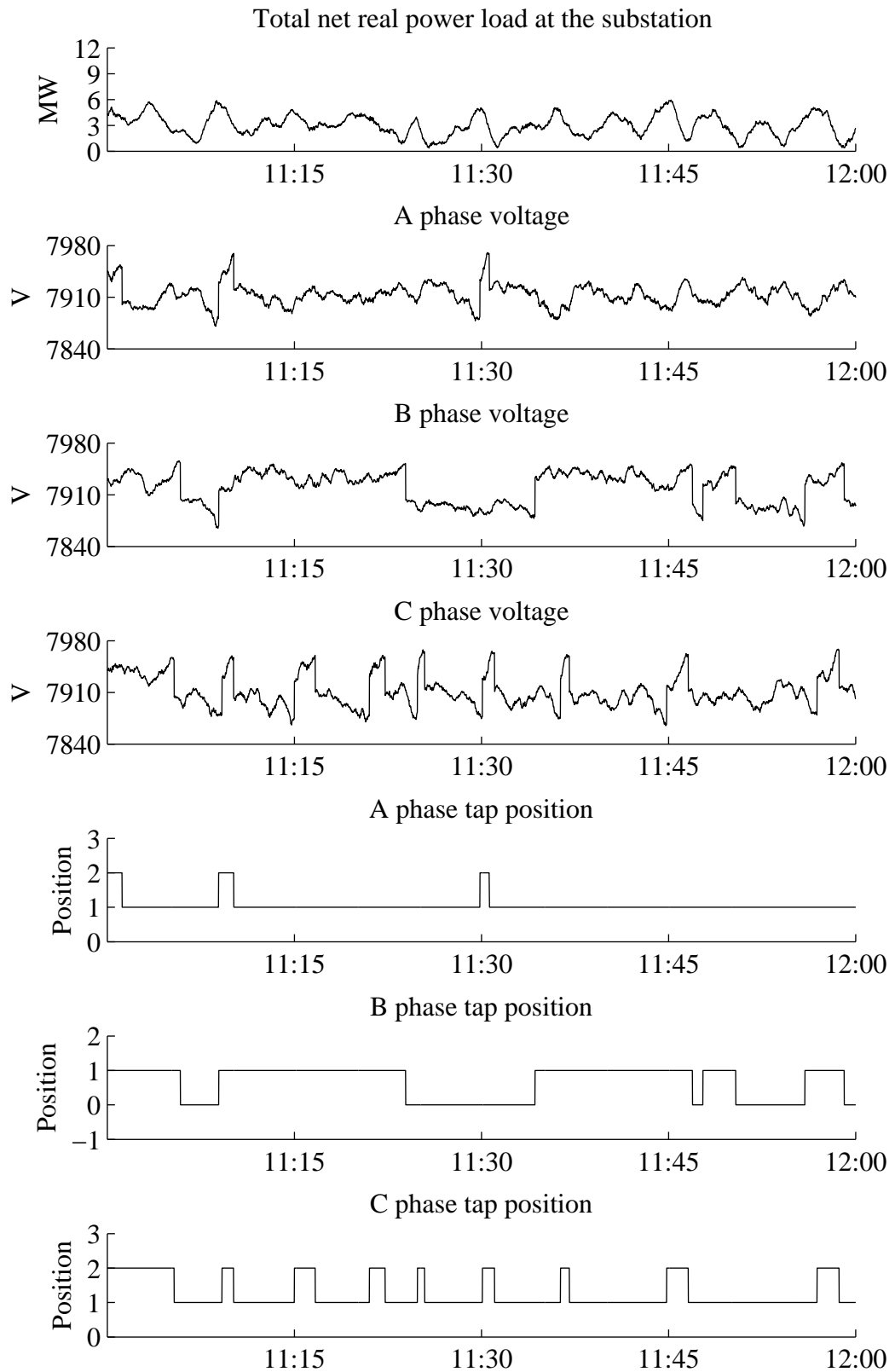


Figure 3.25: Measurements at the substation between 11 AM and 12 PM with summer load and high cloud velocity of 15 m/s.

Table 3.5: Simulation setup for studying LTC operation under different cloud cover

Simulation parameters		Scenario parameters	
T_s	11:00	cloud cover	10% to 90%
T_e	12:00	cloud velocity	6 m/s
iteration	10	cloud movement direction	0°
		PV penetration	100%

cloud cover scenario is shown in Figure 3.26, which shows that the fluctuation of total PV generation first becomes larger with the increase of cloud cover, then decreases when clouds begin to saturate the sky at high cloud cover.

Figure 3.26 shows how the LTC operates under different cloud cover condition. The total number of LTC operation moderately increases as the cloud cover grows from 10% to 30%. The LTC starts to operate much more frequently with cloud cover from 40% to 60%, largely due to the increased size of cloud shadows which are large enough to cover the most or entire part of the distribution feeder area. Beyond the cloud cover of 60%, the number of LTC operations slightly decreases for 70% and 80% cloud cover condition and further drops to a much lower level with 90% cloud cover which indicates an almost overcast sky with a few holes on the sky for the sunlight reaching to the ground. The numerical results of the simulation listed in Table 3.6, where the last line shows the average value of total number of LTC operations under different different cloud cover scenarios.

3.6 Different PV Penetration

This section studies the LTC operation under different penetration scenarios. The PV penetration is defined in Section 3.3.4 and the simulation setup is listed in Table 3.7. PV generation under different PV penetration scenarios is plotted in Figure 3.28, where it can be observed that with the increase of PV penetration, the total PV generation level also increases but at the same time experiences larger variation. The numerical results of total number of LTC operations are detailed in Table 3.8. As expected, the LTC tends to operate more

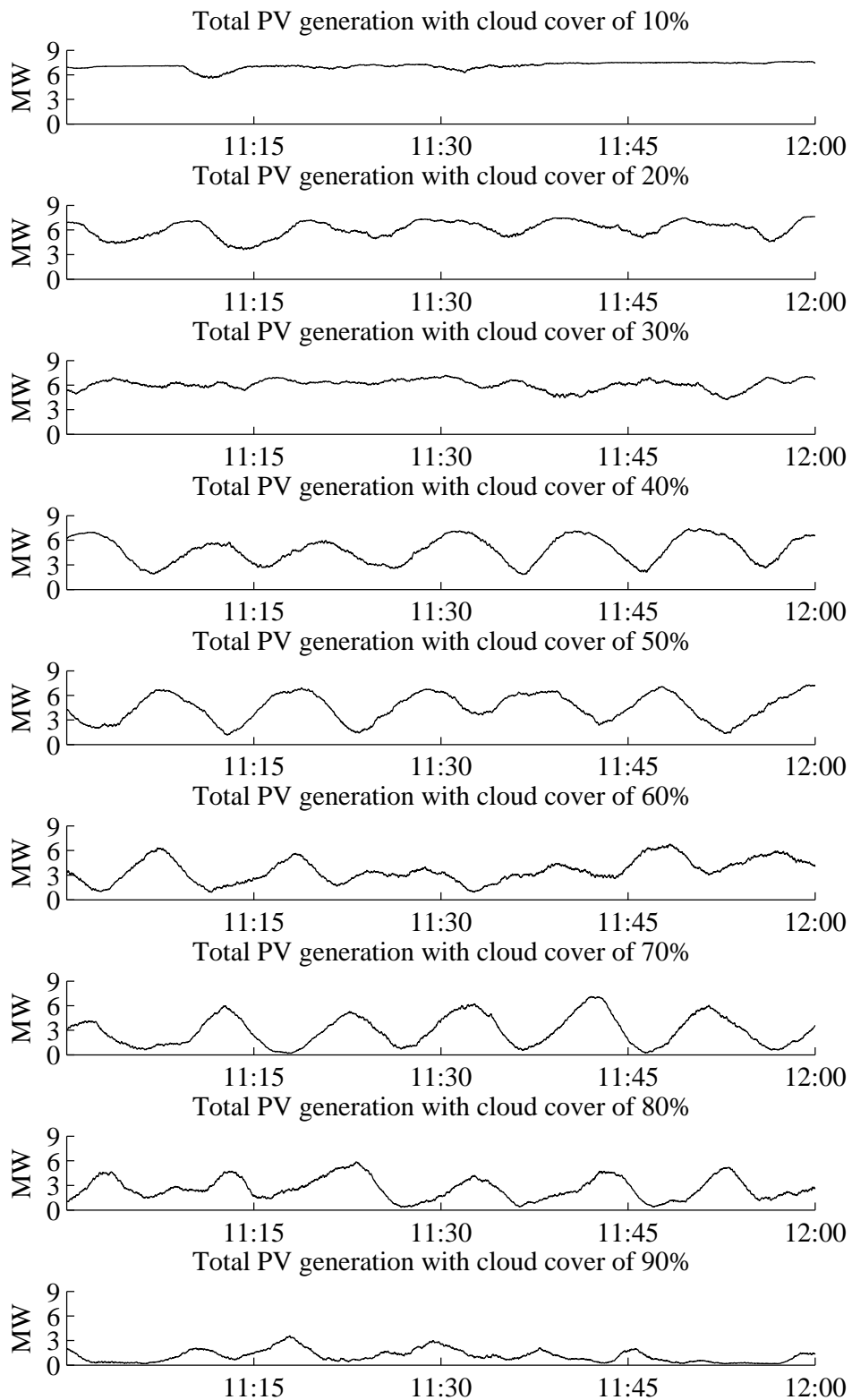


Figure 3.26: Total PV generation of one simulation case with different cloud cover.

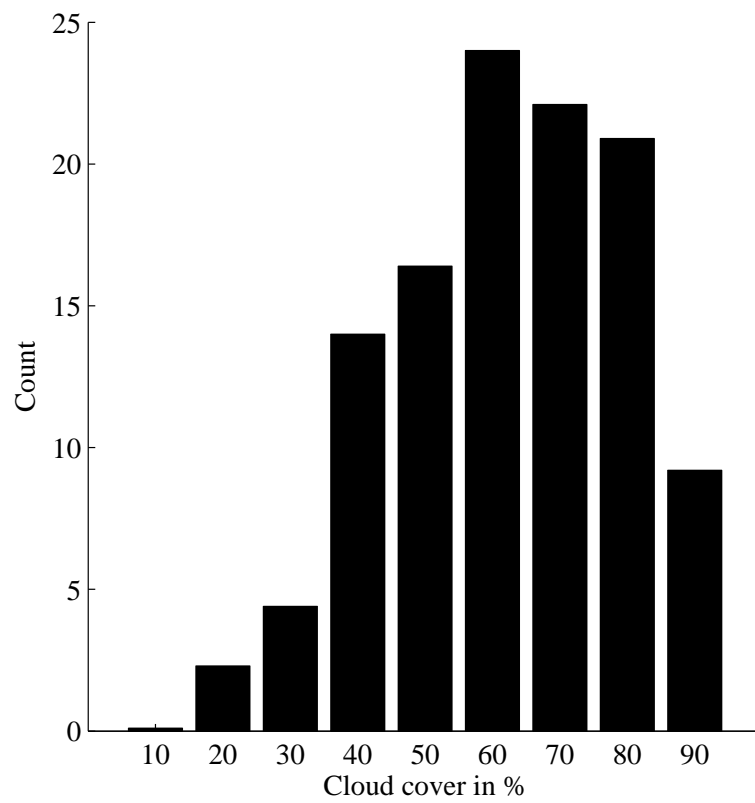


Figure 3.27: The average value of three-phase total number of LTC tap changes in the 1-hr period simulation in a summer day with different cloud cover scenarios.

Table 3.6: Simulation result of total number of LTC operations in 1-hr period of the summer day with different cloud cover scenarios

	10%	20%	30%	40%	50%	60%	70%	80%	90%
case 1	0	0	5	13	12	25	25	21	12
case 2	0	2	14	26	10	28	22	20	6
case 3	0	2	6	12	24	23	17	25	8
case 4	1	2	2	10	17	24	30	18	8
case 5	0	2	4	6	17	28	12	19	9
case 6	0	4	0	22	19	21	27	18	12
case 7	0	3	3	15	16	19	20	20	10
case 8	0	4	4	4	16	24	20	19	10
case 9	0	2	2	22	12	30	23	18	11
case 10	0	2	4	10	21	18	25	31	6
Average	0.1	2.3	4.4	14	16.4	24	22.1	20.9	9.2

frequently with increased amount PV generation.

3.7 Comparison of Different Cloud and Irradiance Models

In this section, two cloud models are compared to show what differences they could make on the LTC operation under different cloud condition.

In [14], Jewell developed the cumulative distribution function of the area of small cumulus cloud shadows, given by (3.5), based on the cloud shadow size statistics derived in [13].

Table 3.7: Simulation setup for studying LTC operation under different PV penetration

Simulation parameters		Scenario parameters	
T_s	11:00	cloud cover	50%
T_e	12:00	cloud velocity	6 m/s
iteration	10	cloud movement direction	0°
		PV penetration	25%, 50%, 75%, 100%

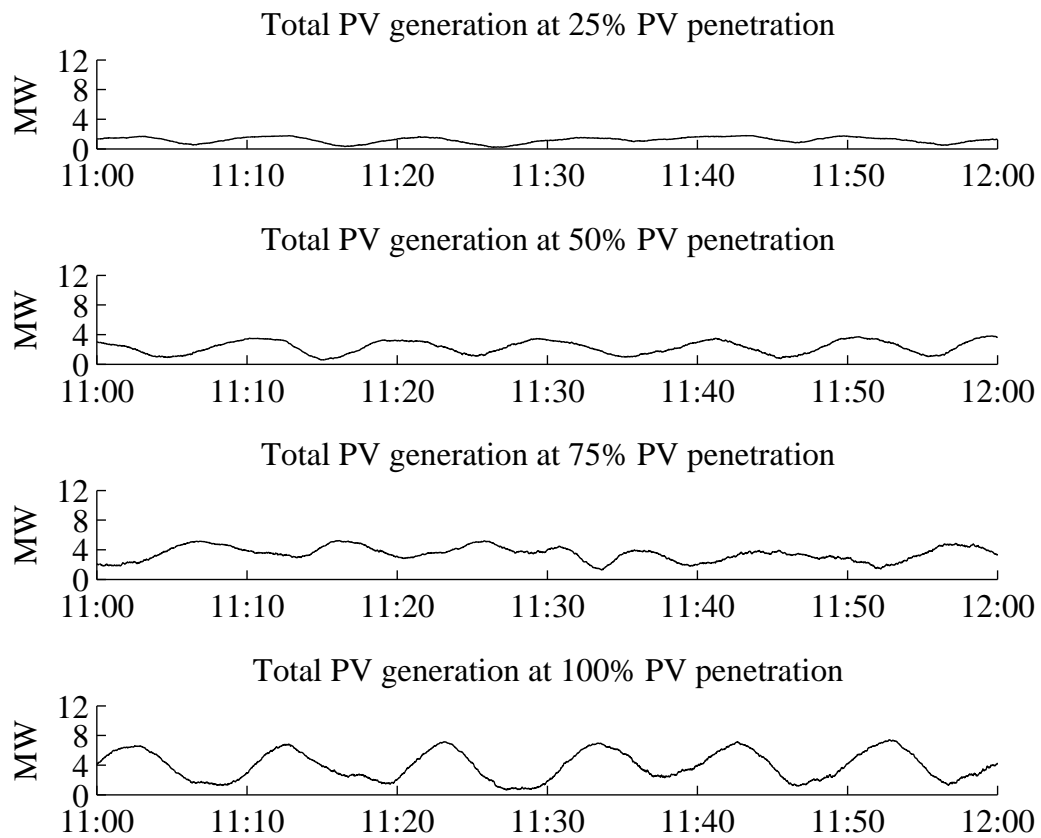


Figure 3.28: Total PV generation for 50% cloud cover and 6 m/s cloud velocity under 25%, 50%, 75% and 100% PV penetration scenarios.

Table 3.8: Simulation result for the summer day with PV penetration scenarios (cloud cover is 50% and cloud velocity is 6 m/s).

	25%	50%	75%	100%
case 1	3	7	13	17
case 2	3	13	15	16
case 3	4	7	12	21
case 4	4	7	17	17
case 5	4	13	16	26
case 6	4	14	20	16
case 7	2	15	16	14
case 8	4	18	18	24
case 9	2	9	14	21
case 10	4	10	12	19
Average	3.4	11.3	15.3	19.1

$$F(a) = a(0.88 - 0.442 \ln a) - 0.18; \quad 0.1 < a < 2.34 \quad (3.5)$$

Figure 3.29 shows the cumulative distribution function of the cloud shadow area a . The Inverse Transform Sampling technique is used to randomly generate the size of the cloud shadow. To use the Inverse Transform Sampling technique, a random number between 0 and 1 with the uniform distribution is firstly generated. Then using the value of this random number as $F(a)$, a can be reversely solved by different numerical methods. Note that there might be multiple solutions to a , and the value within the range of 0.1 and 2.34 should be used and others should be discarded.

All cloud shadows are assumed to have the rectangular shape, the length (L) and width (W) of which can be determined by (3.6)

$$W = 0.582L \quad (3.6)$$

By (3.5) and (3.6), a large number of cloud shadow objects with known shape, width and

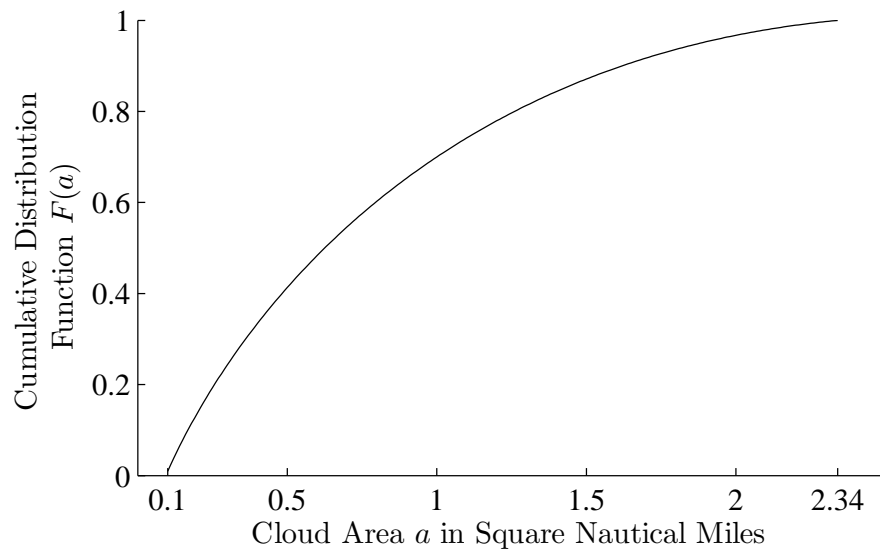


Figure 3.29: The cumulative distribution function (CDF) of the cumulus cloud with area a within range of 0.1 to 2.34 square nautical miles.

length can be generated and serve as the candidates for generating the cloud shadow pattern. In [14], no technical detail is provided about how to place the cloud shadows to form the pattern. To overcome this limitation, a procedure is developed here, as shown by the flow chart in Figure 3.30.

Figure 3.31 shows an example of generating the cloud shadow pattern using Jewell's method explained in Figure 3.30. For each iteration, a randomly selected cloud shadow is randomly placed in the cloud pattern band. The iteration process stops when the specified cloud cover is reached.

Figure 3.32 compares the generated cloud shadow pattern under different cloud cover using two different models. As can be observed, at low cloud cover, the fractal model mostly generates small cloud shadows, which is realistic, however the Jewell model tends to generate much larger bulk of cloud shadows. At 50% cloud cover, the fractal model starts to generate some large cloud shadows with similar sizes to the shadows generated by Jewell's model.

Figure 3.33 compares the total PV generation for the one hour period by using different models. From Figure 3.33-(a) and Figure 3.33-(b), it can be seen that with low cloud cover of 25%, the simulated PV generation by Jewell's model experiences severe fluctuations due to

Table 3.9: Simulation result of total number of LTC operations in the study of comparing two different cloud shadow models

cloud cover	Fractal Model		Jewell Model	
	25%	50%	25%	50%
case 1	0	23	9	21
case 2	3	16	6	18
case 3	4	26	6	19
case 4	0	14	15	14
case 5	2	16	10	14
case 6	6	11	8	21
case 7	10	28	5	23
case 8	8	21	16	23
case 9	6	10	12	20
case 10	4	18	10	15
Average	4.3	18.3	9.7	18.8

those large bulky cloud shadows it generates. In contrast, the fractal model synthesizes the PV generation with much less variation, as what will be expected from a mostly clear sky condition. With the cloud cover increasing to 50%, PV generation profiles simulated by both models have severe variations. This is because with increase of the cloud cover, both models will generate cloud shadows that are large enough to cover the most or the whole part of the distribution feeder.

Figure 3.34 compares the voltage profile on each phase for 25% cloud cover. The difference is phenomenal that the LTC operates more often with the cloud shadow pattern generated by the Jewell's model. Figure 3.35 compares the voltage profile on each phase for 50% cloud cover. Different from the case of 25% cloud cover, LTC operates frequently in both models, and this is mainly due to the fact that when the sky is more and more occupied by clouds, there will be less difference made by using different models. Table 3.9 lists the numerical results where the above analysis can be seen clearly.

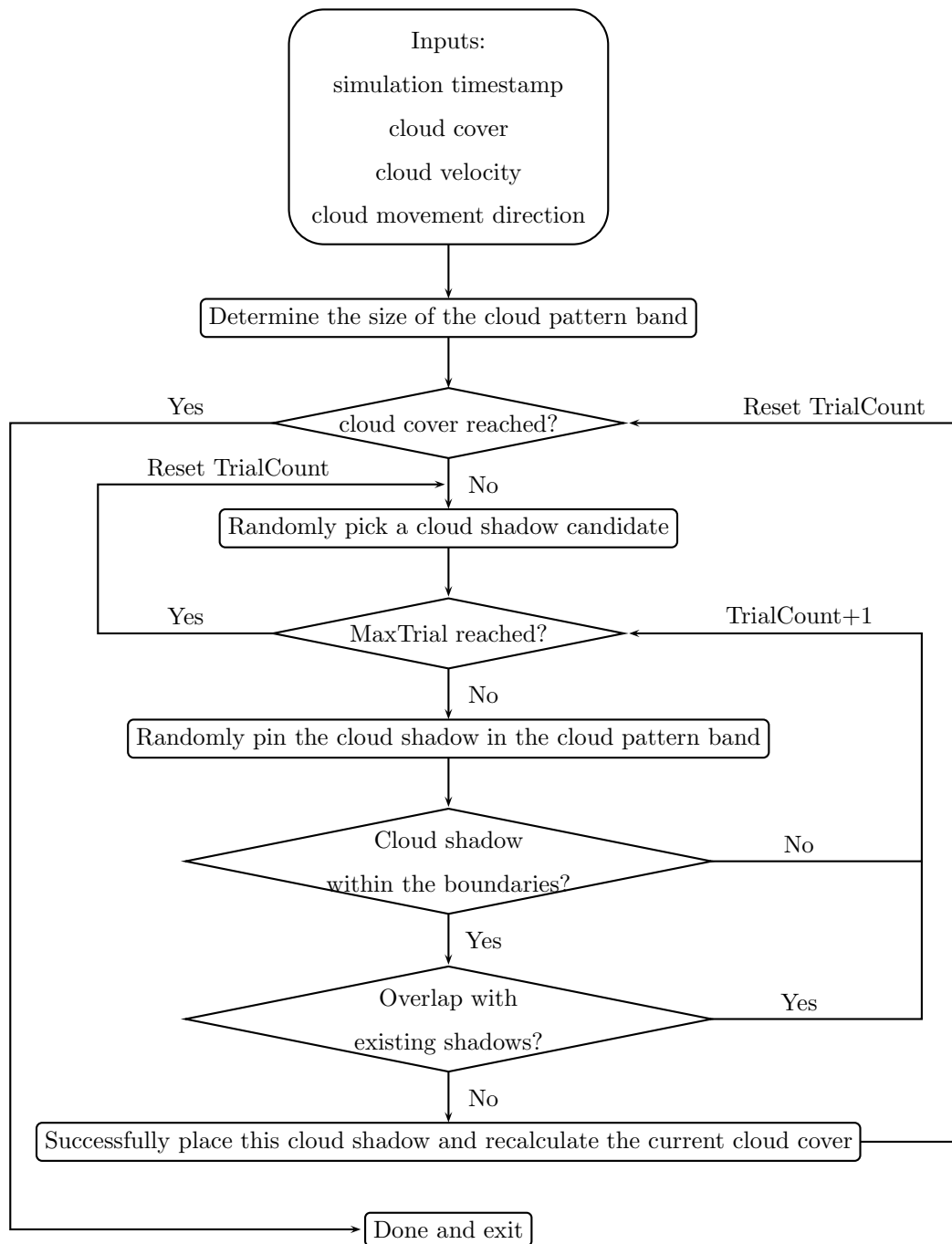
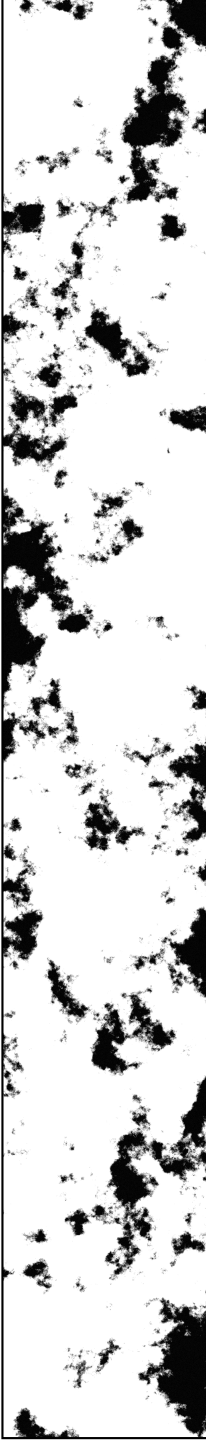


Figure 3.30: Procedure to place cloud shadow objects in generating the shadow pattern.

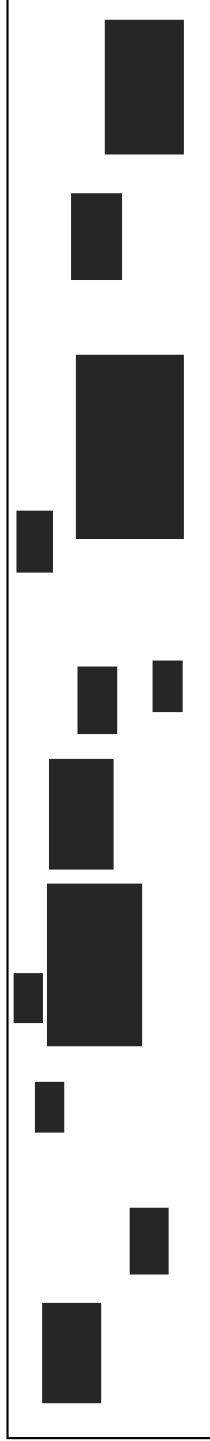


Figure 3.31: The procedure of generating the cloud pattern band using Jewell's method. Black parts are cloud shadows. In this example, the cloud cover is set to be 30% and the cloud velocity is 10 m/s. The simulation time is 2 hours.

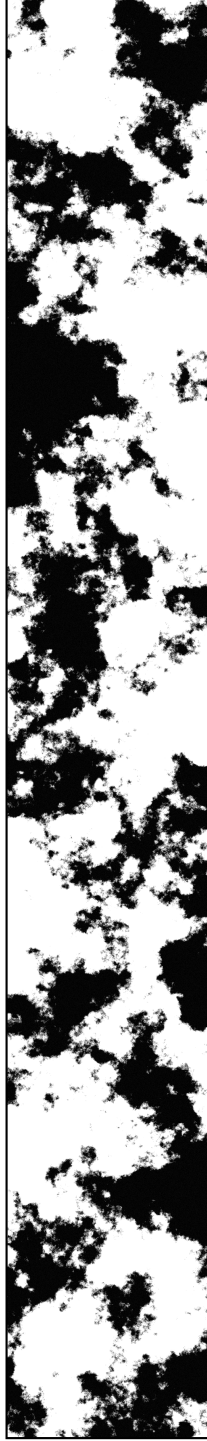
(a) 25% cloud cover using fractal based model



(b) 25% cloud cover using Jewell's model



(c) 50% cloud cover using fractal based model



(d) 50% cloud cover using Jewell's model



Figure 3.32: Generated cloud shadow pattern using the fractal and Jewell's model for different cloud cover. Cloud velocity is 6 m/s and the simulation duration is 1 hour. The length of the cloud pattern is 25 km and the width is 3.6 km.

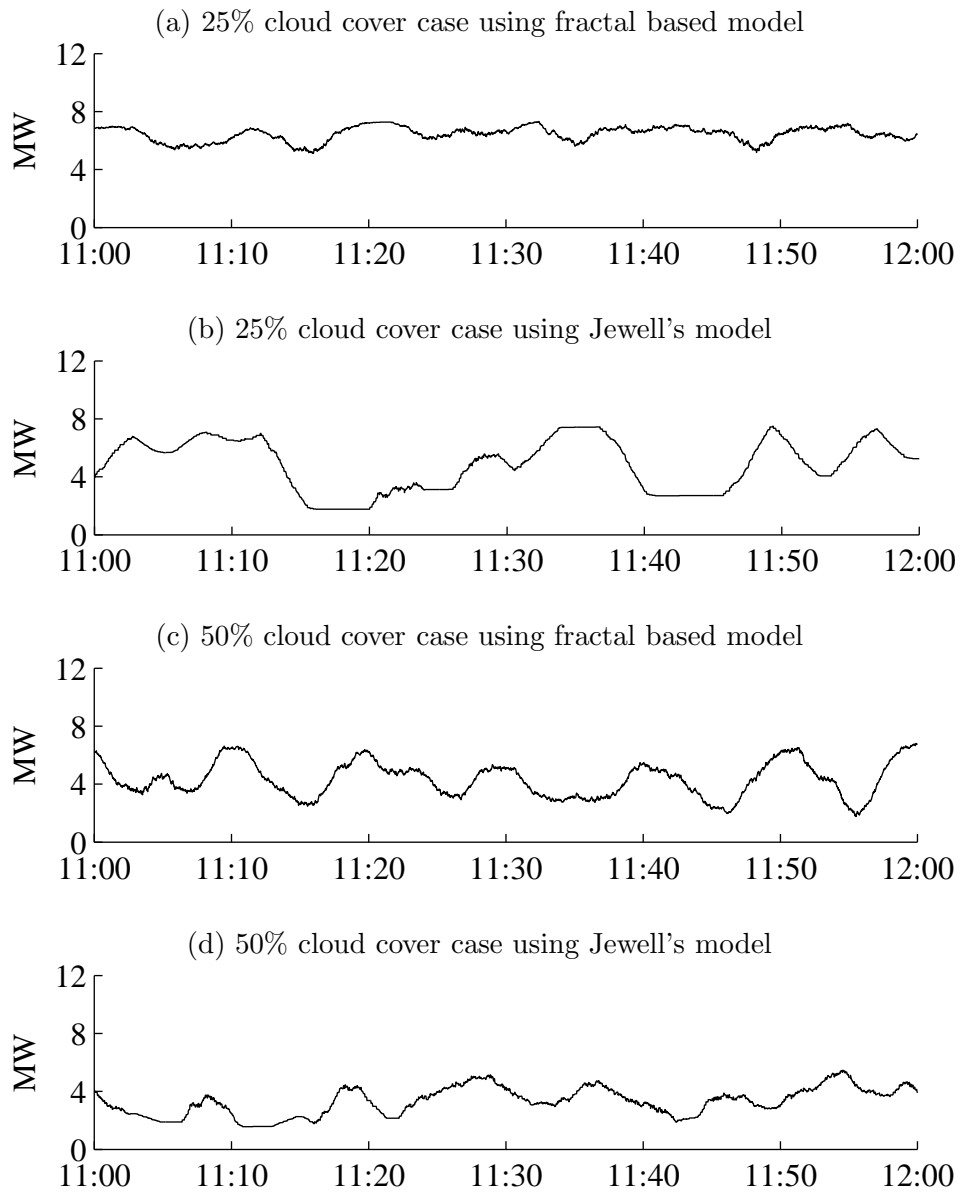


Figure 3.33: PV generation for the study area under different cloud pattern synthesized by different model.

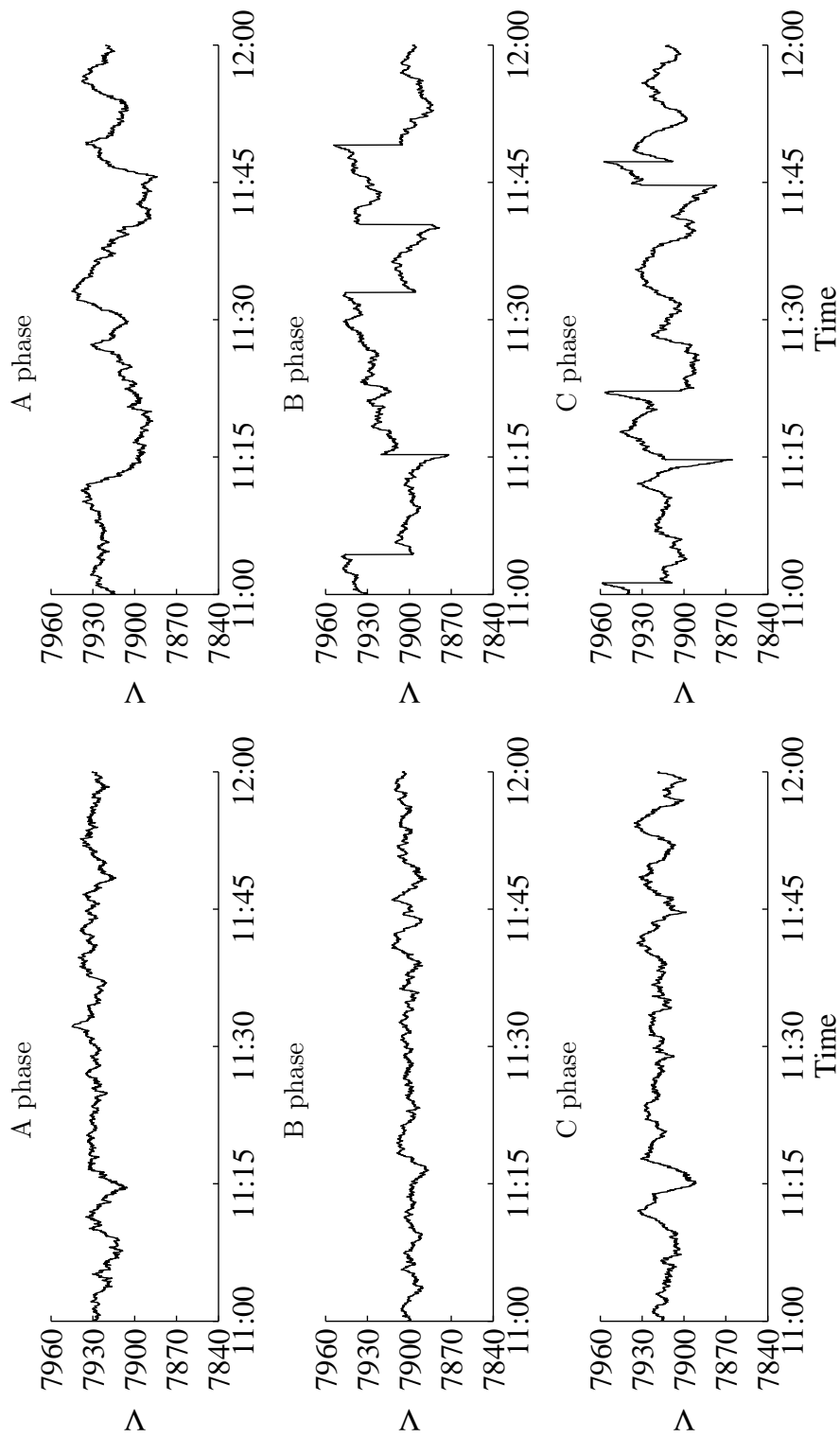


Figure 3.34: Compare the voltage profile of each phase under 25% cloud cover scenario using fractal based model (left) and Jewell's model (right).

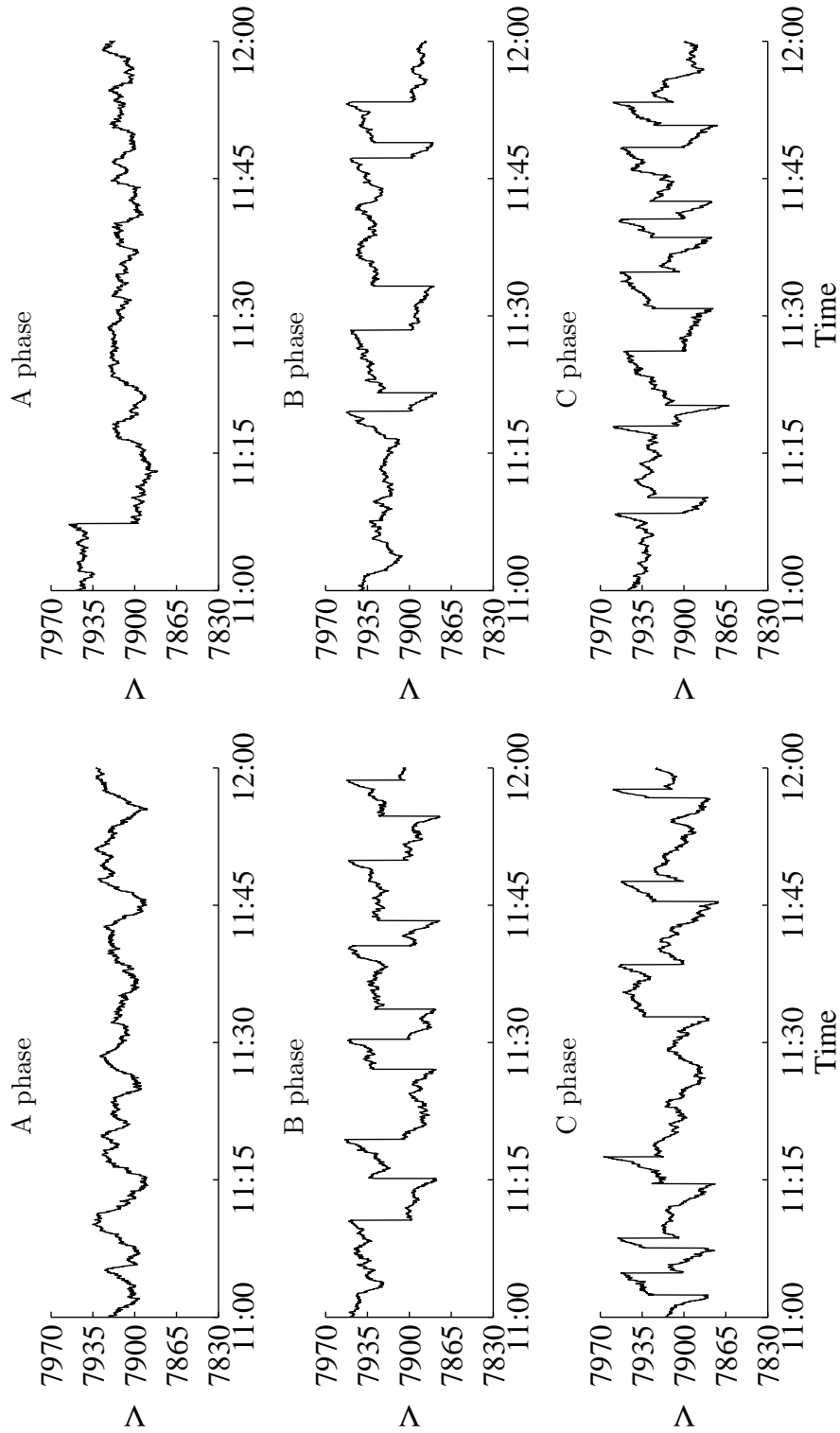


Figure 3.35: Compare the voltage profile of each phase under 50% cloud cover scenario using fractal based model (left) and Jewell's model (right).

CHAPTER 4 CONCLUSION AND FUTURE WORK

4.1 Conclusions

This dissertation proposed and developed a cloud shadow and irradiance model, which can be used to generate time series of solar irradiance for each PV system embedded within an area of interest during time periods with low-altitude cumulus clouds, which is considered to cause most of the fluctuation on PV power output. The time series of solar irradiance can be further converted to model the power output of individual PV system, which is commonly required in all kinds of PV integration studies.

The idea is to generate realistic cloud shadow patterns by modeling the cloud shadows as fractals, which are moved over an area of interest with embedded PV generation. Additional enhancements to the model include representing the thickness of clouds, yielding smooth and realistic irradiance transitions, and the ability to conduct long-term (hour-long or more) studies under varying cloud cover and cloud velocity.

The algorithm behind the model to generate the cloud shadows is computationally inexpensive and thus it is suitable and efficient for performing Monte-Carlo simulations by creating a large number of PV generation scenarios.

Compared to the complex physics-based cloud and irradiance models in the meteorology field, the model in this dissertation is purposely designed to be simple for power engineers to use, without requiring an expertise in meteorology. It only needs three meteorological inputs, i.e., cloud cover, cloud velocity and cloud movement direction. The data for all three inputs are widely available and can be readily acquired from different resources, e.g., the well known Automated Surface Observing Systems (ASOS) of National Weather Service (NWS).

A possible way to fine tune the model parameters was also presented, and the output of

the model was validated against the recorded measurement in the real world, which showed a reasonably good match.

The main contribution of the model is its capability to realistically reproduce the irradiance waveforms for a large number of locations in an area under changing weather condition while accounting for the spatial diversity and temporal variability at high resolution, which has been overlooked by previous models and studies. This is key to assessing the impact of high penetration of PV on the system operation and evaluating the corresponding mitigation measures, e.g., new voltage control devices and control methods. Thus, the accuracy of modeling the distributed PV generation is improved and studies based on PV modeling are more realistic. Another feature of the model is that the output of the model can be easily integrated with distribution feeder simulation software such as GridLAB-D [4] or OpenDSS [5].

To demonstrate the potential application of the model and how the model could be used in together with other distribution system simulation software (GridLAB-D in this dissertation), a case study focusing on the impact of the high penetration of PV to the switching actions of Load Tap Changer was carried out. The case study also provided a detailed procedure of modeling the PV systems, which interact with the cloud shadow and irradiance model to produce the PV power output injected into the distribution feeder at the location of each house.

In the case study, the switching behavior of LTC was precisely simulated at 1-sec time step and closely examined in the summer and winter season. A major implication of the simulation results is that, at high penetration level, the large power output fluctuation of PV systems caused by cloud shadows considerably increases the number of switching actions of LTC, especially in the winter scenario.

LTC operation under different cloud condition and PV penetration level were also investigated. It is found that with the increase of cloud movement speed, LTC switches more frequently. Besides, it is revealed that the cloud cover also affects the LTC actions. At 60% cloud cover, the increase on the number of LTC switching is most phenomenal, and the impact alleviates with less or more cloud cover.

4.2 Future Research Directions

This dissertation is not without limitations. The developed cloud shadow and irradiance model could be improved and better utilized by following aspects.

- Study the fractal dimension parameters, i.e., D_1 and D_2 .

As discussed in the dissertation, these two parameters are the key property in generating the fractal surface and the cloud shadow pattern. Although some universal values were given by previous studies, they might be dependent on the location and time of the year. When using the developed model to conduct simulation studies, as the one shown in the case study on LTC operation, it could be more precise if D_1 and D_2 value can be calculated from local cloud images. The cloud images can be captured by using the sky imager [68] and the D_1 and D_2 value can be calculated by following the method in [30].

- Modeling PV systems with field measurements on building parameters.

As described in the case study on LTC, the detailed modeling of each rooftop PV system depends on the building parameters, i.e., roof pitch, roof facing direction and available roof area for PV. Here some assumptions were made to randomly generate some parameters and the available roof area was approximatively estimated from satellite images. The simulation could be even more accurate and realistic if field measurement can be carried out to build statistic models for these parameters.

- Considering the limitation of power electronics.

In this dissertation, the ideal PV inverter was used and the maximum power point tracking (MPPT) was assumed to be instantaneously achieved. It might affect the simulation result if the limitation of these power electronics are modeled. It is also interesting to evaluate and test the MPPT capability using the developed cloud shadow and irradiance model.

The developed cloud shadow and irradiance model serves as a useful tool to facilitate all kinds of PV integration studies. Future research directions are proposed as follows.

- Calculating the hosting capacity of PV in distribution feeders with consideration of voltage control devices.

The hosting capacity is a useful and popular index to quantify the potential of installing distributed photovoltaics in a distribution system. Most of calculations of the hosting capacity only consider static metrics, e.g., maximum loading of power transformers, system energy loss, voltage drop along the feeder, etc. With the proposed cloud shadow and irradiance model, the behavior of various voltage control devices can be precisely simulated with high penetration of PV, as shown by the case study on LTC. These voltage control devices largely affect the distribution system performance and the power quality. Thus, it will be important and necessary to estimate the hosting capacity while considering the constraints posed by these devices, e.g., number of switching actions per period of time.

- Evaluating the Volt/VAR control with high penetration of PV.

The Volt/VAR control is quickly becoming an effective way to mitigate the voltage fluctuation and voltage rise caused by high penetration of PV. The Volt/VAR control will need the coordination between devices, e.g., PV inverters. Otherwise, the control devices might fight between each other, causing technical problems to the distribution system. It is common for these control devices to take the local measurement as the control signal, which means the accurate modeling of PV generation for each PV system is vital to evaluating the Volt/VAR control method.

- Impact of utility-scale PV farms to the voltage stability of the transmission grid.

Unlike distributed PV systems embedded in a distribution feeder, the utility-scale PV farm usually deploys a high capacity PV system in a relatively small area. Under certain circumstances, the cloud shadow is large enough to cover the entire PV system in a short period of time, which yields a severe power fluctuation that disturbs the transmission system. Thus it is of great interest to system operators to investigate the voltage stability issue when this type of event takes place. The developed cloud shadow model could be used to simulate the power output of the utility-scale PV farms at high temporal resolution during cloudy days and recreate this scenario for voltage stability analysis and

testing of voltage control methods.

- Generate scenarios for stochastic unit commitment with high penetration of PV.

With integrating of an increasing amount of PV, the traditional unit dispatch model is being challenged by the large variability and uncertainty of PV generation. To address this, a stochastic unit commitment model has been proposed and studied, which requires scenarios of PV generation on each bus. By using the correlated weather information on each bus as the meteorological inputs, the cloud shadow model could be used to create a large number of scenarios of correlated PV generation on each bus. The generated PV power scenario can have high temporal resolution, e.g., 1-min, which enables the modeling of unit commitment in greater details.

APPENDIX A Technical Data for 65 PV Modules

This appendix contains the full list of 65 PV modules used in the PV modeling. Below are some notes about the data.

- In the “Type” column, “P” represents the Polycrystalline solar cell and “M” represents the Monocrystalline solar cells.
- “STC” stands for standard test condition, i.e., irradiance of 1000 W/m² and ambient temperature of 25°.
- The efficiency is calculated as

$$\text{Efficiency} = \text{STC Capacity}/(\text{Size}*1000)$$

Table A.1: Module data part 1

Name	Type	STC Capacity (W)	Width (in)	Length (in)	Size (m ²)	Efficiency (%)
Astronergy CHSM 6612P 305	P	305	39.13	77.01	1.94	15.69
Astronergy CHSM 6610P 255	P	255	39.13	65.04	1.64	15.53
Astronergy CHSM 6610P 250	P	250	39.13	64.04	1.62	15.46
SolarWorld SW 260	M	260	39.41	65.94	1.68	15.51
SolarWorld SW R6A 130	P	130	26.77	59.37	1.03	12.68
SolarWorld SW 265	M	265	39.41	65.94	1.68	15.81
SolarWorld SW 255	M	255	39.41	65.94	1.68	15.21
ET Solar ET-P660250WB	P	250	39.06	64.57	1.63	15.36
ET Solar P672300WB	P	300	39.06	77.01	1.94	15.46
Eoply EP125M/72	M	190	31.81	62.2	1.28	14.88
Kyocera KD140GX-LFBS	P	140	26.3	59.06	1	13.97
Kyocera KD140SX-UFBS	P	140	26.3	59.06	1	13.97
Kyocera KD245GX-LFB2	P	245	38.98	65.43	1.65	14.89
LG NeoN LG300NIC	M	300	39.37	64.57	1.64	18.29
LG Mono LG250S1C-G2	M	250	38.82	64.25	1.61	15.54
LG NeoN LG290NIC	M	290	39.37	64.56	1.64	17.68
Sharp NE-170UC1	P	170	32.5	62	1.3	13.08
Sharp ND-224UC1	P	224	39.1	64.6	1.63	13.75
Sharp ND-240QCS	P	250	39.1	64.6	1.63	15.34
Suniva MVX 250	P	250	39.05	64.54	1.63	15.38
Suniva OPT 270	M	270	38.66	65.04	1.62	16.64
SW130	P	130	26.06	58.15	0.98	13.3
SW175	M	175	31.81	62.2	1.28	13.71
AUO EcoDuo PM220P01.0-240	P	240	39.17	64.25	1.62	14.78

Table A.2: Module data part 2

Name	Type	STC Capacity (W)	Width (in)	Length (in)	Size (m ²)	Efficiency (%)
Canadian Solar CSI CS6P-190	P	190	38.3	63.8	1.58	12.05
Canadian Solar CSI CS6P-220	P	220	38.7	64.5	1.61	13.66
Canadian Solar CSI CS6P-235	P	235	38.7	64.5	1.61	14.59
Conergy S 175MU	M	175	31.8	62.2	1.28	13.71
EcoSology TWES-(225)60P	P	225	39.2	65.1	1.65	13.67
Evergreen ES-A 200-FA3	P	200	35.9	61.8	1.43	13.97
GEPV-085	M	85	20.8	47.3	0.63	13.39
Hyundai HiS-S227SG	P	230	38.7	64.76	1.62	14.22
Mitsubishi Electric MF125UE5N	P	125	26.5	58.9	1.01	12.41
Mitsubishi Electric MF185UD5	P	185	32.6	65.3	1.37	13.47
NB Solar TDB125X125-72-P	M	180	31.81	62.2	1.28	14.1
Schott Solar Perform Mono 255	M	255	39.09	66.34	1.67	15.24
Schott Solar Perform Poly 235	P	235	39.09	66.34	1.67	14.05
REC Solar REC210AE-US	P	210	39.02	66.55	1.68	12.53
REC Solar REC230PE	P	230	39.02	66.55	1.68	13.73
Ritek Solar PM230	P	230	39.37	65.32	1.66	13.86
Samsung LPC241SM	M	241	36.66	64.17	1.52	15.88
SunTech 85	M	85	21.3	47.05	0.65	13.15
SunTech 175	M	175	31.8	62.2	1.28	13.71
SunTech STP250S	M	250	39.1	64.6	1.63	15.34
REC Solar REC210AE-US	P	210	39.02	66.55	1.68	12.53
REC Solar REC230PE	P	230	39.02	66.55	1.68	13.73
Ritek Solar PM230	P	230	39.37	65.32	1.66	13.86
Samsung LPC241SM	M	241	36.66	64.17	1.52	15.88

Table A.3: Module data part 3

Name	Type	STC Capacity (W)	Width (in)	Length (in)	Size (m ²)	Efficiency (%)
SunTech 85	M	85	21.3	47.05	0.65	13.15
SunTech 175	M	175	31.8	62.2	1.28	13.71
SunTech STP250S	M	250	39.1	64.6	1.63	15.34
SunTech STP295	P	295	39.1	77	1.94	15.19
SunTech STP240	P	240	39.1	64.6	1.63	14.73
Trina solar TSM-240PA05	P	240	39.05	64.95	1.64	14.67
Trina solar TSM-220PA05	P	220	39.05	64.95	1.64	13.44
Trina solar TSM-DA01-175	M	175	31.85	62.24	1.28	13.68
Yingli Solar YL270C-30b	M	270	38.98	64.96	1.63	16.53
Yingli Solar YL245P-29b	P	245	38.98	64.96	1.63	15
Yingli Solar YL305P-35b	P	305	38.98	77.56	1.95	15.64
Jinko Solar JKM315M-72	M	315	39.05	77.01	1.94	16.24
Jinko Solar JKM275M-96	M	275	42.63	61.85	1.7	16.17
Jinko Solar JKM270M-60	M	270	39.05	65	1.64	16.49
Jinko Solar JKM210M-72	M	210	31.81	62.2	1.28	16.45
Jinko Solar JKM265P-60	P	265	39.05	65	1.64	16.18
Jinko Solar JKM310P-72	P	310	39.05	77.01	1.94	15.98
SunPower E20-327	M	327	41.2	61.4	1.63	20.04
SunPower X21-345	M	345	41.2	61.4	1.63	21.14
Hanwha Solar HSL72P6-PB-305W	P	305	38.9	77	1.93	15.78
Hanwha Solar HSL72P6-PA-280W	P	280	39.37	77.4	1.97	14.24
Hanwha Solar SF160-24-1M195	M	195	31.8	62.2	1.28	15.28
Hanwha Solar SF160-24-1M170L	M	170	31.8	62.2	1.28	13.32
Hanwha Solar HSL60M6-HA-1-265	M	265	39.37	65.04	1.65	16.04

APPENDIX B PV Experimental Station

This appendix documents the PV experimental station in Iowa State University. Schematics of system design and list of equipments are included. The user interface of PV data acquisition system is programmed in LabVIEW.

Table B.1: Equipment list of PV experimental station (electrical parts)

Product Name and Description	Part Number	Unit
Morningstar SunSaver-MPPT 15L amp-12/24V Charge Controller	3615155	1
Powersonic PS-1250F1 - 12 Volt/5 Amp Hour Sealed Lead Acid Battery	73C8390	2
Self-made rack for PV panels	N/A	1
SW-S130P Poly-crystalline 130-Watt Solar Module	1401303	2
MidNite MNPV-3, 3 Position Combiner Box 150V	8910239	1
other accessories:		
1) 50 ft of 10/2 Tray Cable THHN/THWN sunlight resistant	N/A	1
2) 1/2" Strain Relief for #10 or #12 wire	N/A	4
3) MNEPV-15 15 amp DC Breaker 150VDC DIN, 13mm	N/A	2

Table B.2: Equipment list of PV experimental station (data acquisition parts)

Product Name and Description	Part Number	Unit
Omega SAI-RTD surface mount RTD sensor	SAI-RTD	1
Omega TX92A-1-L RTD transmitter with linearized 4-20 mA output for -40 to 140 F	TX92A-1-L	1
LI-200SA-50-BNC	LI-200SA-50-BNC	1
Universal Trans-conductance Amplifier for Li-200 with BNC	UTA/BNC/200/5	1
GE HumiTrac ambient temperature and relative humidity sensor - wall mount	P40250125	1
Note: the configuration is "signal conditioned temp (-40 to 140 F)"		
Omron S8VM03024AD 24V output 30W SMPS	Z2477-ND	1
Hall Effect Current Sensor	H-ACDC-70	1
NI WLS 9205 (NI C9205 + NI 9163 Wireless Ethernet Carrier) spring terminal	NI WLS-9205	1

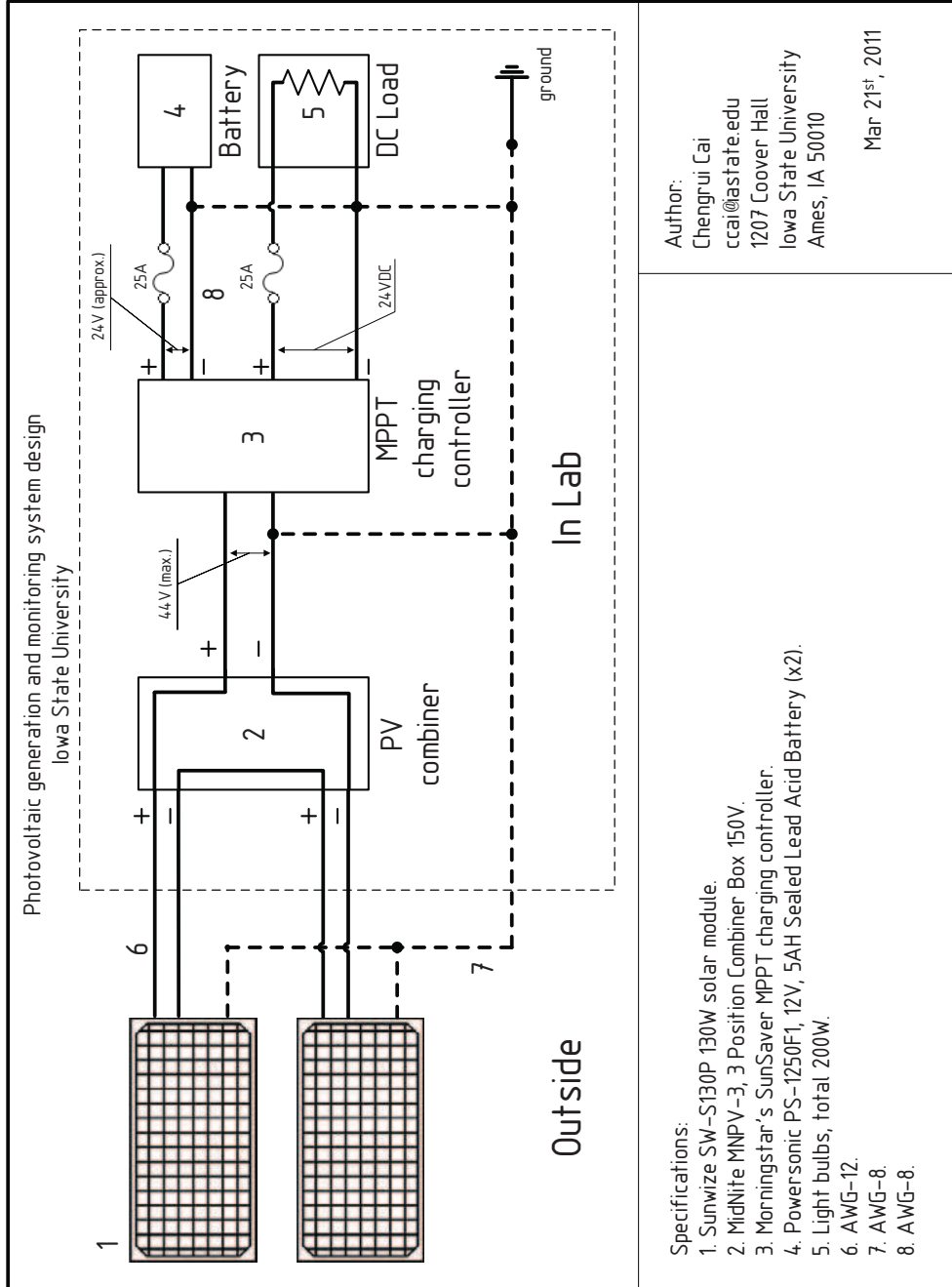


Figure B.1: Schematic of PV generation system.

Author:
Chengrui Cai
ccai@astate.edu
1207 Coover Hall
Iowa State University
Ames, IA 50010

Mar 21st, 2011

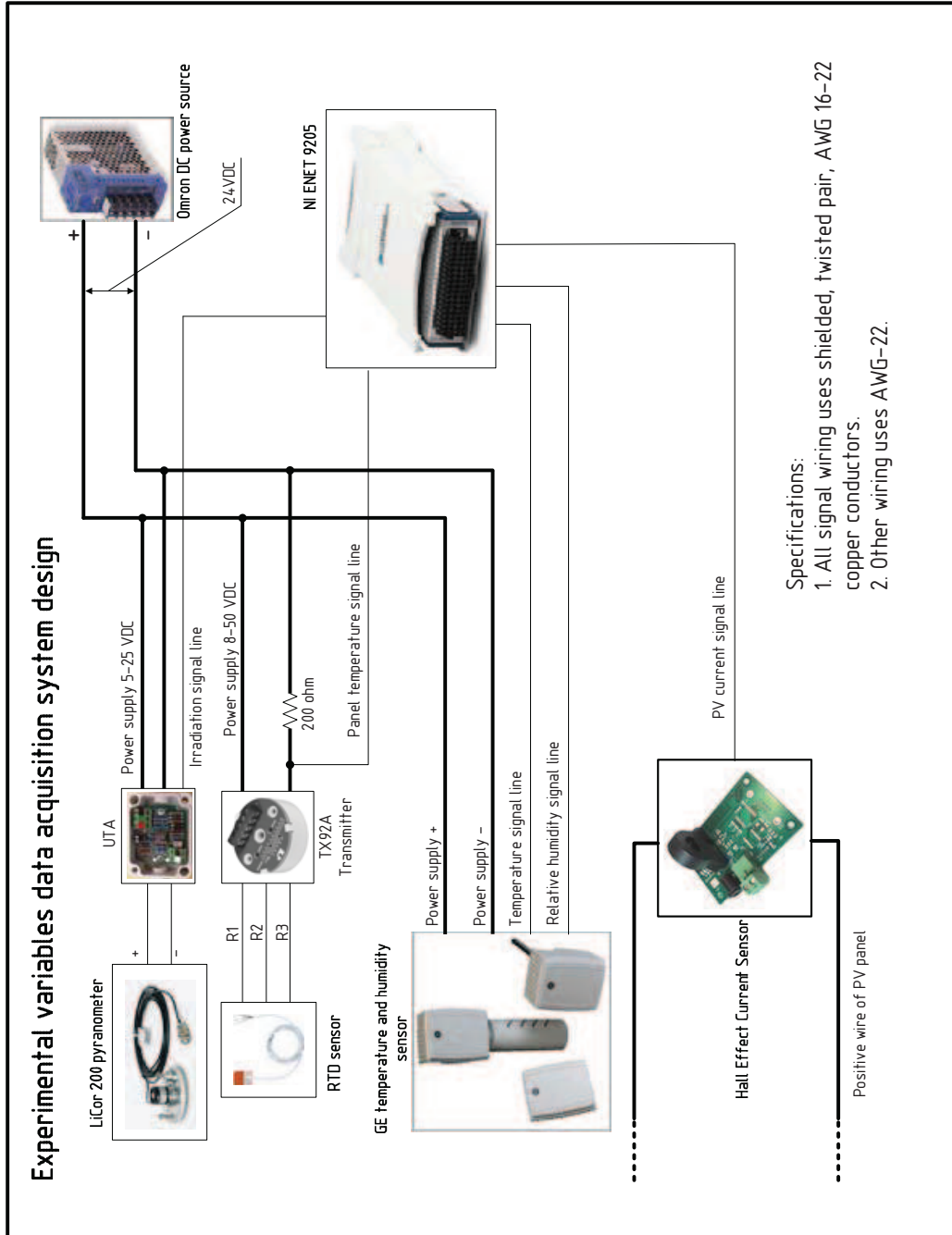


Figure B.2: Schematic of data acquisition system.

Bibliography

- [1] “EPIA market report 2013,” European Photovoltaic Industry Association (EPIA), Tech. Rep., 2013.
- [2] Cooper Power Systems. CYMDIST - Distribution System Analysis software. [Online]. Available: <http://www.cyme.com/software/cymdist/>
- [3] ETAP. Power Distribution software package. [Online]. Available: <http://etap.com/distribution-systems/distribution-systems-software.htm>
- [4] U.S. Department of Energy (DOE) at Pacific Northwest National Laboratory (PNNL). GridLAB-D simulation software. [Online]. Available: <http://www.gridlabd.org/>
- [5] Electric Power Research Institute (EPRI). Simulation Tool – OpenDSS. [Online]. Available: <http://www.smartgrid.epri.com/SimulationTool.aspx>
- [6] National Renewable Energy Laboratory. Measurement and Instrumentation Data Center (MIDC). [Online]. Available: <http://www.nrel.gov/midc/>
- [7] K. Otani, J. Minowa, and K. Kurokawa, “Study on areal solar irradiance for analyzing areally-totalized PV systems,” *Sol. Energy Mater. Sol. Cells*, vol. 47, no. 1–4, pp. 281–288, Oct. 1997.
- [8] “Utility-scale PV variability workshop report,” National Renewable Energy Laboratory (NREL), Tech. Rep., Oct. 2009.
- [9] T. E. Hoff and R. Perez, “Quantifying PV power output variability,” *Sol. Energy*, vol. 84, no. 10, pp. 1782–1793, Oct. 2010.

- [10] J. Marcos, L. Marroyo, E. Lorenzo, D. Alvira, and E. Izco, "Power output fluctuations in large scale PV plants: one year observations with one second resolution and a derived analytic model," *Prog. Photovolt: Res. Appl.*, vol. 19, no. 2, pp. 218–227, Mar. 2011.
- [11] C. W. Chow, B. Urquhart, M. Lave, A. Dominguez, J. Kleissl, J. Shields, and B. Washom, "Intra-hour forecasting with a total sky imager at the UC San Diego solar energy testbed," *Sol. Energy*, vol. 85, no. 11, Nov. 2011.
- [12] R. H. Blackmer and J. E. Alder, "Statistics of cumuliform clouds from U-2 photographs," Stanford Research Institute, Tech. Rep., May 1963.
- [13] R. T. Hall, "Cloud shadow modeling," Aerospace Corporation, Tech. Rep. (ATM76(7506-01)-1), Sep. 1975.
- [14] W. Jewell and R. Ramakumar, "The effect of moving clouds on electric utilities with dispersed photovoltaic generation," *IEEE Trans. Energy Convers.*, vol. EC-2, no. 4, pp. 570–576, Dec. 1987.
- [15] W. T. Jewell, R. Ramakumar, and S. R. Hill, "A study of dispersed photovoltaic generation on the PSO system," *IEEE Trans. Energy Convers.*, vol. 3, no. 3, pp. 473–478, Sep. 1988.
- [16] W. T. Jewell and R. Ramakumar, "The history of utility-interactive photovoltaic generation," *IEEE Trans. Energy Convers.*, vol. 3, no. 3, pp. 583–588, Sep. 1988.
- [17] W. T. Jewell and T. D. Unruh, "Limits on cloud-induced fluctuation in photovoltaic generation," *IEEE Trans. Energy Convers.*, vol. 5, no. 1, pp. 8–14, Mar. 1990.
- [18] G. A. Marotz and J. A. Henry, "Satellite-derived cumulus cloud statistics for western Kansas," *J. Appl. Meteor.*, vol. 17, no. 11, pp. 1725–1736, Nov. 1978.
- [19] D. L. Garrett and S. M. Jeter, "A photovoltaic voltage regulation impact investigation technique. I. Model development," *IEEE Trans. Energy Convers.*, vol. 4, no. 1, pp. 47–53, Mar. 1989.

- [20] H. Morf, “The stochastic two-state solar irradiance model (STSIM),” *Sol. Energy*, vol. 62, no. 2, pp. 101–112, 1998.
- [21] —, “The stochastic two-state cloud cover model STSCCM,” *Sol. Energy*, vol. 85, pp. 985–999, 2011.
- [22] —, “A stochastic solar irradiance model adjusted on the Ångström-Prescott regression,” *Sol. Energy*, vol. 87, pp. 1–21, 2013.
- [23] P. Beaucage, M. C. Brower, J. D. Frank, and J. D. Freedman, “Development of a stochastic-kinematic cloud model to generate high-frequency solar irradiance and power data,” in *Proc. 41st World Renewable Energy Forum, Am. Sol. Energy Soc. (ASES)*, Denver, CO, May 2012.
- [24] S. Lovejoy, “Area-perimeter relation for rain and cloud areas,” *Science*, vol. 216, no. 4542, pp. 185–187, Apr. 1982.
- [25] B. B. Mandelbrot, *The Fractal Geometry of Nature*. New York: W. H. Freeman and Co., 1983.
- [26] R. F. Cahalan and J. H. Joseph, “Fractal statistics of cloud fields,” *Mon. Wea. Rev.*, vol. 117, pp. 261–272, Feb. 1989.
- [27] F. S. Rys and A. Waldvogel, “Fractal shape of hail clouds,” *Phys. Rev. Lett*, vol. 56, no. 7, pp. 784–787, Feb. 1986.
- [28] K. Gotoh and Y. Fujii, “A fractal dimensional analysis on the cloud shape parameters of cumulus over land,” *J. Appl. Meteor.*, vol. 37, no. 10, pp. 1283–1292, Oct. 1998.
- [29] S. G. Roux, A. Arnéodo, and N. Decoster, “A wavelet-based method for multifractal image analysis III: Applications to high-resolution satellite images of cloud structure,” *Eur. Phys. J. B*, vol. 15, no. 4, pp. 765–786, 2000.

- [30] H. G. Beyer, A. Hammer, J. Luther, J. Poplawska, K. Stolzenburg, and P. Wieting, "Analysis and synthesis of cloud pattern for radiation field studies," *Sol. Energy*, vol. 52, no. 5, pp. 379–390, May 1994.
- [31] H. O. Peitgen, D. Saupe, and M. F. Barnsley, *The Science of Fractal Images*. New York: Springer-Verlag, 1988.
- [32] A. Gross, J. Bogensperger, and D. Thyr, "Impacts of large scale photovoltaic systems on the low voltage network," *Sol. Energy*, vol. 59, no. 4, pp. 143–149, Apr. 1997.
- [33] J. V. Paatero and P. D. Lund, "Effects of large-scale photovoltaic power integration on electricity distribution networks," *Renew. Energy*, vol. 32, no. 2, pp. 216–234, Feb. 2007.
- [34] E. Liu and J. Bebic, "Distribution system voltage performance analysis for high-penetration photovoltaics," National Renewable Energy Laboratory (NREL), Tech. Rep., Feb. 2008.
- [35] J. C. Hernández, A. Medina, and F. Jurado, "Impact comparison of PV system integration into rural and urban feeders," *Energy Convers. and Manag.*, vol. 49, no. 6, pp. 1747–1765, Jun. 2008.
- [36] Cooper Power Systems. Integrated Volt/VAR Management. [Online]. Available: http://www.cooperindustries.com/content/public/en/power_systems/solutions/ivvc.html
- [37] GE Digital Energy. Integrated Volt-VAR control (IVVC). [Online]. Available: www.gedigitalenergy.com/products/brochures/uos/VVC.pdf
- [38] J. Fan, H. Fan, P. Bakscheider, and J. D. McDonald, "Coordinated optimization in distribution operation," in *Proc. IEEE Power Eng. Soc. Gen. Meet.*, San Diego, CA, Jul. 2012.
- [39] M. J. Krok and S. Gene, "A coordinated optimization approach to Volt/VAr control for large power distribution networks," in *Proc. Amer. Control Conf. (ACC)*, San Francisco, CA, 2011, pp. 1145–1150.

- [40] E. Demirok, P. C. González, K. H. B. Frederiksen, D. Sera, P. Rodriguez, and R. Teodorescu, “Local reactive power control methods for overvoltage prevention of distributed solar inverters in low-voltage grids,” *IEEE J. Photovolt.*, vol. 1, no. 2, pp. 174–182, Dec. 2011.
- [41] P. Jahangiri and D. C. Aliprantis, “Distributed Volt/VAR control by PV inverters,” *IEEE Trans. Power Syst.*, 2013, to appear.
- [42] H. G. Yeh, D. F. Gayme, and S. H. Low, “Adaptive VAR control for distribution circuits with photovoltaic generators,” *IEEE Trans. Power Syst.*, vol. 27, no. 3, pp. 1656–1663, Aug. 2012.
- [43] J. C. Hernández, A. Medina, and F. Jurado, “Optimal allocation and sizing for profitability and voltage enhancement of PV systems on feeders,” *Renew. Energy*, vol. 32, no. 10, pp. 1768–1789, Aug. 2007.
- [44] A. Hoke, R. Butler, J. Hambrick, and B. Kroposki, “Maximum photovoltaic penetration levels on typical distribution feeders,” National Renewable Energy Laboratory (NREL), Tech. Rep., 2012.
- [45] R. A. Shayani and M. A. G. de Oliveira, “Photovoltaic generation penetration limits in radial distribution systems,” *IEEE Trans. Power Syst.*, vol. 26, no. 3, pp. 1625–1631, Aug. 2011.
- [46] “Large-scale PV integration study,” Navigant Consulting, Inc., Sandia National Laboratories, and Pacific Northwest National Laboratory, Tech. Rep., 2011.
- [47] Y. T. Tan and D. S. Kirschen, “Impact on the power system of a large penetration of photovoltaic generation,” in *Proc. IEEE Power Eng. Soc. Gen. Meet.*, Jul. 2007.
- [48] S. Achilles, S. Schramm, and J. Bebic, “Transmission system performance analysis for high-penetration photovoltaics,” GE Global Research, Tech. Rep., Feb. 2008.
- [49] C. D. Ahrens, *Meteorology Today: An Introduction to Weather, Climate, and the Environment*, 9th ed. Belmont, CA: Thomson Brooks/Cole, 2009.

- [50] A. Longhetto, G. Elisei, and C. Giraud, "Effect of correlations in time and spatial extent on performance of very large solar conversion systems," *Sol. Energy*, vol. 43, no. 2, pp. 77–84, 1989.
- [51] C. W. Hansen, J. S. Stein, and A. Ellis, "Simulation of one-minute power output from utility-scale photovoltaic generation systems," Sandia National Laboratories, Tech. Rep. SAND2011-5529, 2011.
- [52] J. A. Duffie and W. A. Beckman, *Solar Engineering of Thermal Processes*, 3rd ed. Hoboken, NJ: Wiley, 2006.
- [53] Iowa State University Department of Agronomy. Iowa Environmental Mesonet Time Machine. [Online]. Available: <http://mesonet.agron.iastate.edu/timemachine/#KCCI-016.201205201800>
- [54] National Renewable Energy Laboratory. Solar Radiation Research Laboratory, Baseline Measurement System. [Online]. Available: http://www.nrel.gov/midc/srrl_bms/
- [55] S. Heier, *Grid Integration of Wind Energy Conversion Systems*, 2nd ed. Wiley, Jun. 2006.
- [56] P. Jahangiri, D. Wu, W. Li, D. C. Aliprantis, and L. Tesfatsion, "Development of an agent-based distribution test feeder with smart-grid functionality," in *Proc. IEEE Power Eng. Soc. Gen. Meet.*, Jul. 2012.
- [57] Weather station in Ames Municipal Airport. [Online]. Available: http://mesonet.agron.iastate.edu/request/download.phtml?network=IA_ASOS
- [58] U.S. Department of Energy (DOE) at National Renewable Energy Laboratory (NREL). HOMER energy modeling software. [Online]. Available: <https://analysis.nrel.gov/homer/>
- [59] D. M. Geibel, "Load tap changers - theory and application," ABB, USA, Tech. Rep., 2013.

- [60] J. L. Johnson and G. T. Klise, *PV Value User Manual V 1.1*, Sandia National Laboratories, 9 2012. [Online]. Available: http://energy.sandia.gov/wp/wp-content/gallery/uploads/PV_Value_v1.1_user_manual1.pdf
- [61] PVWatts calculator from NREL. [Online]. Available: <http://pvwatts.nrel.gov/>
- [62] “Marketbuzz,” NPD Solarbuzz, Tech. Rep., 2013. [Online]. Available: <http://www.solarbuzz.com/landing-marketbuzz>
- [63] European Distribution System Operators’ Association for Smart Grids (EDSO for Smart Grid), “The european electricity grid initiative (EEGI) roadmap 2010-18 and detailed implementation plan 2010-12,” European Network of Transmission System Operators for Electricity (ENTSOE), Tech. Rep., May 2010.
- [64] European Regulators Group for Electricity and Gas, “Position paper on smart grids,” ERGEG, Tech. Rep., June 2010.
- [65] M. Bollen and F. Hassan, *Integration of Distributed Generation in the Power System*, ser. IEEE Press Series on Power Engineering, M. E. EL-Hawary, Ed. John Wiley & Sons, Inc., 2011.
- [66] Photovoltaic Power Systems Programme, “Impacts of power penetration from photovoltaic power systems in distribution networks,” International Energy Agency (IEA), Tech. Rep., Feb. 2002.
- [67] Washington State University Cooperative Extension Energy Program and the Northwest Energy Efficiency Alliance, “Factsheet: Reducing power factor cost,” U.S. Department of Energy (DOE), Tech. Rep.
- [68] Sky Imager. [Online]. Available: <http://www.yesinc.com/products/data/tsi880>